

Pore-level Quantitative Structure-Activity Relationship (QSAR) for Water Permeation Rate in Aquaporins

Juan José Galano-Frutos^{1,a,†,*}, Luca Bergamasco^{2,a,*}, Paolo Vigo², Matteo Morciano², Matteo Fasano², Davide Pirolli¹, Eliodoro Chiavazzo² and Maria Cristina de Rosa¹

¹ Istituto di Scienze e Tecnologie Chimiche “Giulio Natta” (SCITEC) - National Research Council (CNR), Via Largo Francesco Vito 1, 00168 Rome, Italy

² Department of Energy, Politecnico di Torino, C.so Duca degli Abruzzi 24, 10129 Turin, Italy

[†] Present address: Certest Biotec S.L., 50840 San Mateo de Gallego, Zaragoza, Spain

^a These authors contributed equally to this work.

* **Correspondence:** J.J. G.-F. jjgalano@certest.es; L.B. luca.bergamasco@polito.it

ABSTRACT

Aquaporins (AQPs) and aquaglyceroporins (AQGPs) play a crucial role in regulating water transport and solute selectivity across biological membranes. Besides their biological relevance, AQPs have attracted growing interest as models for the design of next-generation biomimetic membranes for water filtration. In this work, we present a pore-level Quantitative Structure–Activity Relationship (QSAR) approach that relates structural and physicochemical pore descriptors with experimentally reported water permeation rates across a set of AQ(G)Ps with high-resolution 3D structures. This data-driven methodology, presented here as a proof of concept, introduces a multi-feature framework for determining pore descriptors associated with water transport efficiency in AQ(G)Ps. Applied to two compiled permeation rate datasets, this framework recapitulates determinants previously reported in single-feature studies, while also highlighting additional pore descriptors that emerge as relevant in a multi-variable context. The insights gained through this approach may, in perspective, contribute to advancing the rational design of AQP-based filtration devices and to deepening the molecular understanding of the function of these valuable macromolecules in health and disease.

Keywords: QSAR; Aquaporins; Pore Permeation Rate; Pore Selectivity; Pore Descriptors.

1. INTRODUCTION

The maintenance of ionic homeostasis and water levels within the cell and within different organisms' tissues and compartments is a function that has been linked to a protein family called aquaporins (AQPs), which includes aquaglyceroporins (AQGPs). Initially referred to as Channel-forming Integral Protein (CHIP) [1–3] or Major Intrinsic Proteins (MIPs), AQ(G)Ps are 28-35 kDa integral membrane protein channels, which enable the transport of water across cells with a high efficiency and a unique selectivity. Typically assembled as tetramers (Fig. 1a), each subunit forms an integral membrane pore, characterized by six transmembrane spanning domains, with cytosolic amino and carboxy termini (Fig. 1b and 1c). Only pure water and small uncharged solutes, e.g. glycerol, urea, metalloids, carbon dioxide, oxygen, nitrogen, hydrogen peroxide and ammonia, are allowed to pass through the pore [4–7]. This selectivity is due to an electrostatic barrier located at the center of the channel, which prevents the passage of protons and other charged molecules [8] (Fig. 1b). Phenomena like the survival of some plants in extreme environments, characterized by saline-alkaline soils, high or low temperatures, heavy metal toxicity and drought are owed to adaptations developed by these organisms thanks to the presence of AQ(G)Ps [9–12]. AQ(G)Ps have also been associated with cell volume regulation, transepithelial fluid transport, cell migration and proliferation, neuroexcitation, among other physiological events [13–15], and thus linked to various non-infectious and infectious diseases in humans [3,13,14,16,17], highlighting the importance of their study across a variety of research and development fields.

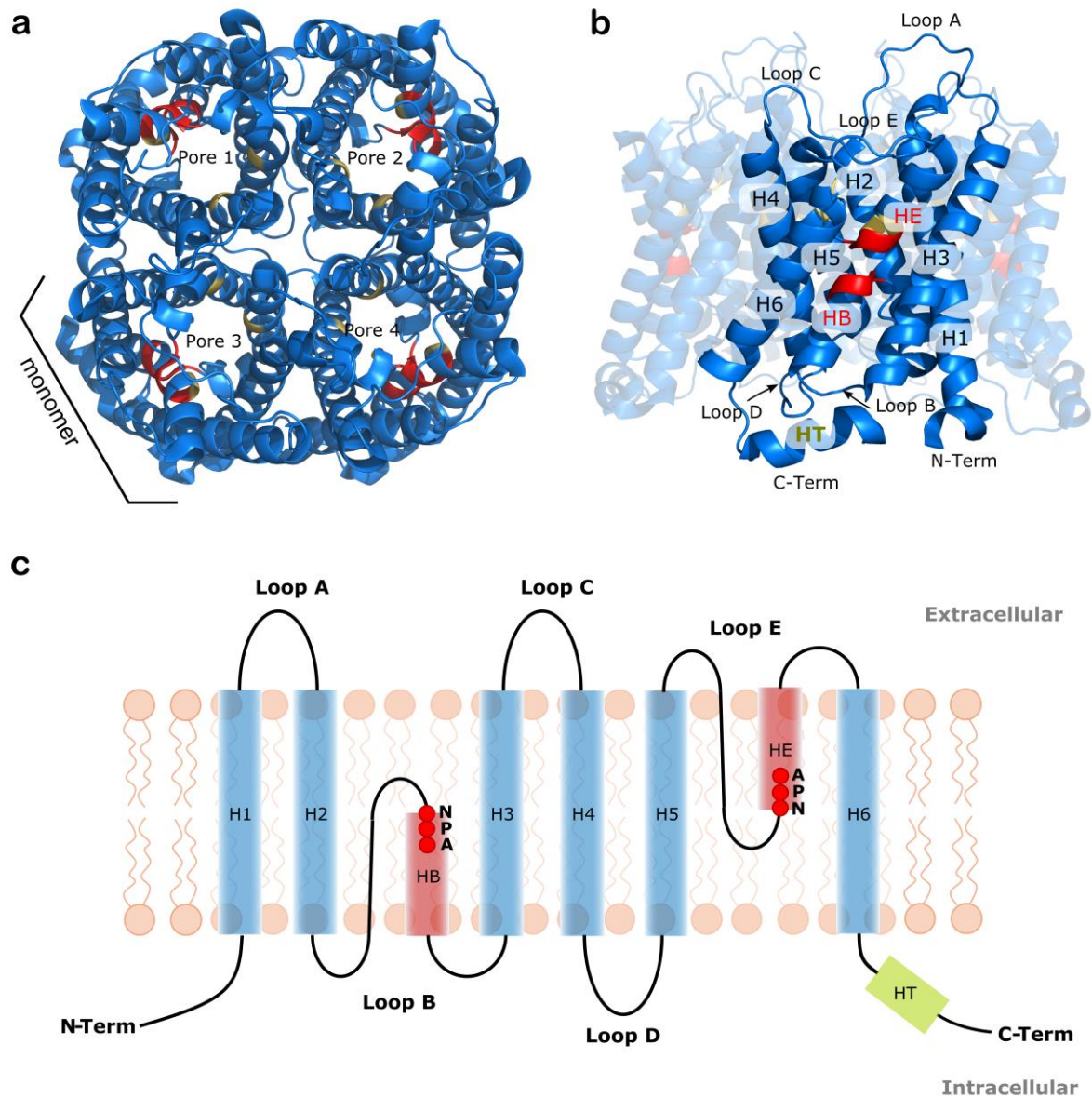


Figure 1. Structural features of mammalian AQ(G)Ps. (a) Tetrameric structure of hAQP1 (PDB ID 7UZE [18]), viewed from the extracellular side, with the pores indicated on each monomer. (b) Side view of hAQP1 highlighting the main features of the pore for one monomer. The two NPA motifs are highlighted in red, and the selectivity filter (SF) motif is highlighted in yellow. (c) Schematic representation of the mammalian AQ(G)P channel topology. Each monomer comprises six transmembrane helices (H1–H6) connected by five loops (A–E) and an additional C-terminal short amphipathic helix (HT). Loops B and E fold back into the membrane, forming two half-membrane spanning helices (HB and HE) that harbor the two asparagine–proline–alanine (NPA) motifs (red colored circles). The N- and C-termini are located in the cytoplasm, and the amphipathic helix (HT) is a common protein–protein interaction site.

There are more than 350 known aquaporins, with 13 subfamilies found in mammalian, namely AQP0-12. Mammalian AQ(G)Ps are usually divided into three sub-classes, one containing proteins that allow only water molecules flow, namely AQP0, 1, 2, 4, 5, 6 and 8, which are referred to as orthodox aquaporins, another one that allows the transport of water and other small solutes, like glycerol or urea,

that includes AQP3, 7, 9 and 10, referred to as aquaglyceroporins (AQGPs), and a more recently discovered class that has comparatively lower sequence homology (about 20%) with the orthodox aquaporins, that includes AQP11 and AQP12, referred to as unorthodox or superaquaporins [17,19,20]. A higher AQP diversity is present in plants, where there are five homologous AQP subfamilies, namely plasma membrane intrinsic proteins (PIP), tonoplast intrinsic protein (TIP), small basic intrinsic protein (SIP), nodulin-26 like intrinsic protein (NIP) and X intrinsic proteins (XIP) [10]. Amphibians [21], bacteria [22] and fungi [23] have also been reported to carry AQPs.

Thanks to their inherent functional characteristics, aquaporins are used for developing next-generation ultra-permeable membranes [24,25]. Aquaporin-based biomimetic membranes (ABMs) [26] have demonstrated remarkable promise both in water desalination [27,28] (see reviews in Ref. [29–33]) and wastewater treatment [34–36]. Their application for these and other related purposes has proven to be a valuable solution [37–39] as an alternative to conventional reverse osmosis (RO) [40,41] or thermal desalination techniques [42,43], offering potential energy and cost savings [39]. Hélix-Nielsen [31] and Beratto-Ramos et al. [36] emphasized the necessity of adopting novel optimization and design strategies to enhance ABM technology further. In close alignment with this imperative, the past 15 years have witnessed a significant surge in the development of bio-inspired artificial water channels (AWCs), which has been driven by the ambition to fabricate synthetic counterparts of AQ(G)Ps (see Ref. [44–46], and recent applications in Ref. [47,48]), marking a notable frontier in scientific exploration.

In connection with these challenges, significant efforts—spanning both experimental and computational domains—have been dedicated to unraveling the working principles governing the permeation and selective capabilities of AQ(G)Ps [19,49–60]. Most of them, however, have predominantly focused on individual features of these proteins [61], as for instance, the amino acid compositions of the NPA and SF motifs, the pore gating [59], the pore shape and size [60,61], the putative number of hydrogen bonds formed along the pore lining [57], or the number of positive charges at the pore mouth [58], to name a few. For instance, it has been shown that AQ(G)Ps' water permeability and high solute rejection occur through a narrow hydrophilic constriction, typically around ~3 Angstroms, which facilitates the formation of a water single-file wire [62]. This process is characterized by hydrogen bonding among water molecules [50,63], alongside bonding and polarizing interactions with the pore lining [57,58,62]. Also, amino acids positions determinative of AQP vs. AQGPs selectivity, and those involved in auto-

regulatory events linked to post-translational modifications have been unveiled through a variety of experimental methods, including site-directed mutagenesis, chimeric domain swaps, membrane permeability assays, electron crystallography, X-ray crystallography, and molecular dynamics simulations [19,64,65]. Despite such progress, a precise and comprehensive understanding of the permeation properties, selectivity and mechanisms exhibited by natural AQ(G)Ps remains incomplete [66].

Quantitative Structure-Activity Relationship (QSAR) (or Quantitative Structure-Property Relationship, QSPR) modeling, is one of the most extended *in silico* tools employed in medicinal chemistry [67]. In QSAR, features such as solubility, acidity, and polarity are computed as molecular descriptors and then applied to determine which of them can be used to predict measurable tasks, like toxicity, drug-likeness, or enzyme binding. The application of QSAR to model the activities or properties of peptides and proteins is an emerging field that is not yet as well established as it is for small molecules, due to the added complexity of these systems. Nevertheless, this approach has proven useful for uncovering hidden relationships that can be exploited to guide the design and optimization of the properties of systems of interest [68]. For valuable insights into the current state, development, and optimization of molecular descriptors to be used in QSAR studies on peptides and proteins, readers may refer to the following works: Ref. [69] (a review paper) and Ref. [70] (a research article).

Although well-established, QSAR methods appear to be still unexplored in the context of AQ(G)Ps. Thus, here we present—as a methodological proof of concept—a pore-level QSAR approach that combines available structural and permeability data to reveal key, and potentially novel, determinants of the filtering capabilities of these remarkable biomolecules. The proposed methodology could provide deeper insights at the molecular level, offering a better understanding of the AQ(G)Ps' functioning, and creating opportunities for the rational improvement of their properties and for targeted interventions in disease-related contexts.

2. MATERIALS AND METHODS

2.1. AQPs with available 3D structure

A search for proteins of the MIP family was performed on two different databases, namely PROSITE [71,72] and InterPro [73,74]. Proteins with experimental 3D structures available were subsequently retrieved from the RCSB PDB archive [75].

The PROSITE database [71,72], returned 285 entries (with accession code PS00221 related to MIP family). Out of the true positive sequences (264), 53 structure entries were available on the PDB archive according to this database. The InterPro database [73,74], which contained all the structure entries reported in PROSITE, returned (with accession code IPR000425 related to MIP family) 73 different PDB structures. This number of structures represented 22 individual aquaporins. In cases where multiple structures were available for a protein, the one with the highest structural resolution among those with canonical sequences (no mutations) was selected as its representative structure for the present study. An overview of these 22 AQ(G)Ps and their respective PDB IDs is reported in Table 1.

Table 1. Overview of AQPs with available 3D structure and selected PDB entries.

AQ(G)P (short name)	PDB ID	Source organism	Ref.^a
Aquaporin 0 (bAQP0)	1YMG	<i>Bos taurus</i>	[76]
Aquaporin 0 (oAQP0)	2B6O	<i>Ovis aries</i>	[77]
Aquaporin 1 (bAQP1)	1J4N	<i>Bos Taurus</i>	[78]
Aquaporin 1 (hAQP1)	7UZE	<i>Homo sapiens</i>	[18]
Aquaporin 1 (aAqp1)	7W7S	<i>Anabas testudineus</i>	[79]
Aquaporin 1 (kAqp1)	3ZOJ	<i>Komagataella pastoris</i>	[80]
Aquaporin 2 (hAQP2)	4NEF	<i>Homo sapiens</i>	[81]
Aquaporin 4 (hAQP4)	3GD8	<i>Homo sapiens</i>	[82]
Aquaporin 4 (rAQP4)	2D57	<i>Rattus norvegicus</i>	[83]
Aquaporin 5 (hAQP5)	3D9S	<i>Homo sapiens</i>	[84]
Aquaporin 7 (hAQP7)	6QZI	<i>Homo sapiens</i>	[85]
Aquaporin 10 (hAQP10)	6F7H	<i>Homo sapiens</i>	[86]
Aquaporin (SoPIP2;1)	1Z98	<i>Spinacia oleracea</i>	[87]
Aquaporin M (mAqpM)	2F2B	<i>Methanothermobacter marburgensis</i>	[88]
Probable aquaporin M (aAqpM)	3NE2	<i>Archaeoglobus fulgidus</i>	[89]
Aquaporin NIP2;1 (OsNIP2;1)	7CJS	<i>Oryza sativa japonica</i>	[90]
Aquaporin TIP2;1 (AtTIP2;1)	5I32	<i>Arabidopsis thaliana</i>	[91]
Probable aquaporin PIP2;4 (AtPIP2;4)	6QIM	<i>Arabidopsis thaliana</i>	[6]
Aquaporin Z (eAqpZ)	1RC2	<i>Escherichia coli</i>	[92]

Aquaporin Z 2 (aAqpZ2)	3LLQ	<i>Agrobacterium fabrum</i>	[93]
Aquaglyceroporin (pAqgp)	3C02	<i>Plasmodium falciparum</i>	[94]
Glycerol uptake facilitator protein (eGlpF)	1FX8	<i>Escherichia coli</i>	[62]

^a Reference articles for structures 3LLQ and 3NE2 are not yet available. In these cases the references provided are the links to the entries in the RCSB Protein Data Bank [75].

2.2. Training Set and AQ(G)Ps' Permeation Rate

We reviewed the literature for osmotic unitary (single-channel) water permeation rates (p_f)—encompassing both experimental and molecular dynamics (MD)-based approaches—reported for the 22 AQ(G)Ps with available experimental structure (see Table S1 and Fig. 2). Permeation data for other AQ(G)Ps lacking resolved 3D structures, and therefore not included in Table 1, are also provided in Tables S1 and S2 and in Fig. 2 (see details below).

Experimental data was not found for some AQ(G)Ps listed in Table 1, for which only *in silico* data is reported. For some AQ(G)Ps, we could not find any data, or the reported permeation rates were not provided as single-channel water permeabilities (i.e., p_f) but rather as global osmotic permeability coefficient (P_f) or other metrics. In cases such as hAQP7 [95–97] and hAQP10 [86], we were unable to convert P_f into p_f due to the lack of required data for such a transformation. In the case of hAQP5, the functional analysis carried out by Horsefield *et al.* [84] relied on a comparative light-scattering-based approach, for which only rate constants (k , in s^{-1}) were reported; consequently, we were not able to retrieve the p_f values.

Importantly, Wachlmayr *et al.* [56] recently revisited the stopped-flow methodology underlying many historical measurements of osmotic water permeability (P_f) and unitary water permeability (p_f). They argued that a significant subset of older reports is systematically biased because P_f was often obtained by fitting light-scattering traces to a single exponential and inserting the resulting time constant into approximate formulas that are only valid under restrictive conditions. To address this, they compare the main analysis strategies and promote an empirically corrected analytical-solution-based exponential approach (E-ASF) that retains the practical simplicity of exponential fitting while reproducing permeabilities consistent with the proper analytical solution. Crucially for legacy datasets, they provide osmolarity-based correction factors that can be applied even when the original traces are unavailable, and

show that many published p_f values should be revised downward (typically to ~ 0.25 – 0.5 of the originally reported value), in agreement with independent numerical re-fits [56]. Here, we compiled—from Ref. [56]—the corrected unitary water permeabilities (hereafter p_f^{corr}) for 8 of AQP(G)Ps listed in Table 1 (i.e., those with experimentally resolved 3D structures), as well as for 4 additional AQPs lacking 3D structures, which are used as an external validation set in the pore-level QSAR approach presented here (see Table S2 and Fig. 2).

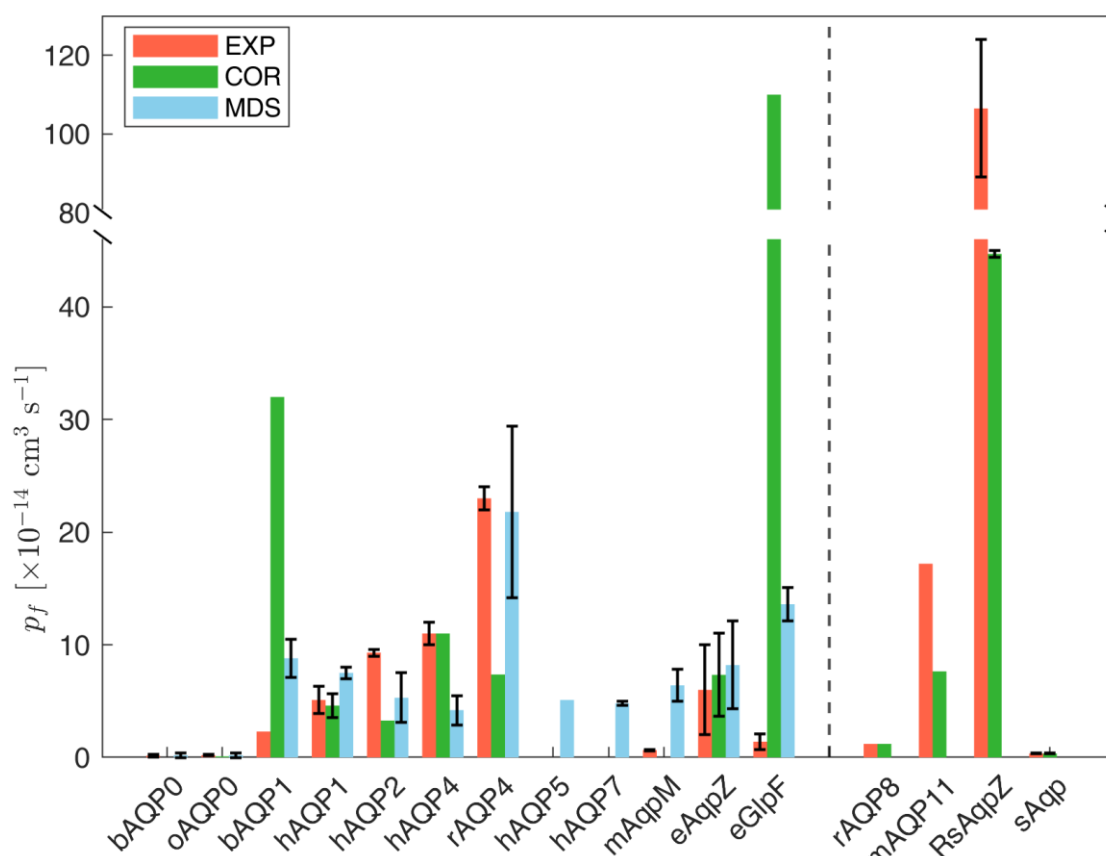


Figure 2. Osmotic unitary water permeation rates ($\times 10^{-14} \text{ cm}^3 \cdot \text{s}^{-1}$). Red bars correspond to individual p_f measurements or averages, as compiled in Table S1. Green bars correspond to corrected unitary water permeabilities (p_f^{corr} [56]), as compiled in Table S2. Cyan bars correspond to p_f values (individual or averages) obtained from molecular dynamics simulations (MDS; as compiled in Table S1). AQPs and AQP(G)Ps to the left of the vertical dashed line correspond to those with experimentally resolved 3D structures (listed in Table 1). Within this subset, experimental p_f values could not be found or derived for hAQP5 and hAQP7, and the compiled p_f^{corr} values correspond to corrections or averages derived strictly from low-temperature ($\leq 15^\circ\text{C}$) measurements (Table S2). AQPs to the right of the dashed line lack resolved 3D structures and were used as an external validation set in the pore-level QSAR approach presented here. The experimental methods employed, along with the main conditions and simulation setups used to derive the compiled values, are summarized in Table S1. When more than one value is available—regardless of the method used—the bar represents the mean value and the black vertical lines indicate the standard error of the mean. Otherwise, the black vertical line denotes the experimental or computational uncertainty—when reported—associated with the individual measurement or calculation.

Since equilibrium MDS-based approaches, mostly used in earlier modeling of AQ(G)Ps, have well-recognized limitations [98], and because MDS-derived osmotic unitary water permeabilities do not appear to align well with either non-corrected or corrected experimental estimates (see Fig. 2), we did not consider MDS-derived permeation rates for the pore-level QSAR framework presented here. We therefore carried out the proposed modelling separately for two subsets of structurally resolved AQ(G)Ps listed in Table 1: (i) those for which experimental p_f values are available (individual measurements or averages thereof, as compiled in Table S1), comprising 10 AQ(G)Ps: bAQP0, oAQP0, bAQP1, hAQP1, hAQP2, hAQP4, rAQP4, mAqPM, eAqPZ and eGlpF (see Table S1 and Fig. 2); and (ii) those for which corrected unitary permeabilities, p_f^{corr} , are reported by Wachlmayr *et al.* [56], comprising 8 AQ(G)Ps: oAQP0, bAQP1, hAQP1, hAQP2, hAQP4, rAQP4, eAqPZ and eGlpF (see Table S2 and Fig. 2). This second set of AQ(G)Ps with available p_f^{corr} values is indeed a subset of the first one.

When compiling the p_f^{corr} data from Ref. [56], we followed the authors' recommendation that osmotic permeabilities should preferably be measured at low temperature (<10 °C) to minimize systematic errors. Thus, we applied a temperature-based filtering to maximize internal consistency of the corrected permeability dataset: measurements performed above 10 °C, as well as entries with unreported temperature were discarded (with the sole exception of sheep AQP0, for which only one value at 15 °C was available and was retained). In this context, in cases where multiple low-temperature permeabilities are reported for the same AQ(G)P, we averaged their p_f^{corr} values to obtain a single representative corrected permeability per aquaporin (Table S2).

For QSAR modeling, unitary permeabilities were expressed on a common numerical scale ($\times 10^{-14}$ cm³·s⁻¹, after which the 10^{-14} factor was removed prior to log-transformation. We thus used $\ln(p_f)$ or $\ln(p_f^{corr})$ as the response variable in the QSAR modeling. This log transformation was necessary because p_f and p_f^{corr} spans approximately two and four orders of magnitude, respectively, and their values are not evenly distributed (Table S2). The log transformation compresses the dynamic range, reduces the influence of extreme values, and yields a distribution closer to normality, thereby facilitating model fitting and interpretation.

The scenario outlined above, further enables us to assess how the use of uncorrected versus corrected permeability values impacts predictive performance and, critically, the physicochemical interpretability of the resulting QSAR models. Importantly, the analysis and discussion presented below are

intended in a constructive spirit—aimed at contributing additional evidence to the ongoing effort to refine experimental permeability measurements in narrow water channels such as AQ(G)Ps—rather than to endorse or disparage any particular experimental or analytical approach.

2.3. Pore Descriptors

Different computational resources were used to obtain or derive pore features (hereafter ‘pore descriptors’, PDs). Geometric PDs (including averaged pore diameter, minimum pore diameter and regularity) and pore-lining amino acid composition were obtained using the PoreWalker server [99]. Per-residue hydrophathy (Kyte–Doolittle index [100]) was computed in Discovery Studio [101]. The Kyte–Doolittle hydrophobicity scale ranges from -4.5 , the most hydrophilic value for Arg, to 4.5 , the most hydrophobic value for Ile, with Gly being the most amphipathic residue (-0.4). PDs providing an indirect proxy for local mobility/flexibility were derived from crystallographic atomic displacements (B-factors) extracted from the PDB files. Finally, H-bonding- and electrostatic/solvation-related PDs were calculated following procedures analogous to those described by Horner *et al.* in Ref. [57] and Ref. [58], respectively (see Fig. 3).

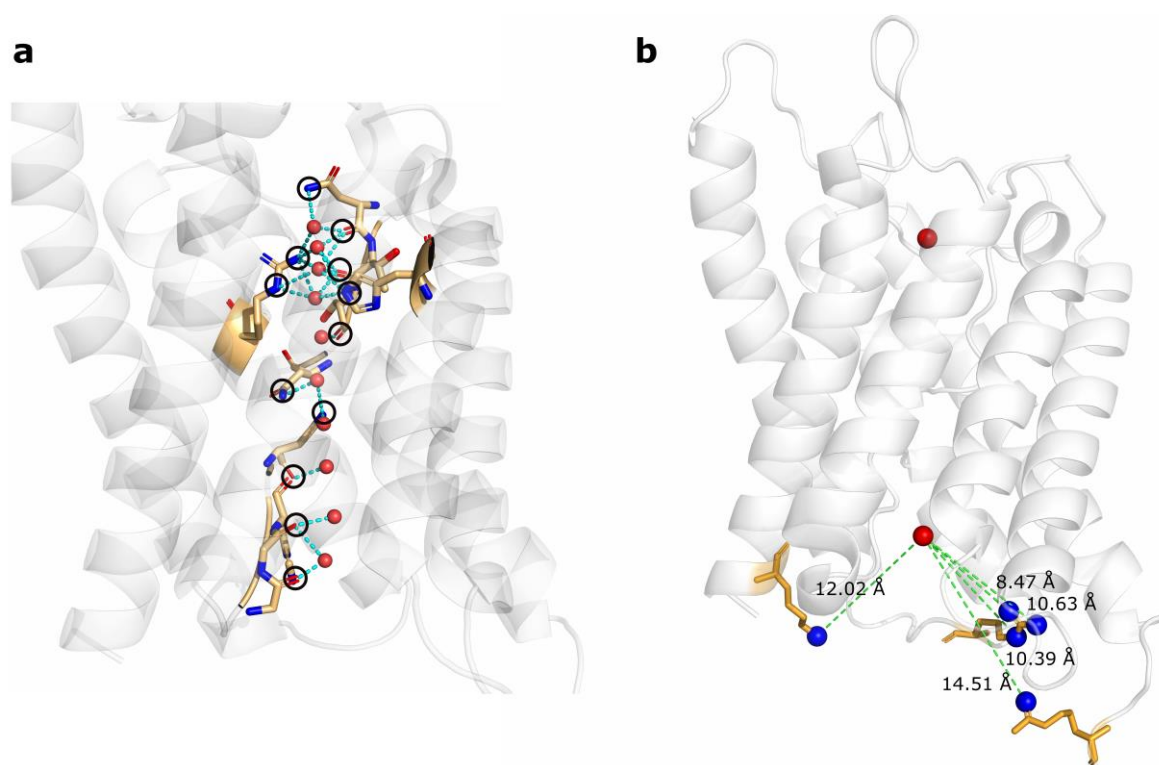


Figure 3. Schematic illustration for eAqpZ (PDB ID: 1RC2) showing the computed number of potential pore-lining hydrogen-bonds (N_H), charged residues and charged sites located in the periplasmic and cytoplasmic pore vestibules. (a) Calculated potential H-bonding sites ($N_H = 12$, black circles) along the single-file region

of eAqpZ. The single-file water column (red spheres) was defined following exactly the procedure described by Horner *et al.* [57]: water coordinates were taken from the 0.88 Å-resolution yeast AQP1 structure (PDB ID: 3ZOJ) [80] after structural superposition onto eAqpZ. Putative hydrogen bonds (cyan dashed lines) were identified using a 3.8 Å distance cut-off. (b) Positively charged Lys and Arg residues ($Res^+ = 3$, tan-colored sticks), and associated charged side-chain nitrogen atoms ($Sites^+ = 5$, blue spheres) counted within the pore cytoplasmic vestibule in eAqpZ, according to the established 15 Å cut-off to the reference waters (red spheres) represented on both the periplasmic and cytoplasmic sides. The red spheres mark the oxygen atoms of the first water molecules flanking the single-file water column, i.e., waters that are no longer part of the continuous single-file chain traversing the pore. Their coordinates were also taken from the above-mentioned yeast AQP1 structure (PDB ID 3ZOJ) [80] after structural superposition onto eAqpZ. The numbers next to the green dashed lines indicate the distances (Å)—all below the 15 Å cut-off (same defined by Horner *et al.* [58])—computed between each water oxygen atom (red spheres) and the charged side-chain nitrogen atoms (blue spheres) of the identified Lys and Arg residues within the same outer vestibule. Custom Python scripts were developed to compute these PDs and the rest of related pore features (see Table 2), including the number of negatively charged residues (Res^- , Glu and Asp) and charged sites/atoms ($Sites^-$) located in the pore vestibules.

When using the PoreWalker tool [99], the initial chain of each AQ(G)P structure was uploaded to the server for calculation. The PoreWalker output (a summary .TXT file is provided in the **Supplementary Information** for every AQ(G)P studied) includes the pore diameter profile along the pore z-coordinate, the 3D shape regularity percentage, 2D projection of the pore shape, cross-sectional images of the pore, as well as the list of amino acids lining the pore.

To carry out the present pore-level QSAR modeling, we first equalized the pore z-coordinate across the AQ(G)Ps with p_f and/or p_f^{corr} data compiled (Fig. 2 and Tables S1-S3). This was done by aligning all the pores along the z-axis, using as a common reference point the β -carbon (βC) of the asparagine residue in the second NPA motif. The βC coordinate was thus set to $z = 0$ (Table S3, Fig. 4a, and left panels in Fig. S1). After alignment, z-coordinates outside the range of -20 and 17.5 Å were not considered (Fig. 4f). This sectional “trimming” was motivated by the observation that pore diameter profiles for several AQ(G)Ps (obtained by PoreWalker [99]) showed artifactually elongated z-coordinates at either the intracellular or extracellular end, or both (see Fig. 4 and Fig. S1). In these regions, the pore shape is less well defined, making it difficult to unambiguously determine the residues lining the channel.

Table 2. Overview of the pore descriptors computed and analyzed in this work.

Pore Descriptor (PD)	PD Short Name	PD Type	Description & Computation
Averaged diameter	<i>Ave_diam</i>	Geometric	Diameter average computed from the diameter versus z-coordinate data provided by Pore-Walker server [99], along the pore z-coordinate-‘trimming’ analyzed. Computed by a custom script.
Minimum diameter	<i>Min_diam</i>	Geometric	Minimum diameter identified from the diameter versus z-coordinate data provided by the Pore-Walker server [99].
3D shape regularity	<i>Reg</i>	Geometric	Measure of how uniformly the pore geometry (cross-sectional symmetry) is maintained along the channel axis (z-coordinate). Reported by the PoreWalker server [99] as a percentage.
Averaged hydrophobicity indexes on pore-lining residues	<i>Ave_hydropho</i>	Hydrophathy	Average of per-residue hydrophobicity along the pore z-coordinate-‘trimming’ analyzed. Hydrophathy indexes from the the Kyte-Doolittle scale [100], computed by Discovery Studio [98]. <i>Ave_hydropho</i> accounts for strictly hydrophobic amino acids (i.e., those with positive hydrophobicity).
Averaged hydrophilicity indexed on pore-lining residues	<i>Ave_hydrophi</i>	Hydrophathy	Average of per-residue hydrophilicity along the pore z-coordinate-‘trimming’ analyzed. Hydrophathy indexes from the Kyte-Doolittle scale [100], computed by Discovery Studio [98]. <i>Ave_hydrophi</i> accounts for strictly hydrophilic amino acids (i.e., those with negative Kyte-Doolittle hydrophobicity). These negative indexes were converted into positive values—by multiplying by -1— to favor better interpretability.
Averaged per-residue B-factor on pore-lining residues within the selectivity filter region	<i>SF_Ave_Bfac</i>	Mobility/flexibility	Average of per-residue displacement (B-factor) on those residues located within the pore z-coordinate 2-6 Å (see Fig. 4a and Fig. S1). B-factor values extracted from the PDB files using a custom script.
Average side chain B-factor on pore-lining residues within the selectivity filter region	<i>SF_Ave_Bfac_SC</i>	Mobility/flexibility	Average of per-residue side-chain displacement on those residues located within the pore z-coordinate 2-6 Å (see Fig. 4a and Fig. S1). Extracted from the PDB file by a custom script.

Table 2. Continuation...

Pore Descriptor (PD)	PD Short Name	PD Type	Description & Computation
Averaged backbone B-factor on pore-lining residues within the selectivity filter region	<i>SF_Ave_Bfac_BB</i>	Mobility/flexibility	Average of per-residue backbone displacement on those residues located within the pore z-coordinate 2-6 Å (see Fig. 4a and Fig. S1). Extracted from the PDB file by a custom script.
Averaged B-factor on pore-lining residues	<i>Ave_Bfac</i>	Mobility/flexibility	Average of per-residue displacement on all the residues lining the pore. B-factor values extracted from the PDB files using a custom script.
Averaged side chain B-factor on the pore-lining residues	<i>Ave_Bfac_SC</i>	Mobility/flexibility	Average of per-residue side chain displacement on all the residues lining the pore. B-factor values extracted from the PDB files using a custom script.
Averaged backbone B-factor on the pore-lining residues	<i>Ave_Bfac_BB</i>	Mobility/flexibility	Average of per-residue backbone displacement on all the residues lining the pore. B-factor values extracted from the PDB files using a custom script.
Number of potential H-bonds with pore-lining residues along the single-file region	N_H	H-bonding	Number of potential H-bonding sites along the single-file region. The single-file water column defined following exactly the procedure described by Horner <i>et al.</i> [93] (see the caption of Fig. 3, panel a).
Positively charged Lys and Arg residues in the pore vestibules	Res^+	Electrostatic/solvation	Number of positively charged Lys and Arg residues counted within the pore outer vestibules (with side-chain nitrogen atoms within 15 Å distance cut-off to the reference waters in their own vestibule, see Fig. 3, panel b). It is a measure of enrichment of positively charged sites at the pore mouths, computed by a custom script.
Positively charged side-chain nitrogen atoms from Lys and Arg in the pore vestibules	$Sites^+$	Electrostatic/solvation	Number of positively charged side-chain nitrogen atoms from Lys and Arg residues counted within the pore outer vestibules (within 15 Å distance cut-off to the above-mentioned reference waters, see Fig. 3, panel b). It is another measure of enrichment of positively charged sites at the pore mouths, computed by a custom script.

Table 2. Continuation...

Pore Descriptor (PD)	PD Short Name	PD Type	Description & Computation
Negatively charged Glu and Asp residues in the pore vestibules	<i>Res⁻</i>	Electrostatic/solvation	Number of negatively charged Asp and Glu residues counted within the pore outer vestibules (with side-chain oxygen atoms within 15 Å distance cut-off to the above-mentioned reference waters. It is a measure of enrichment of negatively charged sites at the pore mouths, computed by a custom script.
Positively charged side-chain nitrogen atoms from Lys and Arg in the pore vestibules	<i>Sites⁻</i>	Electrostatic/solvation	Number of negatively charged side-chain oxygen atoms from Asp and Glu residues counted within the pore outer vestibules (within 15 Å distance cut-off to the above-mentioned reference waters). It is another measure of enrichment of negatively charged sites at the pore mouths, computed by a custom script.

0

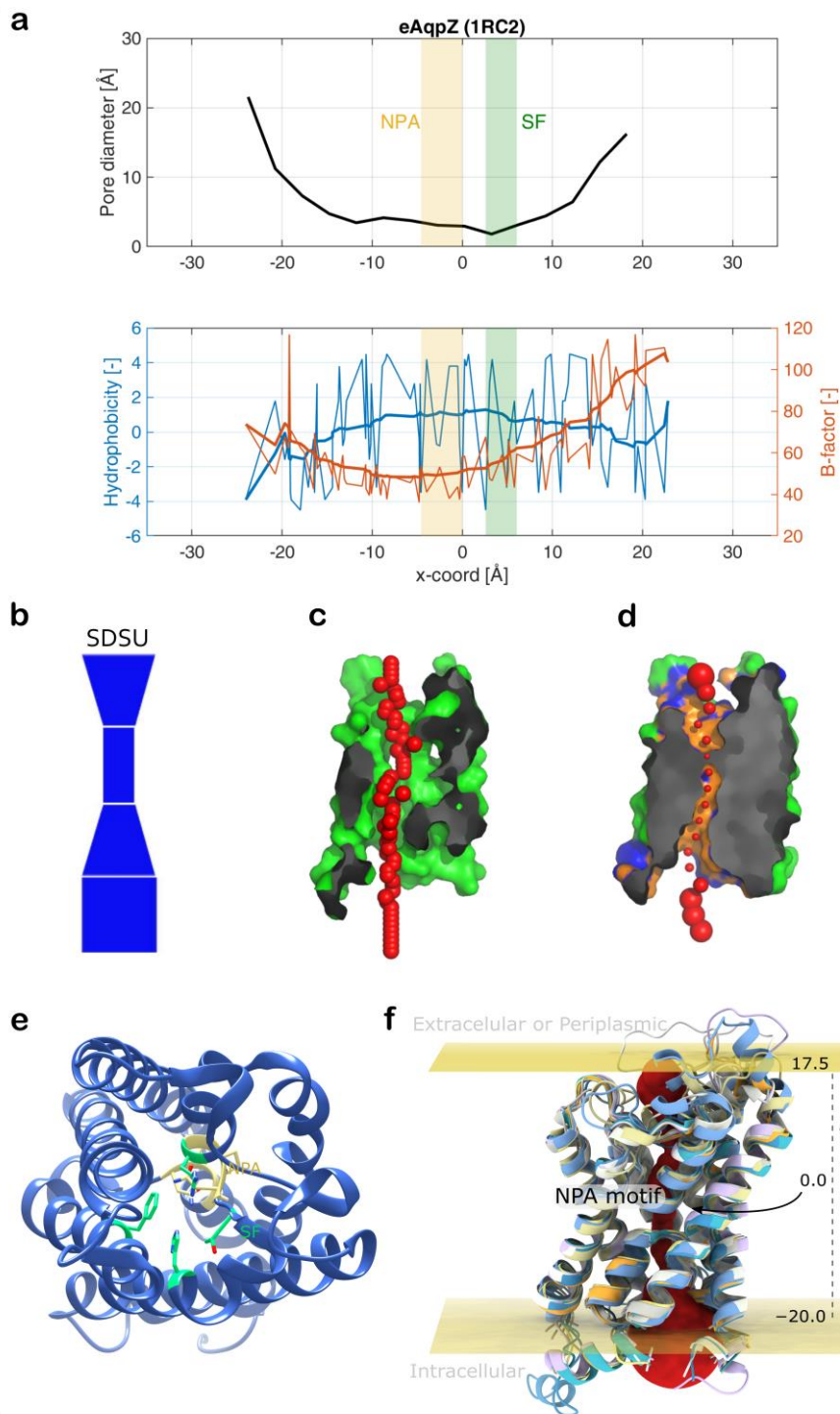


Figure 4. Pore properties profiles and geometrical shape for *Escherichia coli* aquaporin Z (eAqpZ, PDB ID 1RC2), and scheme showing the z-coordinates equalization of the AQ(G)Ps modeled in this work. (a) Top panel: diameter profile along the pore principal axis (z-coordinate) at 3Å step as calculated by the PoreWalker tool [99]; bottom panel: per-residue hydrophobicity index (blue) and B-factor (orange) of amino acids in the pore lining along the pore z-coordinate, as calculated by Discovery Studio (BIOVIA, Dassault Systèmes) [101] and as obtained from the crystal PDB file (1RC2), respectively. The thicker lines are smooth curves (noise removed). Vertical bands show the z-coordinates ranges where the NPA (orange) and SF (green) motifs are located. (b) Funnel-like form representing a 2D projection of the predicted pore shape as calculated by variations of diameter values along the pore: the bottom of the pore axis (i.e. the lowest z-coordinate) corresponds to the bottom of the stack. In the letter

1
2
3
4
5
6
7
8
9
10

code on the top of the form, 'D' indicates a conical frustum generated by decreasing pore diameter values, i.e. the diameter of the lower base of the frustum is bigger than the diameter of its upper circle, 'U' indicates the opposite conical frustum, i.e. lower base diameter smaller than upper base diameter, and 'S' indicates a cylinder (the code ordering from bottom to top). (c) and (d) Longitudinal cross-sectional images of the pore issued by PoreWalker, where the pore regularity is shown through red spheres located at the centre of the pore every 1 Å step (c), whereas the pore dimension is represented by red spheres—at the center of the pore at 3 Å step—whose sizes are proportional to the pore diameter calculated at that point (d). In the latter, orange and blue areas show pore-lining atoms and corresponding residues, respectively. (e) Cartoon representation of a single monomer of *E. coli* aquaporin Z (PDB ID: 1RC2), viewed from the extracellular side. The NPA motifs are shown as sticks in pale yellow (residues 63–65 for NPA-1 and 186–188 for NPA-2), and the selectivity filter residues (F43, H174, T183, and R189) are shown as green sticks. (f) Scheme showing the z-coordinates equalization performed on the modeled AQ(G)Ps. The central red yarn ball-like form approximately represents the pore diameter of one of the aligned AQ(G)Ps. **Notes:** Amino acids in the pore lining are reported in the PoreWalker's output files (**Supplementary Files**). The z-coordinates in the properties profiles (a) were shifted from the original ones issued by PoreWalker, to place the beta carbon (β C) of the asparagine (N) in the second NPA motif at the center of the z-coordinate system ($z=0$). This ensures that all the AQ(G)Ps are aligned to have the same reference z-coordinate, as showed in panel f.

Trimming the pore ends therefore helps to reduce the uncertainty in identifying the pore-lining residues and allows the application of a uniform framework across all the AQ(G)Ps, thereby enabling a more consistent calculation of pore properties, including average diameter, hydrophobicity, and B-factor-related pore descriptors.

All in all, thirteen (13) pore descriptors (PDs) were selected to conduct the pore-level QSAR modeling proposed in this study. Table 2 contains an overview of these PDs. A subset (*Reg*, *SF_Ave_Bfac*, *SF_Ave_Bfac_BB* and *SF_Ave_Bfac_SC*) was first scaled to the 0–10 range. Then, standardization was applied to selected descriptors included in the QSAR models. These preprocessing steps were implemented to minimize scale-related bias during model training.

2.4 Pore-level QSAR Modeling and Performance Assessment

Given the limited number of AQ(G)Ps with compiled values of p_f or p_f^{corr} ($n = 10$ and $n = 8$, respectively) among those listed in Table 1, we use these entire sets to train the models. These two training datasets—containing the unitary log-transformed water permeabilities ($\ln(p_f)$ or $\ln(p_f^{corr})$) together with the calculated PDs—are provided as **Supplementary Files** in CSV format.

The iterative regularization technique LASSO (Least Absolute Shrinkage and Selection Operator [102]) was used, along with the Ordinary Least Squares (OLS) multiple linear regression method (MLR), to select optimal combinations of PDs for QSAR modeling. LASSO repeatedly fits a regression model

by applying an L1 penalty so that small coefficients are shrunk to zero, thereby removing irrelevant variables and helping to prevent overfitting and multicollinearity.

Statistical parameters obtained to assess the performance of the QSAR models include: R-squared (R^2 , internal coefficient of determination), regression p -value (from a Fisher F-test), statistical significance (from a Student t-test, $\alpha=0.05$) for each independent variable (PD) in the models and the independent term, as well as the predictive parameters: SPRESS: Standard Prediction Error Sum of Squares, and $loo\text{-}Q^2$ (leave-one-out cross-validation coefficient).

Regarding the parameters mentioned above, R^2 is a measure of how well the model fits the data used to train the model (desirable R^2 is close to 1, whereas R^2 close to 0 denotes bad performance). The $loo\text{-}Q^2$ parameter is a measure of the internal predictive ability, and not just the fit. This metric is obtained after: (i) removing one item from the dataset, (ii) training again the model with the rest of items in the dataset, (iii) predicting the left-out item using the re-trained model. This process is then repeated until every item has been left out once. Then, all the prediction errors are combined into Q^2 . Thus, higher $loo\text{-}Q^2$ (crucially, >0.5 up to 1) means that the model predicts well data internally, whereas low $loo\text{-}Q^2$ means it predicts poorly (basically noise).

To evaluate collinearity among the retained predictors, we inspected the pairwise correlation matrix and calculated variance inflation factors (VIFs) for each final descriptor set. Candidate models displaying pairwise intercorrelations $|r| > 0.5$ and/or $VIF > 5$ were excluded. In addition, the condition number (CN) was calculated to assess the sensitivity of the regression coefficients to perturbations in the data; models with $CN > 5$ were considered numerically unstable and were not pursued further (additional details are provided in the **Supplementary Information**).

A y -scrambling analysis was also conducted. The y -scrambling (also called y -randomization) is a method to assess chance correlation issues. In QSAR, an unscrambled model is the natural relationship that is observed between the dependent Y variable(s) Y and the independent X variable(s). A y -scrambled model, instead, is obtained by deliberately randomizing (shuffling) the Y values in the dataset while keeping X unchanged across the analyzed items. This procedure is done several times so that allows to verify that none of the “randomized” (scrambled) models perform better than the observed (trained) model, thus excluding the possibility that the proposed model is a result of accidentally fitting noise.

For model assessment, we took advantage of the availability of four aquaporins that, despite lacking experimentally resolved 3D structures, have p_f^{corr} permeability values reported in the literature [56]

(Table S2 and Fig. 2). These proteins were used as an external test set to evaluate one of the best-performing models developed in this study for the p_f^{corr} dataset (see **Results and Discussion**). We used AlphaFold2-predicted 3D structures [103,104] for this purpose, and computed the pore descriptors included in the model in the same manner as for the rest of the dataset. Since AlphaFold2 does not provide B-factor information, and its confidence metrics (pLDDT and PAE) have been shown not to be equivalent to experimental B-factors [105,106], we restricted this validation only to the QSAR model that do not rely on B-factor features.

A dedicated Python script was developed to perform all regression, statistical, and y-scrambling analyses. This script is also supplied, together with the AQ(G)P PDB or AlphaFold structure files, as **Supplementary Data**. Further details on the pore-level QSAR modeling implemented in this study can be found in the **Supplementary Information** document.

3. RESULTS AND DISCUSSION

3.1. On AQ(G)Ps' Permeation Rate

Two key functional elements of AQ(G)Ps are their selectivity and permeation properties. In the **Supplementary Information**, we provide a systematic description of the main structural motifs that determine these properties, highlighting the similarities and differences across the representative set of AQ(G)Ps investigated in this study (see Table S4, Fig. S2 and Fig. S3). AQ(G)Ps' pore shape (also analyzed in detail in the **Supplementary Information**), whose conical design—both in the cytoplasmic and the extracellular entrances (Fig. 4b, Fig. 4f and Fig. S1)—ensures the creation of highly permeable water channels [60] that can transport $\sim 10^9$ water molecules per second (per monomer) in a single-file manner [107–110]. Both experimental [1,56,65,107,108,110–112] and *in silico* [8,63,98,109,113] approaches have been devised to measure or simulate the water permeation rate of AQ(G)Ps.

Access to reliable p_f data of AQ(G)Ps is required to unravel the key structure–function relationships to a molecular level, as we intend here. Back in the early 90's, *in vitro* functional assays were developed to measure the osmotic water permeability of membrane water channels. Classical—though still used—swelling assays based either on the microinjection and expression of a transcribed protein sequence (typically the mRNA of the protein channel of interest) in *Xenopus laevis* oocytes (oocytes

swelling assay: OSA) [1] or the reconstitution of the protein in liposomes (proteoliposome swelling as- 104
say: PSA) [107], have been indispensable tools for the estimation of the water permeability (P_f) and, by 105
inference, unitary water permeabilities (p_f) for many AQ(G)Ps. 106

Despite the advances achieved in methodologies for measuring the water permeabilities of 107
AQ(G)Ps [114]—particularly improvements in the physical techniques employed [65]—, the vast major- 108
ity of unitary permeability measurements (p_f) have been obtained by indirect methods that heavily rely 109
on the accurate estimation of the number of channels present in the sample. As stated by Gonzalez 110
and collaborators, innovative methodological efforts are still needed to enable direct experimental 111
measurements of the events occurring in water molecules inside AQ(G)P channels [51]. In the last 112
decade, although still insufficient, some efforts have been made to obtain more direct permeation meas- 113
urements [97] and to apply improved experimental strategies [115]. 114

Notably, recent re-analyses have suggested that a non-negligible fraction of legacy stopped-flow– 115
derived osmotic and unitary permeability estimates may be systematically overstated (up to 75%), ow- 116
ing to methodological assumptions that were common in earlier studies [56]. This has two practical 117
implications for comparative structure–function analyses: first, absolute p_f values across the literature 118
should be interpreted with caution unless they derive from modern analysis pipelines or include explicit 119
corrections; and second, relative rankings and broad trends are generally more robust than the original 120
numerical magnitudes. 121

On the computational side, most approaches have relied on molecular dynamics simulations (MDS), 122
including simulations under equilibrium conditions [63,98,116–123], pressure-induced [98], and steered 123
molecular dynamics [113]. However, Zhu et al. [98] reported that equilibrium MDS is not a reliable 124
method for computing osmotic unitary water permeabilities and suggested instead imposing a hydro- 125
static pressure difference across the membrane to better approximate experimental conditions [98]. 126
Despite these limitations, MDS-based approaches—unlike experimental methods—enable the direct 127
computation of p_f under fully controlled conditions and have provided invaluable atom– and residue– 128
level insights into filtration mechanisms, selectivity, and proton exclusion [50,63,85,98,117]. Moreover, 129
they hold the potential to deepen our understanding of the behavior of protein channels in lipid mem- 130
branes and to enable detailed thermodynamic and stability analyses [124,125]. Such analyses may 131
help rationalize, and ultimately mitigate, the stability issues reported for several AQ(G)Ps [36]. 132

133

3.2. Pore-level QSAR Study as a Methodological Proof of Concept	134
3.2.1. Pore Descriptors (PDs)	135
Several mechanistic studies have already attempted to quantitatively dissect how specific pore features modulate the unitary water permeability of narrow AQ(G)Ps, albeit typically by interrogating one factor at a time and/or using limited protein sets.	136 137 138
In particular, Horner <i>et al.</i> [57] proposed that single-file water mobility is governed by the number of potential hydrogen-bonds (N_H) between permeating waters and pore-lining residues, with transport limited by the kinetics of breaking and reforming these interactions during translocation. Closely related work further highlighted the role of entrance/exit dehydration–rehydration energetics, showing that the electrostatic environment at the pore mouth (e.g., enrichment of positively charged residues) can measurably boost p_f even when the single-file H-bonding capacity is held constant, based on comparisons across a small panel of AQPs [58].	139 140 141 142 143 144 145
Complementary MDS-based analyses likewise indicated that permeability is not dictated by pore radius alone, but reflects a competition between channel geometry and the degree of single-file character along the permeation pathway [117]. Finally, experimental mutagenesis combined with <i>in silico</i> pore profiling has reinforced that subtle variations in constriction geometry and local physico-chemistry can differentially impact permeation [126], underscoring that “pore size” is rarely a sufficient standalone descriptor.	146 147 148 149 150 151
Notwithstanding these important advances—including the broader recognition that gating/regulatory phenomena can reversibly switch AQ(G)Ps between more and less permeable states under specific modulators (e.g., pH, ions, phosphorylation), adding another structural layer to consider—only a small number of pore descriptors have been rigorously benchmarked against extensive, harmonized experimental p_f datasets to date. This motivates a dedicated descriptor framework for the pore-lining environment, in which geometric, H-bonding, electrostatic/solvation-related features, and other features are systematically encoded and evaluated jointly within a unified quantitative modelling context.	152 153 154 155 156 157 158
In the proposed pore-level QSAR modeling, we consider all pore features described above and additionally include descriptors that, to our knowledge, have not been systematically examined in the literature on determinants of water permeation, such as pore regularity and hydrophobicity- and B-factor-related pore descriptors (see Table 2).	159 160 161 162

Computed hydrophobicity profiles (Fig. 4a and Fig. S1) show significantly more hydrophobic residues (positive indexes) lining the pore than hydrophilic ones (negative indexes), in agreement with previous reports [127,128]. These differences are less pronounced near and at the intra- and extracellular pore vestibules, where the pore diameter and water contact surface increase, and there is a higher concentration of hydrophilic residues. The hydrophobicity profiles, thus, predominantly show a downward bell-shaped smoothed curve, with the peak located around the central part of the pore, where the NPA and SF motifs are situated. It is important to note that, although hydrophobic residues predominate—particularly in the central region of the pore—the presence of hydrophilic residues interspersed among them could be essential for water passage [62,117]. In relation to this, a pore lining composition analysis of the AQP(G)Ps listed in Table 1 is provided in the **Supplementary Information** (see Fig. S4) for the reader's reference.

Moreover, B-factor profiles display the opposite shape, that is, an upward bell smoothed curve (Fig. 4a and Fig. S1). The B-factor values, which are typically derived from fitting X-ray diffraction data, measure the atomic displacement in molecular structures, indicating how much atoms deviate from their average positions due to thermal motion or structural disorder. According to these graphs, residues in the pore with the lowest B-factors are located in the region encompassing the pore constriction sites, namely the SF and NPA motifs. This is likely due to the proximity of the pore walls, which facilitates the formation of interaction networks that are crucial for the transport and selectivity exhibited by these proteins. Accordingly, within our QSAR framework, we evaluated B-factor–derived descriptors at the whole-residue, backbone, and side-chain levels, computed as averages over residues in the selectivity filter region as well as over the all pore-lining residues for the AQP(G)Ps analyzed.

We additionally computed B-factor descriptors at the whole-protein level and for the extra-pore region (i.e., non–pore-lining residues) using the same structure alignment and pore-trimming workflow. However, none of these descriptors was statistically significant and, accordingly, they provided no informative signal in our tests. These descriptors are therefore not included in Table 2, which focuses on pore-related descriptors. Instead, their computed values are provided in the **Supplementary Information** as a separate file for transparency.

3.2.2. Pore-level QSAR Models: Performance and Mechanistic Insights

We present here the best-performing models ($R^2 > 0.9$ and $\text{loo-Q}^2 > 0.6$) obtained for the two permeability datasets, following the criteria defined in Section 2.4: (1) AQP(G)Ps with compiled p_f ($n=10$), and

(2) AQP(G)Ps with compiled p_f^{corr} (n=8). Candidate QSAR models containing four or more PDs exhibited substantial multicollinearity and/or instability and were therefore discarded, even when their apparent goodness of fit was high (data not shown).

Model 1.3 (uncorrected permeabilities; n = 10):

$$\ln(p_f) = -1.38(\pm 0.21) * N_H + 0.98(\pm 0.20) * SF_Ave_Bfac_SC - 1.18(\pm 0.22) * Sites^- + 0.83(\pm 0.19)$$

This model exhibits an excellent fit ($R^2 = 0.92$; Adj. $R^2 = 0.88$; Prob(F) = 0.001) together with moderate-to-good internal predictivity (loo- $Q^2 = 0.71$). In real-scale terms, predicted p_f values remained within the same order of magnitude as the experimental (observed) values across all cases. The largest absolute deviation ($12.5 \times 10^{-14} \text{ cm}^3 \cdot \text{s}^{-1}$) was observed for the highest permeability channel (rat AQP4; Table 4 and Fig. 5a), which is an expected feature of small-n QSAR models where high-leverage points can dominate.

The strongest effect in Model 1.3 is the negative coefficient for N_H , defined as the number of potential H-bonding sites along the single-file region. This indicates that increasing the density of H-bond-capable pore-lining residues is associated with reduced water permeability. The direction of this effect is consistent with the single-file transport framework, in which wall–water H-bonding introduces kinetic friction: permeating waters must repeatedly break and reform interactions with pore-lining residues, slowing collective motion through the constriction. The dependence on N_H in Model 1.3 is also consistent with prior work by Horner *et al.* [57], who reported an inverse relationship between p_f and N_H across a small set of AQ(G)Ps, protein channels, and nanotubes.

The positive coefficient for $SF_Ave_Bfac_SC$ (average side-chain displacement/B-factor for residues within $z = 2-6$, i.e., around the selectivity filter) suggests that greater local side-chain mobility in the constriction region correlates with increased water permeability in this dataset. A plausible mechanistic interpretation is that moderate flexibility could transiently relax steric or interaction constraints, smoothing the free-energy landscape for single-file water translation (e.g., by reducing the persistence of “sticky” configurations). However, because B-factors conflate genuine dynamics with crystal packing, resolution, and refinement procedures, this descriptor should be interpreted cautiously as a proxy for flexibility rather than a direct dynamical observable.

The negative coefficient for $Sites^-$ indicates that a higher density of negatively charged sites in the outer vestibules is associated with reduced p_f in this dataset. This observation is compatible with, but

also extends, previous mechanistic analyses of aquaporin entrances. In particular, Horner *et al.* reported a clear positive association between positively charged residues at the channel mouth and single-file water flow, whereas the contribution of negatively charged residues appeared comparatively marginal in the small set of channels examined [58]. In Model 1.3, however, the LASSO procedure retained $Sites^-$ —defined not as the number of negatively charged residues, but as the number of negatively charged oxygen atoms from Asp/Glu side chains within a defined vestibular proximity to reference waters (see Table 2)—suggesting that a more fine-grained representation of vestibular anionic functionality may capture effects that are not resolved by residue counts alone.

A plausible interpretation is that vestibular anionic groups can oppose water entry and throughput by increasing the energetic cost of reorganizing hydration upon approach to the pore mouth, thereby counteracting the permeability-enhancing effect of cationic sites (with a lower desolvation penalty, see discussion below for Model 2.3b) [58]. In addition, an increased abundance of Asp/Glu oxygen atoms provides additional opportunities for transient water–protein hydrogen bonding in the vestibular regions, which could slow water exchange into the single-file pathway by raising the local residence time and effectively increasing friction before and/or after the principal constriction. These mechanisms are not mutually exclusive and may act in concert. Given the limited sample size ($n = 10$), the contribution of $Sites^-$ is best interpreted as a mechanistically plausible association that merits targeted validation, rather than as a definitive causal determinant of p_f .

Model 2.3a (corrected permeabilities; $n=8$):

$$\ln(p_f^{corr}) = -0.53(\pm 0.21) * SF_Ave_Bfac_SC - 0.77(\pm 0.21) * Reg - 1.55(\pm 0.21) * N_H + 1.57(\pm 0.20)$$

This model shows an excellent goodness-of-fit ($R^2 = 0.95$; Adj. $R^2 = 0.92$; Prob(F) = 0.004) but a more modest internal predictability (loo- $Q^2 = 0.63$). In real-scale terms, predicted p_f^{corr} values remained within the same order of magnitude as the compiled (observed) permeabilities across all AQ(G)Ps. The largest absolute deviation was observed for *E. coli* GlpF ($26.8 \times 10^{-14} \text{ cm}^3 \cdot \text{s}^{-1}$; Table 4 and Fig. 5b).

Notably, N_H remains a dominant negative term, reinforcing the robustness of the H-bond friction concept across datasets. The negative coefficient for *Reg* (PoreWalker-derived regularity [100]) suggests that a more uniform pore geometry along the pore axis is associated with lower permeability in the corrected dataset. At this stage, *Reg* is best viewed as a global structural correlate of permeability rather than a direct mechanistic determinant. Clarifying its physical meaning will likely require a more

detailed analysis that resolves local radius variations along the pore and quantifies how these features couple to the free-energy barriers governing single-file water flow.

In contrast to Model 1.3, the coefficient associated with $SF_Ave_Bfac_SC$ is negative in Model 2.3a. However, this term also displays the smallest effect size among the selected predictors (-0.53 in standardized units) and the weakest statistical support within the model ($P > |t| = 0.064$, whereas the remaining terms show P -values ≤ 0.01). Taken together, the modest magnitude, marginal significance, and sign reversal relative to the non-corrected-permeability model suggest that B-factor-derived descriptors could be particularly sensitive to changes in the response definition (i.e., corrected versus non-corrected permeabilities) and to dataset composition. In addition, the training set comprises structures obtained under heterogeneous experimental conditions (including resolution, temperature, pH, crystallization/buffer conditions, and structure-determination method; see Table S6), all of which can influence crystallographic displacement parameters and limit the direct comparability of B-factors across AQ(G)Ps. Accordingly, at this stage, the $SF_Ave_Bfac_SC$ term should be interpreted cautiously and revisited once a larger dataset becomes available.

Model 2.3b (corrected permeabilities; $n=8$):

$$\ln(p_f^{corr}) = 0.39(\pm 0.39) * Sites^+ - 0.95(\pm 0.33) * Reg - 1.59(\pm 0.35) * N_H + 1.57(\pm 0.29)$$

This model also provides a strong fit ($R^2 = 0.90$; Adj. $R^2 = 0.826$; Prob(F) = 0.018) together with similar moderate internal predictivity (loo- $Q^2 = 0.65$). In real-scale terms, predicted p_f^{corr} values remained within the same order of magnitude as the compiled (observed) permeabilities for all channels, with the exception of *E. coli* GlpF, for which the absolute discrepancy reached $46.6 \times 10^{-14} \text{ cm}^3 \cdot \text{s}^{-1}$ (Table 4 and Fig. 5c). Relative to Model 2.3a, Model 2.3b replaces the $SF_Ave_Bfac_SC$ descriptor with $Sites^+$, defined as the number of positively charged Lys/Arg side-chain nitrogen atoms within the pore vestibules (Table 2). The positive coefficient for $Sites^+$ is consistent with previous evidence that positive charges at the pore mouth (entrances/exits) can boost water flow [58]. Accordingly, Model 2.3b supports the interpretation that vestibular cationic groups may facilitate water entry and/or reduce the energetic penalty associated with reorganisation of hydration at the pore mouth, thereby promoting the initiation and maintenance of the single-file water column.

Importantly, Model 2.3b is the most amenable to external testing among the QSAR models presented here, as it relies on descriptors that can be computed from AlphaFold2 [103,104] structures (in contrast to B-factor-based terms). External evaluation on four AQPs (rAQP8, mAQP11, RsAqpZ and

sAQP) shows good overall agreement between predicted and compiled p_f^{corr} values (Fig. 5d), with $R_{Ext}^2 = 0.898$. In real-scale terms, absolute deviations ranged from 0.85 to $8.77 \times 10^{-14} \text{ cm}^3 \cdot \text{s}^{-1}$; in relative terms, three AQPs were predicted within ~2-fold (rAQP8, mAQP11 and RsAqpZ), whereas the lowest-permeability case (sAQP) was overestimated (~6.5-fold). Given the very small external set (n = 4) and the wide range in p_f^{corr} values across this subset of AQPs, these results should be interpreted as preliminary evidence of transferability rather than as a definitive validation.

Overall, N_H displays a consistent negative association with permeability across all models, supporting the view that an increased density of potential wall–water hydrogen-bonding sites in the single-file region imposes an effective friction that limits water throughput. By contrast, descriptors derived from crystallographic B-factors show dataset-dependent behavior, including a reversal in coefficient sign between the non-corrected and corrected permeability datasets, reinforcing their interpretation as empirical proxies rather than robust mechanistic determinants. Importantly, vestibular electrostatics emerge as a complementary modulator of permeability: the positive association of $Sites^+$ with p_f^{corr} , together with the negative trend observed for $Sites^-$ in the non-corrected dataset, is consistent with the notion that charge distribution at the pore mouth can influence water entry/exit by altering hydration reorganization and the associated desolvation penalty.

From a statistical standpoint, multicollinearity was negligible (VIF ≈ 1 –1.76; condition number ≤ 2.21) across all models, supporting coefficient stability and interpretability. Moreover, y-scrambling analysis (100 permutations; Fig. S5, panels b, d and f) yielded no scrambled model with superior $R^2/loo-Q^2$ compared with the corresponding original model, which argues against chance correlations being responsible for the reported fits. All statistical parameters for the QSAR models are summarized in Table 3, and the per-descriptor LASSO coefficients resulted after the application of the feature-selection procedure are shown in the bar plots in Fig.S5 (panels a, c and e).

Table 3. Best-performing pore-level QSAR models and their associated statistical fit and predictive performance metrics.

Training Dataset ^a	No. PDs in model ^c	Model ID	PD1 (coeff. ± SE) ^d	PD2 (coeff. ± SE) ^d	PD3 (coeff. ± SE) ^d	Indep. term (± SE) ^d	R ²	P-value (F-test)	CN ^e	VIF ^f	loo-Q ^{2g}	SPRESS ^h
1 <i>ln(p_f)</i>	3	1.3	<i>N_H</i> (-1.38±0.21) ^{***}	<i>SF_Ave_Bfac_SC</i> (0.98±0.20) ^{***}	<i>Sites⁻</i> (-1.18±0.22) ^{***}	0.84 ± 0.19 ^{***}	0.92	0.001	1.68	1.20; 1.08; 1.29	0.71	0.87
		2.3a	<i>Ave_Bfac_SC</i> (-0.53±0.21) [*]	<i>Reg</i> (-0.77±0.21) ^{**}	<i>N_H</i> (-1.55±0.21) ^{***}	1.57 ± 0.20 ^{***}	0.95	0.004	1.38	1.07; 1.03; 1.11	0.63	1.12
2 <i>ln(p_f^{corr})</i>	3	2.3b	<i>Sites⁺</i> (0.39±0.38) [*]	<i>Reg</i> (-0.95±0.33) ^{**}	<i>N_H</i> (-1.59±0.35) ^{***}	1.57 ± 0.29 ^{***}	0.90	0.018	2.21	1.30; 1.41; 1.76	0.65	1.09

^aWater permeability datasets used to train the QSAR models presented in the rows: 1) dataset of individual or averaged p_f measurements—without correction—for: bAQP0, oAQP0, bAQP1, hAQP1, hAQP2, hAQP4, rAQP4, mAqpM, eAqpZ and eGlpF (as reported in Table S1 and depicted in Fig. 2); 2) dataset of corrected water permeabilities for: oAQP0, bAQP1, hAQP1, hAQP2, hAQP4, rAQP4, eAqpZ and eGlpF (as reported in Table S2 and depicted in Fig. 2). ^cNumber of PDs included in the QSAR models presented in the rows. ^dS.E. stands for standard error, and the number of asterisks shown over the values indicates the statistical significance (p-value from a Student t-test) obtained for the PDs or the independent term of the models, namely: * if $p < 0.1$, ** if $p < 0.05$, and *** if $p < 0.01$. ^eThe condition number (CN) obtained for each model. A summarized description of CN is given in the **Supplementary Information**. ^fThe Variance Inflation Factor (VIF) for all the variables (PDs) in the models. A summarized description of VIF is also provided in the **Supplementary Information**. ^gloo-Q² is the leave-one-out cross-validation coefficient used to assess the internal predictability of the models. ^hSPRESS stands for Standard Prediction Error Sum of Squares.

Table 4. Measured or corrected water permeation rates (observed), predicted values, and residuals obtained from Models 1.3, 2.3a and 2.3b in Table 3.^a

AQ(G)P (PDB)	Observed	Predicted	Residual	Observed	Predicted	Residual	Observed	Predicted	Residual
	p_f ($\times 10^{-14}$ $\text{cm}^3\cdot\text{s}^{-1}$) ^b	p_f ($\times 10^{-14}$ $\text{cm}^3\cdot\text{s}^{-1}$)	p_f (Pred. minus Obs.)	p_f^{corr} ($\times 10^{-14}$ $\text{cm}^3\cdot\text{s}^{-1}$) ^c	p_f^{corr} ($\times 10^{-14}$ $\text{cm}^3\cdot\text{s}^{-1}$)	p_f^{corr} (Pred. minus Obs.)	p_f^{corr} ($\times 10^{-14}$ $\text{cm}^3\cdot\text{s}^{-1}$) ^c	p_f^{corr} ($\times 10^{-14}$ $\text{cm}^3\cdot\text{s}^{-1}$)	p_f^{corr} (Pred. minus Obs.)
	Model 1.3			Model 2.3a			Model 2.3b		
eGlpF (1FX8)	1.35	2.71	1.36	110.0	83.2	-26.8	110.0	63.4	-46.6
bAQP1 (1J4N)	2.3	2.95	0.65	3.2	2.93	-0.27	3.2	2.75	-0.45
eAqpZ (1RC2)	6.0	4.91	-1.09	7.33	6.75	-0.58	7.33	7.95	0.62
bAQP0 (1YMG)	0.15	0.25	0.1	--	--	--	--	--	--
oAQP0 (2B6O)	0.2	0.21	0.01	0.09	0.11	0.02	0.09	0.11	0.02
rAQP4 (2D57)	23.0	35.5	12.5	7.36	17.94	10.58	7.36	24.52	17.16
mAqpM (2F2B)	0.65	0.46	-0.19	--	--	--	--	--	--
hAQP4 (3GD8)	11.0	10.0	-1.0	11.0	11.5	0.5	11.0	4.45	-6.55
hAQP2 (4NEF)	9.3	6.0	-3.3	3.27	1.89	-1.38	3.27	4.17	0.9
hAQP1 (7UZE)	5.1	2.12	-2.98	4.6	3.77	-0.83	4.6	4.12	-0.48

^aAll unitary permeation rates and their associated residuals are presented on the original (non-log) scale, obtained by back-transforming the modeled log-transformed data.

^bExperimental water permeation rates (averages if more than one is reported for a given AQ(G)P), as listed in Table S1 (original p_f values, i.e., without the correction proposed by Wachlmayr *et al.* [56]). ^cCorrected water permeation rates [56] compiled in Table S2 and Fig. 2.

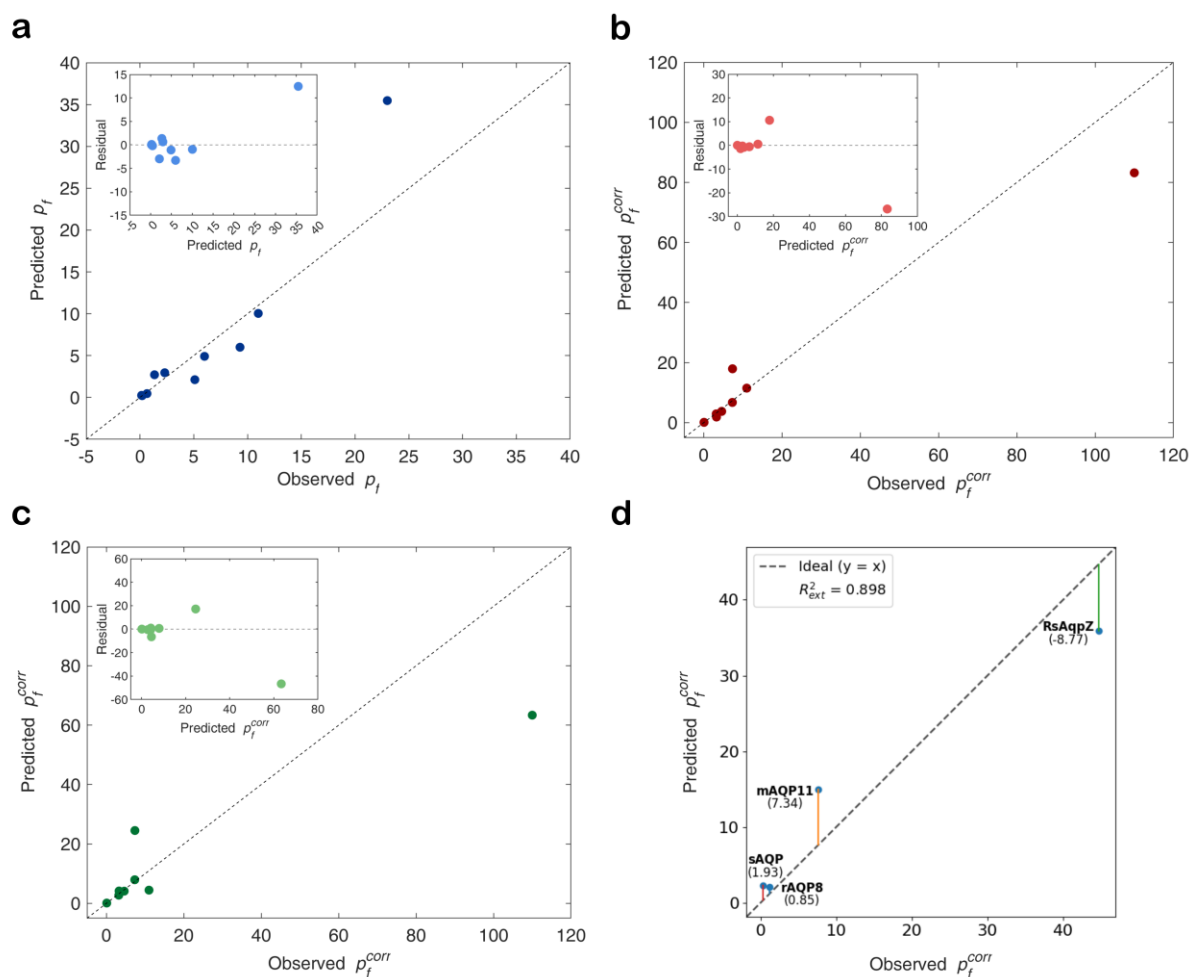


Figure 5. Predictive performance and evaluation of the proposed pore-level QSAR models. (a) Predicted versus observed non-corrected permeability (p_f) values obtained from Model 1.3 (Table 4). (b) Predicted versus observed corrected permeability (p_f^{corr}) values obtained from Model 2.3a (Table 4). (c) Predicted versus observed corrected permeability (p_f^{corr}) values obtained from Model 2.3b (Table 4). In (a-c) the diagonal dashed lines show the 1:1 relationship, and the insets display residuals versus predicted p_f^{corr} . (d) Predicted versus observed p_f^{corr} values obtained with Model 2.3b for an independent set (rAQP8, mAQP11, RsAqpZ and sAQP; Table S6) used for external validation. The diagonal dashed line corresponds to the ideal prediction ($y = x$). The external coefficient of determination ($R^2_{Ext} = 0.898$) indicates a strong overall agreement between observed and predicted values. For each data point, the deviation from the diagonal ($\Delta = \text{predicted} - \text{observed}$) is indicated in parentheses, highlighting over- and under-predictions by the model.

3.2.3. Challenges and Main Limitations of the Proposed Methodology

Modelling water permeation through narrow channels such as AQPs and AQGs remains intrinsically challenging. This complexity stems, on the one hand, from the coupling between local and global phenomena occurring both within and around the pore, including auto-regulatory processes (e.g., pore gating; discussed in more detail in the **Supplementary Information**, Fig. S6) and post-translational

modifications [13,87,129–132]. On the other hand, defining descriptors that faithfully capture the structural and physicochemical determinants of permeation is not straightforward a priori.

In addition, the still limited availability of experimentally determined osmotic permeability coefficients (p_f) across AQ(G)Ps precludes the development of more robust predictive models based on extended training sets and, at the same time, restricts the possibility of reserving independent external test sets for rigorous validation.

Beyond data availability, substantial room remains to devise and validate new pore features / descriptors that encode the physical determinants of pore-mediated filtration and selectivity, an area where computational approaches could play a particularly important role. In this context, MDS-based methodologies could be leveraged to derive dynamic descriptors that go beyond static structural proxies. This perspective is increasingly feasible given the availability of high-quality structure predictors such as AlphaFold [103,104], together with growing access to high-performance computing resources. In particular, AlphaFold-derived structures of AQ(G)Ps can enable descriptor calculation and, consequently, support broader model development and validation—as illustrated here by the external set used to validate Model 2.3b (Table S6)—particularly as larger datasets of AQ(G)Ps with experimentally measured osmotic permeability become available.

It should also be noted that crystal structures, such as those used here, are not fully representative of proteins embedded in a lipid membrane. However, because our modeling framework focuses on the pore region, it is reasonable to assume that pore geometry and key constriction features are comparatively less sensitive to the surrounding membrane environment than other protein regions.

For this study, AQ(G)P structures solved at the highest available resolution were selected. In addition, to avoid biases and minimize inter-structure differences, all B-factor-based descriptors were computed after structural alignment of all AQ(G)Ps and applying identical pore segment definitions (z-coordinate pore trimming in the range of -20 to 17.5 Å). Nonetheless, modest differences remain across structures in terms of resolution, crystallization conditions (e.g., temperature, pH, and solvent), and data-collection protocols across the AQ(G)Ps analyzed here (Table S5). This issue limits direct comparisons between AQ(G)Ps and, particularly for models relying on B-factor features, complicate interpretation in terms of “true” dynamics or flexibility.

Despite these limitations, the good statistical metrics and predictive performance achieved by the selected QSAR models, together with their consistency with previously reported experimental observations (see previous section), render the proposed approach particularly encouraging. Importantly, this framework enables the joint assessment of multiple pore features and their combined effects on permeability. In our view, the results presented here may also motivate continued improvements in experimental procedures for determining osmotic water permeability, as well as the development of richer and more physically grounded pore descriptors, ultimately extending the applicability and robustness of this QSAR framework in future studies. Nonetheless, experimental validation and prospective design tests will be required before any predictive or engineering capability can be firmly established.

3. CONCLUSIONS

A pore-level QSAR approach is proposed to help identify key characteristics influencing water permeation through molecular pores. The best QSAR models achieved, while showing good correlation and moderate-to-good internal predictive performance, still present some limitations due to the scarcity of experimental permeation rate data for AQ(G)Ps, which hinders the use of broader training sets. Nevertheless, this constraint does not diminish the potential of the approach for gaining a deeper residue-level understanding of AQ(G)Ps' filtering properties, particularly by integrating multiple pore descriptors within a single quantitative framework rather than interrogating them individually. We believe that this methodology holds significant promise and, as additional permeation data become available, could yield a more comprehensive view of the pore permeation process. Ultimately, it may also support the rational design of highly efficient AQ(G)Ps or other biomimetic molecules with tailored filtration properties and provide further insights into the molecular mechanisms underlying AQ(G)P-related diseases.

SUPPLEMENTARY INFORMATION

This article has an associated **Supplementary Information** document and **Supplementary Files**.

CRedit authorship contribution statement

J.J.G-F.: Conceptualization, Methodology, Software, Validation, Formal analysis, Investigation, Data curation, Writing - Original draft preparation, Writing - Reviewing and Editing, Visualization, Project ad-

ministration; **L.B.:** Conceptualization, Methodology, Software, Validation, Formal analysis, Investigation, Data curation, Writing - Original draft preparation, Writing - Reviewing and Editing, Visualization, Project administration; **P.V.:** Investigation, Data curation, Writing - Original draft preparation; **M.M.:** Writing - Reviewing and Editing; **M.F.:** Writing - Reviewing and Editing; **D.P.:** Writing - Reviewing and Editing; **E.C.:** Writing - Reviewing and Editing; **M.C.dR.:** Writing - Reviewing and Editing, Supervision.

Data Availability Statement

Files with the raw and processed data, and the custom Python script prepared for the pore-level QSAR modeling can be accessed from: <https://zenodo.org/records/18675157>.

Competing Interests

The authors declare no competing interests.

REFERENCES

- [1] Preston GM, Carroll TP, Guggino WB, Agre P. Appearance of water channels in *Xenopus* oocytes expressing red cell CHIP28 protein. *Science* 1992;256:385–7. <https://doi.org/10.1126/science.256.5055.385>.
- [2] Agre P, Sasaki S, Chrispeels MJ. Aquaporins: a family of water channel proteins. *American Journal of Physiology-Renal Physiology* 1993. <https://doi.org/10.1152/ajprenal.1993.265.3.F461>.
- [3] Agre P, Borgnia MJ, Yasui M, Neely JD, Carbrey J, Kozono D, et al. Discovery of the aquaporins and their impact on basic and clinical physiology. *Curr Top Membr* 2001;51:1–38. [https://doi.org/10.1016/S1063-5823\(01\)51003-0](https://doi.org/10.1016/S1063-5823(01)51003-0).
- [4] Zwiazek JJ, Xu H, Tan X, Navarro-Ródenas A, Morte A. Significance of oxygen transport through aquaporins. *Sci Rep* 2017;7:40411. <https://doi.org/10.1038/srep40411>.
- [5] Lindahl V, Gourdon P, Andersson M, Hess B. Permeability and ammonia selectivity in aquaporin TIP2;1: linking structure to function. *Sci Rep* 2018;8:2995. <https://doi.org/10.1038/s41598-018-21357-2>.
- [6] Wang H, Schoebel S, Schmitz F, Dong H, Hedfalk K. Characterization of aquaporin-driven hydrogen peroxide transport. *Biochimica et Biophysica Acta Biomembranes* 2020;1862:183065. <https://doi.org/10.1016/j.bbamem.2019.183065>.

- [7] Yang B, Verkman A. Water and glycerol permeabilities of aquaporins 1–5 and MIP determined quantitatively by expression of epitope-tagged constructs in *Xenopus* oocytes. *Journal of Biological Chemistry* 1997;272:16140–6. <https://doi.org/10.1074/jbc.272.26.16140>. 409
410
411
- [8] Tajkhorshid E, Nollert P, Jensen MØ, Miercke LJ, O’Connell J, Stroud RM, et al. Control of the selectivity of the aquaporin water channel family by global orientational tuning. *Science (New York, NY)* 2002;296:525–30. <https://doi.org/10.1126/science.1067778>. 412
413
414
- [9] Goto SG, Lee RE, Denlinger DL. Aquaporins in the Antarctic Midge, an Extremophile that Relies on Dehydration for Cold Survival. *The Biological Bulletin* 2015;229:47–57. <https://doi.org/10.1086/BBLv229n1p47>. 415
416
417
- [10] Gautam A, Pandey AK. Aquaporins Responses under Challenging Environmental Conditions and Abiotic Stress Tolerance in Plants. *Bot Rev* 2021;87:467–95. <https://doi.org/10.1007/s12229-021-09249-z>. 418
419
420
- [11] Kapilan R, Vaziri M, Zwiazek JJ. Regulation of aquaporins in plants under stress. *Biological Research* 2018;51:4. <https://doi.org/10.1186/s40659-018-0152-0>. 421
422
- [12] Philip BN, Kiss AJ, Lee RE. The protective role of aquaporins in the freeze-tolerant insect *Eurosta solidaginis*: functional characterization and tissue abundance of EsAQP1. *Journal of Experimental Biology* 2011;214:848–57. <https://doi.org/10.1242/jeb.051276>. 423
424
425
- [13] Yang B, editor. *Aquaporins*. vol. 1398. Second Edition. Singapore: Springer Nature; 2023. <https://doi.org/10.1007/978-981-19-7415-1>. 426
427
- [14] Verkman AS. Aquaporins in Clinical Medicine. *Annu Rev Med* 2012;63:303–16. <https://doi.org/10.1146/annurev-med-043010-193843>. 428
429
- [15] Verkman AS. Aquaporins. *Current Biology* 2013;23:R52–5. <https://doi.org/10.1016/j.cub.2012.11.025>. 430
431
- [16] Azad AK, Raihan T, Ahmed J, Hakim A, Emon TH, Chowdhury PA. Human Aquaporins: Functional Diversity and Potential Roles in Infectious and Non-infectious Diseases. *Front Genet* 2021;12:654865. <https://doi.org/10.3389/fgene.2021.654865>. 432
433
434

- [17] Dutta A, Das M. Deciphering the role of aquaporins in metabolic diseases: A mini review. *The American Journal of the Medical Sciences* 2022;364:148–62. <https://doi.org/10.1016/j.amjms.2021.10.029>.
- [18] Vallese F, Kim K, Yen LY, Johnston JD, Noble AJ, Cali T, et al. Architecture of the human erythrocyte ankyrin-1 complex. *Nature Structural & Molecular Biology* 2022;29:706–18. <https://doi.org/10.1038/s41594-022-00792-w>.
- [19] Krane CM, Goldstein DL. Comparative functional analysis of aquaporins/glyceroporins in mammals and anurans. *Mammalian Genome: Official Journal of the International Mammalian Genome Society* 2007;18:452–62. <https://doi.org/10.1007/s00335-007-9041-5>.
- [20] Calvanese L, Pellegrini-Calace M, Oliva R. *In silico* study of human aquaporin AQP11 and AQP12 channels. *Protein Science* 2013;22:455–66. <https://doi.org/10.1002/pro.2227>.
- [21] Suzuki M, Shibata Y, Ogushi Y, Okada R. Molecular Machinery for Vasotocin-Dependent Trans-epithelial Water Movement in Amphibians: Aquaporins and Evolution. *The Biological Bulletin* 2015;229:109–19. <https://doi.org/10.1086/BBLv229n1p109>.
- [22] Tong H, Hu Q, Zhu L, Dong X. Prokaryotic Aquaporins. *Cells* 2019;8:1316. <https://doi.org/10.3390/cells8111316>.
- [23] Pettersson N, Filipsson C, Becit E, Brive L, Hohmann S. Aquaporins in yeasts and filamentous fungi. *Biol Cell* 2005;97:487–500. <https://doi.org/10.1042/BC20040144>.
- [24] Kumar M, Grzelakowski M, Zilles J, Clark M, Meier W. Highly permeable polymeric membranes based on the incorporation of the functional water channel protein Aquaporin Z. *Proc Natl Acad Sci U S A* 2007;104:20719–24. <https://doi.org/10.1073/pnas.0708762104>.
- [25] Yang Z, Wu C, Tang CY. Making waves: Why do we need ultra-permeable nanofiltration membranes for water treatment? *Water Res X* 2023;19:100172. <https://doi.org/10.1016/j.wroa.2023.100172>.
- [26] Nielsen CH. Biomimetic membranes for sensor and separation applications. *Anal Bioanal Chem* 2009;395:697–718. <https://doi.org/10.1007/s00216-009-2960-0>.

- [27] Li Y, Qi S, Tian M, Widjajanti W, Wang R. Fabrication of aquaporin-based biomimetic membrane for seawater desalination. *Desalination* 2019;467:103–12. <https://doi.org/10.1016/j.desal.2019.06.005>.
- [28] Güvensoy-Morkoyun A, Veliöglu S, Göktuğ MA, Tantekin-Ersolmaz SB. Desalination Potential of Aquaporin-Inspired Functionalization of Carbon Nanotubes: Bridging Between Simulation and Experiment. *ACS Applied Materials & Interfaces* 2022;14:28174–85. <https://doi.org/10.1021/acsami.2c03700>.
- [29] Tang C, Wang Z, Petrinić I, Fane AG, Hélix-Nielsen C. Biomimetic aquaporin membranes coming of age. *Desalination* 2015;368:89–105. <https://doi.org/10.1016/j.desal.2015.04.026>.
- [30] Tang CY, Zhao Y, Wang R, Hélix-Nielsen C, Fane AG. Desalination by biomimetic aquaporin membranes: Review of status and prospects. *Desalination* 2013;308:34–40. <https://doi.org/10.1016/j.desal.2012.07.007>.
- [31] Hélix-Nielsen C. Biomimetic membranes as a technology platform: Challenges and opportunities. *Membranes* 2018;8. <https://doi.org/10.3390/membranes8030044>.
- [32] Azarafza A, Islam MA, Golpazirsorkheh Y, Efteghar I, Sadrzadeh M, Kamkar M, et al. Aquaporin-Based Biomimetic Membranes for Low Energy Water Desalination and Separation Applications. *Advanced Functional Materials* 2023;33:2213326. <https://doi.org/10.1002/adfm.202213326>.
- [33] Shannon MA, Bohn PW, Elimelech M, Georgiadis JG, Mariñas BJ, Mayes AM. Science and technology for water purification in the coming decades. *Nature* 2008;452:301–10. <https://doi.org/10.1038/nature06599>.
- [34] Space-Age Water Conservation | NASA Spinoff n.d. <https://spinoff.nasa.gov/page/space-age-water-conservation-nasa> (accessed April 27, 2024).
- [35] Atkinson S. Aquaporin's membranes play a vital role in effectively cleaning both produced and oil and gas flow-back water. *Membrane Technology* 2020;2020:5–6. [https://doi.org/10.1016/S0958-2118\(20\)30107-5](https://doi.org/10.1016/S0958-2118(20)30107-5).
- [36] Beratto-Ramos A, Dagnino-Leone J, Martínez-Oyanedel J, Aranda M, Bórquez R. Fabrication and Filtration Performance of Aquaporin Biomimetic Membranes for Water Treatment. *Separation & Purification Reviews* 2022;51:340–57. <https://doi.org/10.1080/15422119.2021.1948865>.

- [37] Grzelakowski M, Cherenet MF, Shen YX, Kumar M. A framework for accurate evaluation of the promise of aquaporin based biomimetic membranes. *Journal of Membrane Science* 2015;479:223–31. <https://doi.org/10.1016/j.memsci.2015.01.023>.
- [38] Abdelrasoul A, Doan H, Lohi A, Cheng, C.-H. Aquaporin-Based Biomimetic and Bioinspired Membranes for New Frontiers in Sustainable Water Treatment Technology: Approaches and Challenges. *Polymer Science, Series A* 2018;60:429–50. <https://doi.org/10.1134/S0965545X18040016>.
- [39] Cohen-Tanugi D, McGovern RK, Dave SH, Lienhard JH, Grossman JC. Quantifying the potential of ultra-permeable membranes for water desalination. *Energy Environ Sci* 2014;7:1134–41. <https://doi.org/10.1039/C3EE43221A>.
- [40] Fasano M, Morciano M, Bergamasco L, Chiavazzo E, Zampato M, Carminati S, et al. Deep-sea reverse osmosis desalination for energy efficient low salinity enhanced oil recovery. *Applied Energy* 2021;304:117661. <https://doi.org/10.1016/j.apenergy.2021.117661>.
- [41] Qasim M, Badrelzaman M, Darwish NN, Darwish NA, Hilal N. Reverse osmosis desalination: A state-of-the-art review. *Desalination* 2019;459:59–104. <https://doi.org/10.1016/j.desal.2019.02.008>.
- [42] Morciano M, Fasano M, Bergamasco L, Albiero A, Curzio ML, Asinari P, et al. Sustainable freshwater production using passive membrane distillation and waste heat recovery from portable generator sets. *Applied Energy* 2020;258:114086. <https://doi.org/10.1016/j.apenergy.2019.114086>.
- [43] Antonetto G, Morciano M, Alberghini M, Malgaroli G, Ciocia A, Bergamasco L, et al. Synergistic freshwater and electricity production using passive membrane distillation and waste heat recovered from camouflaged photovoltaic modules. *Journal of Cleaner Production* 2021;318:128464. <https://doi.org/10.1016/j.jclepro.2021.128464>.
- [44] Kocsis I, Sun Z, Legrand YM, Barboiu M. Artificial water channels—deconvolution of natural Aquaporins through synthetic design. *Npj Clean Water* 2018;1:1–11. <https://doi.org/10.1038/s41545-018-0013-y>.

- [45] Song W, Kumar M. Artificial water channels: toward and beyond desalination. *Current Opinion in Chemical Engineering* 2019;25:9–17. <https://doi.org/10.1016/j.coche.2019.06.007>. 516
517
- [46] Barboiu M, Le Duc Y, Gilles A, Cazade P-A, Michau M, Marie Legrand Y, et al. An artificial primitive mimic of the Gramicidin-A channel. *Nat Commun* 2014;5:4142. 518
<https://doi.org/10.1038/ncomms5142>. 519
520
- [47] Andrei IM, Chaix A, Benkhaled BT, Dupuis R, Gomri C, Petit E, et al. Selective Water Pore Recognition and Transport through Self-Assembled Alkyl-Ureido-Trianglamine Artificial Water Channels. *J Am Chem Soc* 2023;145:21213–21. <https://doi.org/10.1021/jacs.3c02815>. 521
522
523
- [48] Vincenzo MD, Tiraferri A, Musteata VE, Chisca S, Sougrat R, Huang LB, et al. Biomimetic artificial water channel membranes for enhanced desalination. *Nature Nanotechnology* 2021;16:190–6. <https://doi.org/10.1038/s41565-020-00796-x>. 524
525
526
- [49] Kruse E, Uehlein N, Kaldenhoff R. The aquaporins. *Genome Biology* 2006;7:206. 527
<https://doi.org/10.1186/gb-2006-7-2-206>. 528
- [50] Groot BL de, Grubmüller H. The dynamics and energetics of water permeation and proton exclusion in aquaporins. *Current Opinion in Structural Biology* 2005;15:176–83. 529
<https://doi.org/10.1016/j.sbi.2005.02.003>. 531
- [51] Ozu M, Alvear-Arias JJ, Fernandez M, Caviglia A, Peña-Pichicoi A, Carrillo C, et al. Aquaporin Gating: A New Twist to Unravel Permeation through Water Channels. *International Journal of Molecular Sciences* 2022;23:12317. <https://doi.org/10.3390/ijms232012317>. 532
533
534
- [52] Ozu M, Galizia L, Acuña C, Amodeo G. Aquaporins: More Than Functional Monomers in a Tetrameric Arrangement. *Cells* 2018;7:209. <https://doi.org/10.3390/cells7110209>. 535
536
- [53] Structure, Dynamics, and Function of Aquaporins n.d. <https://www.ks.uiuc.edu/Research/aquaporins/> (accessed April 28, 2024). 537
538
- [54] Froger A, Thomas D, Delamarche C, Tallur B. Prediction of functional residues in water channels and related proteins. *Protein Science* 1998;7:1458–68. <https://doi.org/10.1002/pro.5560070623>. 539
540
- [55] Fu D, Lu M. The structural basis of water permeation and proton exclusion in aquaporins (Review). *Molecular Membrane Biology* 2007. <https://doi.org/10.1080/09687680701446965>. 541
542

- [56] Wachlmayr J, Samineni L, Knyazev DG, Barta T, Speletz A, Yao C, et al. Biophysical quantification of unitary solute and solvent permeabilities to enable translation to membrane science. *Journal of Membrane Science* 2023;675:121308. <https://doi.org/10.1016/j.memsci.2022.121308>. 543
544
545
- [57] Horner A, Zocher F, Preiner J, Ollinger N, Siligan C, Akimov SA, et al. The mobility of single-file water molecules is governed by the number of H-bonds they may form with channel-lining residues. *Science Advances* 2015;1:e1400083. <https://doi.org/10.1126/sciadv.1400083>. 546
547
548
- [58] Horner A, Siligan C, Cornean A, Pohl P. Positively charged residues at the channel mouth boost single-file water flow. *Faraday Discuss* 2018;209:55–65. <https://doi.org/10.1039/C8FD00050F>. 549
550
- [59] Horner A, Pohl P. Single-file transport of water through membrane channels. *Faraday Discuss* 2018;209:9–33. <https://doi.org/10.1039/C8FD00122G>. 551
552
- [60] Gravelle S, Joly L, Detcheverry F, Ybert C, Cottin-Bizonne C, Bocquet L. Optimizing water permeability through the hourglass shape of aquaporins. *Proc Natl Acad Sci USA* 2013;110:16367–72. <https://doi.org/10.1073/pnas.1306447110>. 553
554
555
- [61] Gössweiner-Mohr N, Siligan C, Pluhackova K, Umlandt L, Koeffler S, Trajkovska N, et al. The Hidden Intricacies of Aquaporins: Remarkable Details in a Common Structural Scaffold. *Small* 2022;18:2202056. <https://doi.org/10.1002/smll.202202056>. 556
557
558
- [62] Fu D, Lisbon A, Miercke LJ, Weitzman C, Nollert P, Krucinski J, et al. Structure of a glycerol-conducting channel and the basis for its selectivity. *Science* 2000;290:481–6. <https://doi.org/10.1126/science.290.5491.481>. 559
560
561
- [63] de Groot BL, Grubmüller H. Water permeation across biological membranes: mechanism and dynamics of aquaporin-1 and GlpF. *Science* 2001;294:2353–7. <https://doi.org/10.1126/science.1066115>. 562
563
564
- [64] Gonen T, Walz T. The structure of aquaporins. *Quarterly Reviews of Biophysics* 2006;39:361–96. <https://doi.org/10.1017/S0033583506004458>. 565
566
- [65] Solenov EI, Baturina GS, Katkova LE, Zarogiannis SG. Methods to Measure Water Permeability. In: Yang B, editor. *Aquaporins*, Dordrecht: Springer Netherlands; 2017, p. 263–76. https://doi.org/10.1007/978-94-024-1057-0_18. 567
568
569

- [66] Xiong M, Li C, Wang W, Yang B. Protein Structure and Modification of Aquaporins. In: Yang B, editor. *Aquaporins*, Singapore: Springer Nature; 2023, p. 15–38. https://doi.org/10.1007/978-981-19-7415-1_2.
- [67] Cherkasov A, Muratov EN, Fourches D, Varnek A, Baskin II, Cronin M, et al. QSAR Modeling: Where Have You Been? Where Are You Going To? *J Med Chem* 2014;57:4977–5010. <https://doi.org/10.1021/jm4004285>.
- [68] Muratov EN, Bajorath J, Sheridan RP, Tetko IV, Filimonov D, Poroikov V, et al. QSAR without borders. *Chem Soc Rev* 2020;49:3525–64. <https://doi.org/10.1039/D0CS00098A>.
- [69] Emonts J, Buyel JF. An overview of descriptors to capture protein properties – Tools and perspectives in the context of QSAR modeling. *Comput Struct Biotechnol J* 2023;21:3234–47. <https://doi.org/10.1016/j.csbj.2023.05.022>.
- [70] Barley MH, Turner NJ, Goodacre R. Improved Descriptors for the Quantitative Structure–Activity Relationship Modeling of Peptides and Proteins. *J Chem Inf Model* 2018;58:234–43. <https://doi.org/10.1021/acs.jcim.7b00488>.
- [71] PROSITE: Database of protein domains, families and functional sites n.d. <https://prosite.expasy.org/> (accessed October 16, 2023).
- [72] Sigrist CJ, Castro E de, Cerutti L, others. New and continuing developments at PROSITE. *Nucleic Acids Research* 2013;41:D344–7.
- [73] Paysan-Lafosse T, Blum M, Chuguransky S, Grego T, Pinto BL, Salazar GA, et al. InterPro in 2022. *Nucleic Acids Research* 2023;51:D418–27. <https://doi.org/10.1093/nar/gkac993>.
- [74] InterPro: Classification of protein families n.d. <https://www.ebi.ac.uk/interpro/> (accessed April 26, 2024).
- [75] Berman HM, Mitsuoka K, Westbrook J, Gilliland ZF andG, Bhat TN, Weissig H, et al. The Protein Data Bank. *Nucleic Acids Research* 2000;28:235–42. <https://doi.org/10.1093/nar/28.1.235>.
- [76] Harries WE, Akhavan D, Miercke LJ, Khademi S, Stroud RM. The channel architecture of aquaporin 0 at a 2.2-Å resolution. *Proceedings of the National Academy of Sciences of the United States of America* 2004;101:14045–50. <https://doi.org/10.1073/pnas.0405274101>.

- [77] Gonen T, Cheng Y, Sliz P, Hiroaki Y, Fujiyoshi Y, Harrison SC, et al. Lipid-protein interactions in double-layered two-dimensional AQP0 crystals. *Nature* 2005;438:633–8. <https://doi.org/10.1038/nature04321>.
- [78] Sui H, Han BG, Lee JK, Walian P, Jap BK. Structural basis of water-specific transport through the AQP1 water channel. *Nature* 2001;41:872–8. <https://doi.org/10.1038/414872a>.
- [79] Zeng J, Schmitz F, Isaksson S, Glas J, Arbab O, Andersson M, et al. High-resolution structure of a fish aquaporin reveals a novel extracellular fold. *Life Science Alliance* 2022;5. <https://doi.org/10.26508/lsa.202201491>.
- [80] Kosinska Eriksson U, Fischer G, Friemann R, Enkavi G, Tajkhorshid E, Neutze R. Subangstrom resolution X-ray structure details aquaporin-water interactions. *Science* 2013;340:1346–9. <https://doi.org/10.1126/science.1234306>.
- [81] Frick A, Eriksson UK, Mattia F de, Oberg F, Hedfalk K, Neutze R, et al. X-ray structure of human aquaporin 2 and its implications for nephrogenic diabetes insipidus and trafficking. *Proceedings of the National Academy of Sciences of the United States of America* 2014;111:6305–10. <https://doi.org/10.1073/pnas.1321406111>.
- [82] Ho JD, Yeh R, Sandstrom A, Chorny I, Harries WE, Robbins RA, et al. Crystal structure of human aquaporin 4 at 1.8 Å and its mechanism of conductance. *Proceedings of the National Academy of Sciences of the United States of America* 2009;106:7437–42. <https://doi.org/10.1073/pnas.0902725106>.
- [83] Hiroaki Y, Tani K, Kamegawa A, Gyobu N, Nishikawa K, Suzuki H, et al. Implications of the aquaporin-4 structure on array formation and cell adhesion. *Journal of Molecular Biology* 2006;355:628–39. <https://doi.org/10.1016/j.jmb.2005.10.081>.
- [84] Horsefield R, Nordén K, Fellert M, Backmark A, Törnroth-Horsefield S, Scheltinga ACT van, et al. High-resolution x-ray structure of human aquaporin 5. *Proceedings of the National Academy of Sciences of the United States of America* 2008;105:13327–32. <https://doi.org/10.1073/pnas.0801466105>.

- [85] de Mare SW, Venskutonytė R, Eltschkner S, de Groot BL, Lindkvist-Petersson K. Structural basis for glycerol efflux and selectivity of human aquaporin 7. *Structure* 2020;28:215–22. <https://doi.org/10.1016/j.str.2019.11.011>.
- [86] Gotfryd K, Mósca AF, Missel JW, Truelsen SF, Wang K, Spulber M, et al. Human adipose glycerol flux is regulated by a pH gate in AQP10. *Nature Communications* 2018;9:1–11. <https://doi.org/10.1038/s41467-018-07176-z>.
- [87] Törnroth-Horsefield S, Wang Y, Hedfalk K, Johanson U, Karlsson M, Tajkhorshid E, et al. Structural mechanism of plant aquaporin gating. *Nature* 2006;439:688–94. <https://doi.org/10.1038/nature04316>.
- [88] Lee JK, Kozono D, Remis J, Kitagawa Y, Agre P, Stroud RM. Structural basis for conductance by the archaeal aquaporin AqpM at 1.68 Å. *Proceedings of the National Academy of Sciences* 2005;102:18932–7. <https://doi.org/10.1073/pnas.0509469102>.
- [89] Lee JK, Finer-Moore JS, Stroud RM. RCSB Protein Data Bank, 3NE2: *Archaeoglobus fulgidus* aquaporin n.d. <https://www.rcsb.org/structure/3ne2> (accessed October 6, 2023).
- [90] Saitoh Y, Mitani-Ueno N, Saito K, Matsuki K, Huang S, Yang L, et al. Structural basis for high selectivity of a rice silicon channel Lsi1. *Nature Communications* 2021;12:6236. <https://doi.org/10.1038/s41467-021-26535-x>.
- [91] Kirscht A, Kaptan SS, Bienert GP, Chaumont F, Nissen P, Goot BL de, et al. Crystal Structure of an Ammonia-Permeable Aquaporin. *PLoS Biology* 2016;14:e1002411. <https://doi.org/10.1371/journal.pbio.1002411>.
- [92] Savage DF, Egea PF, Robles-Colmenares Y, O’Connell 3rd JD, Stroud RM. Architecture and selectivity in aquaporins: 2.5 a X-ray structure of aquaporin Z. *PLoS Biology* 2003;1:E72. <https://doi.org/10.1371/journal.pbio.0000072>.
- [93] Liu Q, Hillerich B, Love J, NYCOMPS. RCSB Protein Data Bank, 3LLQ: Aquaporin structure from plant pathogen *Agrobacterium Tumerfaciens* n.d. <https://www.rcsb.org/structure/3llq> (accessed October 6, 2023).

- [94] Newby ZE, O'Connell Iii J, Robles-Colmenares Y, Khademi S, Miercke LJ, Stroud RM. Crystal structure of the aquaglyceroporin PfAQP from the malarial parasite *Plasmodium falciparum*. *Nature Structural & Molecular Biology* 2008;15:619–25. <https://doi.org/10.1038/nsmb.1431>. 649
650
651
- [95] Moss FJ, Mahinthichaichan P, Lodowski DT, Kowatz T, Tajkhorshid E, Engel A, et al. Aquaporin-7: A Dynamic Aquaglyceroporin With Greater Water and Glycerol Permeability Than Its Bacterial Homolog GlpF. *Front Physiol* 2020;11:728. <https://doi.org/10.3389/fphys.2020.00728>. 652
653
654
- [96] Katano T, Ito Y, Ohta K, Yasujima T, Inoue K, Yuasa H. Functional Characteristics of Aquaporin 7 as a Facilitative Glycerol Carrier. *Drug Metabolism and Pharmacokinetics* 2014;29:244–8. <https://doi.org/10.2133/dmpk.DMPK-13-RG-121>. 655
656
657
- [97] Palmgren M, Hernebring M, Eriksson S, Elbing K, Geijer C, Lasič S, et al. Quantification of the Intracellular Life Time of Water Molecules to Measure Transport Rates of Human Aquaglyceroporins. *J Membr Biol* 2017;250:629–39. <https://doi.org/10.1007/s00232-017-9988-4>. 658
659
660
- [98] Zhu F, Tajkhorshid E, Schulten K. Theory and simulation of water permeation in aquaporin-1. *Biophysical Journal* 2004;86:50–7. [https://doi.org/10.1016/S0006-3495\(04\)74082-5](https://doi.org/10.1016/S0006-3495(04)74082-5). 661
662
- [99] Pellegrini-Calace M, Maiwald T, Thornton JM. PoreWalker: A Novel Tool for the Identification and Characterization of Channels in Transmembrane Proteins from Their Three-Dimensional Structure. *PLoS Comput Biol* 2009;5:e1000440. <https://doi.org/10.1371/journal.pcbi.1000440>. 663
664
665
- [100] Kyte J, Doolittle RF. A simple method for displaying the hydropathic character of a protein. *Journal of Molecular Biology* 1982;157:105–32. [https://doi.org/10.1016/0022-2836\(82\)90515-0](https://doi.org/10.1016/0022-2836(82)90515-0). 666
667
- [101] Discovery Studio, BIOVIA, Dassault Systèmes 2022. 668
- [102] Tibshirani R. Regression Shrinkage and Selection Via the Lasso. *Journal of the Royal Statistical Society: Series B (Methodological)* 1996;58:267–88. <https://doi.org/10.1111/j.2517-6161.1996.tb02080.x>. 669
670
671
- [103] Kovalevskiy O, Mateos-Garcia J, Tunyasuvunakool K. AlphaFold two years on: Validation and impact. *Proceedings of the National Academy of Sciences* 2024;121:e2315002121. <https://doi.org/10.1073/pnas.2315002121>. 672
673
674
- [104] Jumper J, Evans R, Pritzel A, others. Highly accurate protein structure prediction with AlphaFold. *Nature* 2021;596:583–9. <https://doi.org/10.1038/s41586-021-03819-2>. 675
676

- [105] Vander Meersche Y, Diharce J, Gelly J-C, Galochkina T. Flexibility or uncertainty? A critical assessment of AlphaFold 2 pLDDT. *Structure* 2025;33:2157-2163.e2. <https://doi.org/10.1016/j.str.2025.09.001>.
- [106] Carugo O. pLDDT Values in AlphaFold2 Protein Models Are Unrelated to Globular Protein Local Flexibility. *Crystals* 2023;13:1560. <https://doi.org/10.3390/cryst13111560>.
- [107] Zeidel ML, Ambudkar SV, Smith BL, Agre P. Reconstitution of functional water channels in liposomes containing purified red cell CHIP28 protein. *Biochemistry* 1992;31:7436–40. <https://doi.org/10.1021/bi00148a002>.
- [108] Zeidel ML, Nielsen S, Smith BL, Ambudkar SV, Maunsbach AB, Agre P. Ultrastructure, pharmacologic inhibition, and transport selectivity of aquaporin CHIP in proteoliposomes. *Biochemistry* 1994;33:1606–15. <https://doi.org/10.1021/bi00172a042>.
- [109] Jensen MØ, Mouritsen OG. Single-channel water permeabilities of Escherichia coli aquaporins AqpZ and GlpF. *Biophysical Journal* 2006;90:2270–84. <https://doi.org/10.1529/biophysj.105.073965>.
- [110] Walz T, Smith BL, Zeidel ML, Engel A, Agre P. Biologically active two-dimensional crystals of aquaporin CHIP. *Journal of Biological Chemistry* 1994;269:1583–6. [https://doi.org/10.1016/S0021-9258\(17\)42062-X](https://doi.org/10.1016/S0021-9258(17)42062-X).
- [111] Coury LA, Mathai JC, Prasad GV, Brodsky JL, Agre P, Zeidel ML. Reconstitution of water channel function of aquaporins 1 and 2 by expression in yeast secretory vesicles. *Am J Physiol* 1998;274:F34-42. <https://doi.org/10.1152/ajprenal.1998.274.1.F34>.
- [112] Pohl P, Saparov SM, Borgnia MJ, Agre P. Highly selective water channel activity measured by voltage clamp: analysis of planar lipid bilayers reconstituted with purified AqpZ. *Proceedings of the National Academy of Sciences* 2001;98:9624–9. <https://doi.org/10.1073/pnas.161299398>.
- [113] Jensen MØ, Park S, Tajkhorshid E, Schulten K. Energetics of glycerol conduction through aquaglyceroporin GlpF. *Proc Natl Acad Sci U S A* 2002;99:6731–6. <https://doi.org/10.1073/pnas.102649299>.

- [114] Boytsov D, Hanneschlaeger C, Horner A, Siligan C, Pohl P. Micropipette Aspiration-Based Assessment of Single Channel Water Permeability. *Biotechnol J* 2020;15:e1900450. <https://doi.org/10.1002/biot.201900450>.
- [115] Yue K, Jiang J, Zhang P, Kai L. Functional Analysis of Aquaporin Water Permeability Using an *Escherichia coli*-Based Cell-Free Protein Synthesis System. *Front Bioeng Biotechnol* 2020;8. <https://doi.org/10.3389/fbioe.2020.01000>.
- [116] Araya-Secchi R, Garate JA, Holmes DS, Perez-Acle T. Molecular dynamics study of the archaeal aquaporin AqpM. *BMC Genomics* 2011;12 Suppl 4:S8. <https://doi.org/10.1186/1471-2164-12-S4-S8>.
- [117] Hashido M, Ikeguchi M, Kidera A. Comparative simulations of aquaporin family: AQP1, AQPZ, AQP0 and GlpF. *FEBS Letters* 2005;579:5549–52. <https://doi.org/10.1016/j.febslet.2005.09.018>.
- [118] Hashido M, Kidera A, Ikeguchi M. Water transport in aquaporins: osmotic permeability matrix analysis of molecular dynamics simulations. *Biophysical Journal* 2007;93:373–85. <https://doi.org/10.1529/biophysj.106.101170>.
- [119] Binesh AR, Kamali R. Molecular dynamics insights into human aquaporin 2 water channel. *Biophysical Chemistry* 2015;207:107–13. <https://doi.org/10.1016/j.bpc.2015.10.002>.
- [120] Alberga D, Nicolotti O, Lattanzi G, Nicchia GP, Frigeri A, Pisani F, et al. A new gating site in human aquaporin-4: Insights from molecular dynamics simulations. *Biochimica et Biophysica Acta (BBA)-Biomembranes* 2014;1838:3052–60. <https://doi.org/10.1016/j.bbamem.2014.08.015>.
- [121] Garate J-A, English NJ, MacElroy JMD. Human aquaporin 4 gating dynamics in dc and ac electric fields: A molecular dynamics study. *The Journal of Chemical Physics* 2011;134:055110. <https://doi.org/10.1063/1.3529428>.
- [122] Jung JS, Bhat RV, Preston GM, Guggino WB, Baraban JM, Agre P. Molecular characterization of an aquaporin cDNA from brain: candidate osmoreceptor and regulator of water balance. *Proc Natl Acad Sci U S A* 1994;91:13052–6. <https://doi.org/10.1073/pnas.91.26.13052>.
- [123] Alishahi M, Kamali R. Forced diffusion of water molecules through aquaporin-5 biomembrane; a molecular dynamics study. *Biophysics and Physicobiology* 2018;15:255–62. https://doi.org/10.2142/biophysico.15.0_255.

- [124] Galano-Frutos JJ, Sancho J. Energy, water, and protein folding: A molecular dynamics-based quantitative inventory of molecular interactions and forces that make proteins stable. *Protein Science* 2024;33:e4905. <https://doi.org/10.1002/pro.4905>. 731
732
733
- [125] Galano-Frutos JJ, Nerín-Fonz F, Sancho J. Calculation of Protein Folding Thermodynamics Using Molecular Dynamics Simulations. *J Chem Inf Model* 2023;63:7791–806. <https://doi.org/10.1021/acs.jcim.3c01107>. 734
735
736
- [126] Saboe PO, Rapisarda C, Kaptan S, Hsiao Y-S, Summers SR, De Zorzi R, et al. Role of Pore-Lining Residues in Defining the Rate of Water Conduction by Aquaporin-0. *Biophysical Journal* 2017;112:953–65. <https://doi.org/10.1016/j.bpj.2017.01.026>. 737
738
739
- [127] Kozono D, Yasui M, King LS, Agre P. Aquaporin water channels: atomic structure molecular dynamics meet clinical medicine. *J Clin Invest* 2002;109:1395–9. <https://doi.org/10.1172/JCI15851>. 740
741
742
- [128] Verkman AS, Mitra AK. Structure and function of aquaporin water channels. *Am J Physiol Renal Physiol* 2000;278:F13-28. <https://doi.org/10.1152/ajprenal.2000.278.1.F13>. 743
744
- [129] Frick A, Järvå M, Törnroth-Horsefield S. Structural basis for pH gating of plant aquaporins. *FEBS Letters* 2013;587:989–93. <https://doi.org/10.1016/j.febslet.2013.02.038>. 745
746
- [130] Tournaire-Roux C, Sutka M, Javot H, Gout E, Gerbeau P, Luu D-T, et al. Cytosolic pH regulates root water transport during anoxic stress through gating of aquaporins. *Nature* 2003;425:393–7. <https://doi.org/10.1038/nature01853>. 747
748
749
- [131] Yaneff A, Sigaut L, Marquez M, Alleva K, Pietrasanta LI, Amodeo G. Heteromerization of PIP aquaporins affects their intrinsic permeability. *Proceedings of the National Academy of Sciences* 2014;111:231–6. <https://doi.org/10.1073/pnas.1316537111>. 750
751
752
- [132] Yaneff A, Sigaut L, Gómez N, Aliaga Fandiño C, Alleva K, Pietrasanta LI, et al. Loop B serine of a plasma membrane aquaporin type PIP2 but not PIP1 plays a key role in pH sensing. *Biochimica et Biophysica Acta (BBA) - Biomembranes* 2016;1858:2778–87. <https://doi.org/10.1016/j.bbamem.2016.08.002>. 753
754
755
756
757

Supplementary Information

for

Pore-level Quantitative Structure-Activity Relationship (QSAR) for Water Permeation Rate in Aquaporins

Juan José Galano-Frutos^{1,a,†,}, Luca Bergamasco^{2,a,*}, Paolo Vigo², Matteo Morciano²,
Matteo Fasano², Davide Pirolli¹, Eliodoro Chiavazzo² and Maria Cristina de Rosa¹*

¹ *Istituto di Scienze e Tecnologie Chimiche “Giulio Natta” (SCITEC) - National Research Council (CNR), Via
Largo Francesco Vito 1, 00168 Rome, Italy*

² *Department of Energy, Politecnico di Torino, C.so Duca degli Abruzzi 24, 10129 Turin, Italy*

[†] *Present address: Certest Biotec S.L., 50840 San Mateo de Gallego, Zaragoza, Spain*

^a *These authors contributed equally to this work*

^{*} *Corresponding author(s): J.J.G.-F. jjgalano@certest.es; L.B. luca.bergamasco@polito.it*

TABLE OF CONTENT

Best Practices and Pore-level QSAR Modeling.....	4
Pairwise Comparison (Structure and Sequence).....	10
Pore Shape Analysis	12
Pore Composition Analysis.....	14
SUPPLEMENTARY TABLES	16
Table S1. Experimental or computed water permeation rate(s) reported for AQ(G)Ps.....	16
Table S2. Corrected single-channel water permeation rates for AQ(G)Ps. ^a	22
Table S3. Pore characteristics and additional data extracted from PoreWalker output.	23
Table S4. Sequences of the NPA and the selectivity filter (SF) motifs of selected AQ(G)Ps. The symbols highlight the difference or identity across the sequences of the NPA and the SF motifs.....	29
Table S5. Resolution, experimental conditions and other relevant information on crystallization of AQ(G)Ps in the modeled datasets. ^a	31
Table S6. Computed values of the PDs retained in Model 3.2b, along with predicted <i>pfcorr</i> values and residuals for the four AQPs used for external validation.....	32
Table S7. Composition (in %) per amino acid (AA) and per amino acid type for the AQ(G)Ps' pore lining compared to whole protein.	33
SUPPLEMENTARY FIGURES	36
Figure S1. Pore properties profiles and geometrical shape for all the AQ(G)Ps listed in Table 1 of the main text, except for <i>E. coli</i> AqpZ included in the main article.....	40
Figure S2. Structural and sequence comparisons of AQ(G)Ps.	41
Figure S3. Hierarchical clustering based on the pairwise TM-score of AQ(G)Ps.	42

Figure S4. Comparative depiction of the per-amino-acid type composition (in %) both in the whole protein and the pore lining across the AQ(G)Ps investigated.	43
Figure S5. Final LASSO coefficients and <i>y</i>-scramblings analyses for the best-performing QSAR models.	44
Figure S6. Structure comparison of AQPs on pore gating molecular events.	45
SUPPLEMENTARY REFERENCES	46

Best Practices and Pore-level QSAR Modeling

Multicollinearity analysis. Auto-correlation matrixes were computed to identify multicollinearity among descriptors. In addition, the variance inflation factors (VIF)¹ and the condition number (CN)²—calculated for the best QSAR models presented in the main text (Table 3)—were used as complementary indicators of multicollinearity between variables.

LASSO iterative regularization [3]. LASSO was applied to the OLS-MLR models to select optimal combinations of PDs. The associated alpha³ parameter (lambda in Ref. [3]) was set in the range 0.1–1.0 (moderate penalty) to discourage highly correlated predictors. The maximum number of iterations was set to 1,000,000, and convergence was achieved in all cases.

Characteristic Features of AQ(G)Ps: Similarities and Differences

Basic Structure. Aquaporins are tetramers formed by four monomer channels, each constituted by six transmembrane and two half-spanning helices interconnected through

¹ The Variance Inflation Factor (VIF) [1] measures the extent of multi-collinearity in a regression model. A VIF value of 1 indicates no correlation between the independent variable and others. Values between 1 and 5 suggest moderate multicollinearity, while values above 5 indicate significant multicollinearity that could affect the stability of coefficient estimates. A VIF greater than 10 is often considered problematic, as it implies substantial inflation of the variance of the estimated coefficients, leading to unreliable results.

² The condition number (CN) [2] is a crucial metric that assesses the sensitivity of the regression coefficients to perturbations in the data. Generally, a condition number less than 10 indicates a well-conditioned model, suggesting stable and reliable coefficient estimates with minimal numerical errors. Values between 10 and 30 are often associated with moderate multicollinearity, where the results may still be usable but should be approached with caution. Condition numbers between 30 and 100 indicate significant multi-collinearity, raising concerns about the stability of the coefficient estimates. A condition number greater than 100 signals a poorly conditioned model, which can lead to high sensitivity to input changes, resulting in considerable numerical instability and unreliable outputs.

³ The alpha parameter in the LASSO method controls the strength of the regularization applied to the regression model. A small alpha value (e.g., <0.1) results in minimal regularization, allowing for more complex models that may overfit the data. Conversely, a larger alpha value (e.g., >1.0) increases the penalty on the coefficients, particularly affecting variables with significant multicollinearity. This leads to simpler models with potentially better generalization, but at the cost of possibly excluding important predictors and risking underfitting the data.

five loops [4–6]. The inner terminals of the two half helices host the amino acid sequences constituting the NPA motifs, which face each other in the middle of the pore (Fig. 1 of the main document). This motif typically involves asparagine, proline and alanine (Asn, Pro and Ala) residues, which are highly conserved in aquaporins [5–24] (see the conservation analysis addressed below). In this region, proton exclusion is accomplished with a reorientation of the water molecules, which favors their passage [4, 7, 25, 26].

Each monomer presents a second-stage filtering feature in its channel that is located closer to the extracellular border [5, 25] and works as a constriction region. This feature is generally referred to as selectivity filter (SF) or ar/R (aromatic/arginine) region, since it always comprises at least one aromatic residue and one Arg. On the outside of the pore, helices are hydrophobic, while on the inside they are mainly hydrophilic [27]. Each monomer is functionally independent with its own pore, and when assembled together, the four monomers form a pore in the middle (Fig. 1a of the main text). No water permeation has been observed in natural AQ(G)Ps through this central pore, so that the flux takes place only through the four lateral pores of the monomer units [28]. While the orthodox AQPs' pore has been shown to have approximately 1-3 Å minimum diameter [26], AQGs exhibit a constriction pore passage which is approximately 1 Å wider, which allows them to accomplish glycerol diffusion [27]. In the following sub-sections, we will present a detailed analysis of the two main features described above (see Table S4), along with an examination of the pore diameter and geometric characteristics across the selected set of AQ(G)Ps. In addition, we include a systematic analysis where we conducted structure- and sequence-based comparisons, to highlight the similarities and differences exhibited by these fundamental filtering molecules (see Fig. S2 and Fig. S3).

NPA Motif. The AQ(G)P family features two highly conserved asparagine-proline-alanine (NPA) motifs that are absent in other protein channels, like gramicidin A [7]. These two motifs, located in the narrow central segment of the channel are essential for water

permeation and selectivity. Proton exclusion in AQ(G)Ps, which is essential to maintain the electrochemical gradient across cellular and subcellular membranes, has been explained through different perspectives, including electrostatic repulsion [25, 29–31], configurational barriers [7], desolvation penalties [32] and disruption of the highly constrained water structure at the SF [33]. However, the evidence suggests that several or all these factors occur concurrently in the process. At the molecular level, a reorientation of the water molecules inside the pore passage takes place thanks to the presence of two asparagine residues facing each other in the NPA motif, which create H-bonds with the water molecule in transit, substituting some of the water-water H-bonds [25, 30]. The hydrogen bonds with the two Asn residues, instead, facilitate water diffusion through the pore [18, 26]. This reorientation allows their continuous flux so that, when one molecule moves through the channel, the next one is readily available to follow the same path [13, 25, 26, 30]. On the other hand, water molecules in the SF region exhibit highly correlated motions among themselves—dictated by protein-water H-bond interactions—while their connectivity to water molecules outside the SF becomes weaker or more discontinuous [33]. Moreover, a slightly different mechanism has been suggested in some aquaporins. For instance, in hAQP4, the two asparagines (Asn97 and Asn213) separately form H-bonds with two different water molecules, while in most other AQ(G)Ps only one water molecule is involved at a time [20]. This arrangement has also been observed in the crystal structures of hAQP5 [19] and SoPIP2;1 [20]. In aquaporins 0, the Asn184 donate a hydrogen bond to a tyrosine, Tyr23, which in turn donates it to the water molecule [34, 35]. In this regard, the low water permeation observed in these AQPs (see Table S1) could be associated with the presence of this Tyr23, which is not present in other aquaporins.

In addition to the key role previously described, the NPA region can also function as a selectivity filter. When the two NPA motifs approach each other, a constriction forms, although the narrowest point most often occurs at the ar/R region.

Little sequence variation is found in the NPA motif through the whole family of aquaporins (Table S4). This occurs, for instance, in human aquaglyceroporin 7 (hAQP7), which allows glycerol permeation through cell membranes [36]. Human AQP7 exhibits uncommon substitutions in its NPA motifs while both asparagine residues are conserved. This results in the formation of distinctive triads: NAA (Asn94, Ala95, and Ala96) and NPS (Asn226, Pro227, and Ser228, see Table S4) [36]. Another case pertains to the aquaglyceroporin found in the malarial parasite *Plasmodium falciparum* (pAqgp), a protein of great significance in the life cycle of the parasite [37]. In pAqgp, both NPA regions undergo substitutions, although the two asparagines remain also conserved: NLA (Asn-Leu-Ala) and NPS (Asn-Pro-Ser) triads (Table S4). These modifications have been suggested to be crucial in maintaining the proper alignment of the asparagine residues at the selectivity filter [37].

Selectivity Filter. Aquaporins exhibit an hourglass structure, where the narrowest part of their pore is formed by some conserved amino acids—usually in the number of four—that facilitate the passage of water [26, 38] in single file [9]. The composition of this region, known as selectivity filter (SF) or aromatic/arginine (ar/R) motif [5, 39], affects the dimension and polarity of the pore, ultimately influencing its solute selectivity and permeation rate [13, 14, 23, 40]. SF contains at least one arginine and one aromatic residue, although the specific composition may vary among different AQ(G)Ps (see Table S4).

In orthodox aquaporins, there is also a highly conserved His residue, which normally faces the positively charged Arg residue. This Arg provides two hydrogen bond donor sites to which the His may bind, constricting thus the pore passage [41]. The fact that this His appears replaced in AQGPs by a small Gly, preventing the formation of the key H-bond interactions mentioned, suggests an important role for the former in the solute selectivity of these proteins [26]. Krenc and colleagues [41], working with the rat

aquaporin 1, demonstrated the importance of this His through a mutational study in the position.

Greater sequence variability is evident in the SF motif compared to the NPA sequences among the AQ(G)Ps listed in Table S4. In bAQP1, for instance, the SF is formed by a hydrophobic corner (Phe58) and a hydrophilic face (His182, Arg197 and Cys191) on the opposite side [12]. The same residues are found in hAQP1 forming an almost identical SF: Phe56, His180, Arg195 and Cys189 [23]. This SF sequence is also carried by the aquaporin 1 of other organisms (e.g., *Anabas testudineus*: aAqp1), as well as by human aquaporins 2 and 5 (hAQP2, hAQP5). This set of AQPs is indicated with the symbol \ominus in Table S4.

Bovine and ovine aquaporins 0 (bAQP0, oAQP0), as well as the human and rat aquaporins 4 (hAQP4, rAQP4, with symbol Δ in Table S4), present the same residues quartet in their SF motif, namely Phe, His, Arg and Ala. Three of these residues (Phe, His and Arg) match those found in the SF of the previous set of aquaporins (\ominus), while the Cys is substituted by an Ala residue. In aquaporins 0, this change enables the formation of a secondary constriction region, resulting in reduced water permeation [42, 43]. In aquaporins 4, the His is thought to play a determinant role in preventing glycerol passage [20, 44].

Another subgroup of AQPs sharing the same residues in their SF motif, namely Phe, His, Arg and Thr (with symbol \square in Table S4), includes the spinach plasma membrane aquaporin (SoPIP2;1) [45], the *E. coli* and *Agrobacterium fabrum* aquaporins Z (eAqpZ [13], aAqpZ2 [46]), and the *Arabidopsis thaliana* aquaporin AtPIP2;4 [47]. In this group, the distinctive element is the Thr residue in the fourth amino acid position. In the bacterial (*E. coli*) eAqpZ, for instance, the Arg residue (Arg189) has been suggested to be crucial, as it shows two diverse conformations that result in significant differences in water permeability [21]. In one of these conformations, Arg189 forms a hydrogen bond with Thr183, which is believed to prevent the passage of water [21]. Thus, eAqpZ can exhibit structures that are either permeable or impermeable to water.

Other sequences in the SF region show a Gly residue in the second position, with a variety of other amino acids in the first and fourth positions. This is the case, for instance, of the human aquaporins 7 (hAQP7) [36] and 10 (hAQP10) [48], as well as the AQGP from the malarial parasite *Plasmodium falciparum* (pAqgp) [37] and the *E. coli* glycerol-conducting channel (eGlpF) [12].

Ile or Ser residues can also accompany Arg in the central positions of the SF region (see mAqpM and aAqpM in Table S4). Archaeal (*Methanothermobacter marburgensis*) aquaporin (mAqpM) is particularly interesting because it may exhibit multi-functional transport features. In this aquaporin, the His residue, highly conserved among water-selective AQPs, is replaced by an isoleucine residue at position 187 (Phe62, Ile187, Arg202 and Ser196). This substitution, which creates in mAqpM a wider and more hydrophobic SF than that observed in aquaporins 1, is believed to be an adaptation for the conductance of larger and less polar permeants than water, e.g., H₂S and CO₂, in addition to the water transport [15]. At the same time, the presence of Ile187—which together with Phe62 forms the hydrophobic part of the mAqpM's constriction region—creates a pore narrower than that of the *E. coli* glycerol-conducting channel, eGlpF, suggesting that mAqpM may be not suited to conduct glycerol [15].

A particular conformation of the SF has been identified in the ammonia-permeable *Arabidopsis thaliana* TIP2;1 [49] (His63, Ile185, Arg200 and Gly194), which is also permeable to water [50]. Here, the conserved His in position 2 is replaced by a more hydrophobic Ile185 increasing pore diameter. The most interesting feature, however, is the behavior of Arg200, whose sidechain is pushed to the side of the pore by His131, which acts as a fifth element of the SF motif. Besides, Arg200 is H-bound to His63, conserved across all tonoplast intrinsic proteins (TIPs), which replaces the aromatic residue (Phe or Trp) mostly present in the other AQPs. The presence of both His63 and Arg200, along with the referred SF's fifth residue, His131, are a characteristic element of aquaammoniaporins [50].

In summary, three residues—Phe, His, and Arg—are conserved across the majority of AQ(G)Ps analyzed in this study. Notably, Arg is conserved across all AQ(G)Ps. While His is highly conserved among all orthodox AQPs [12, 16, 17, 20, 21, 46, 50], this hydrophilic residue is replaced by a Gly in AQGPs [9, 36, 37, 48], leading to increased hydrophobicity and pore size.

Pairwise Comparison (Structure and Sequence)

Systematic structural similarity (Template Modeling, TM-score) and sequence identity (SI) pairwise analyses have been carried out for the AQ(G)Ps studied in this work. TM-score is a length-independent metric for assessing the topological similarity of two protein structures. It ranges between 0 and 1, where 1 indicates a perfect match between two structures, values below 0.17 correspond to randomly chosen unrelated proteins whereas structures with a score higher than 0.7 assume generally the same fold in SCOP/CATH [51, 52]. Such length independency has prompted the recommendation of this metric over the more commonly used RMSD metric for global comparative structural analyses [51].

The pairwise structural comparison between different proteins was carried out using the Pairwise Structure Alignment tool, available at the RCSB PDB website [53]. The selected protein chains are superposed based on the position of the C-alpha atoms of the backbone and on the location of secondary structural elements. Here, we selected the initial chain of the tetrameric AQ(G)Ps' structures for the calculations. The tool provides several alignment methods, both rigid and flexible. Here we adopt a rigid body alignment, which is suitable for overall structural comparison of proteins which have closely related 3D shapes. Particularly, we adopt the FATCAT algorithm [54, 55], which allows for flexible structure comparison but can be modified to a rigid structure comparison considering only alignments with matching sequence order. The method allows to calculate the TM-score [52] and the percentages of sequence identity per protein pair, among other features.

Results of the pairwise analyses carried out are shown in Fig. S2. The pairwise TM-scores depicted on the 2D map (Fig. S2a: > 0.75 for all pairs) confirm the high degree of structural similarity among all the AQ(G)Ps, regardless the live kingdom or the class or sub-class they belong to. TM-score average per aquaporin (computed across all structures, as shown in Fig. S2b) were calculated. The averages consistently surpass the value of 0.8, with the exception of *Komagataella pastoris* aquaporin 1 (0.77), that is the only fungal AQP and the most structurally distinct protein within the analyzed AQ(G)Ps set. This distinctness is also evident from the pairwise TM-score-based clustering carried out and shown in Fig. S3.

Despite the high global structural similarity among all types of AQ(G)Ps (Fig. S2b), the specific structural features exhibited by the AQ(G)Ps allow them to be grouped by the kingdom of life (e.g., animals, plants, protista, fungi, monera) or by aquaporin type (AQPs or AQGPs; see Table 1 of the main text), as shown in Fig. S3. Indeed, AQPs pairs showing the highest pairwise TM-score (> 0.95) are the *Archaeoglobus fulgidus* probable aquaporin M (aAqpM) and the *Methanothermobacter marburgensis* aquaporin M (mAqpM), with a TM-score of 0.99 (71 % SI, Fig. S2c), the *Agrobacterium fabrum* aquaporin Z2 (aAqpZ2) and the *Escherichia coli* aquaporin Z (eAqpZ), with a TM-score of 0.97 (74 % SI), the hAQP1 and the bAQP1, with a TM-score of 0.96 (89 % SI), the bAQP0 and oAQP0, with a TM-score of 0.96 (98 % SI). Consistent with this, the human aquaglyceroporins hAQP7 and hAQP10 are grouped with the other two AQGPs in the set, namely pAqgp (*Plasmodium falciparum*) and eGlpF (*E. coli*), despite belonging to different kingdoms of life. All against all, mammalian AQPs shows the highest pairwise TM-score averages (Fig. S2b), namely oAQP0 (0.856), hAQP4 (0.854), rAQP4 (0.853), and bAQP0 (0.853).

At the sequence level, the highest pairwise SI averages (calculated over all the AQ(G)Ps) are exhibited by the orthodox AQPs from animals, namely hAQP1 (0.415), hAQP5 (0.411), oAQP0 (0.41), bAQP0 (0.41), hAQP4 (0.41), rAQP4 (0.41), bAQP1 (0.408), hAQP2 (0.405) and aAqp1 (0.405) (Fig. S2d).

Pore Shape Analysis

Pore diameter is perhaps the most comprehensive physical parameter to describe the size and shape of an aquaporin's pore. The PoreWalker tool [56] facilitates the calculation of pore diameter profiles and other properties, such as pore regularity. Additionally, it provides detailed representations of longitudinal cuts of the pores, along with the list of amino acids that make up the pore lining. Fig. 4a and left top panels in Fig. S1 depict the pore diameter profile for the 22 AQ(G)Ps analyzed in this work. Table S3 contains detailed information including the minimum diameter exhibited by the AQ(G)Ps' pore. Calculated pore diameters by PoreWalker tool [56] range from 1.4 to 26.5 Å along the entire longitudinal axis among all the AQ(G)Ps listed in Table 1 of the main text. Diameter profiles indicate that both the cytoplasmic and extracellular pore vestibules have, in general, a conical shape that extends to the single-file region (constriction site) located at the center of the membrane (Fig. 4b, Fig. 4f and Figure S1). This hourglass shape, however, varies from aquaporin to aquaporin, being highly regular in bovine and ovine aquaporins-0 (bAQP0 81% and oAQP0 75% regularity along the pore, Table S3), aquaporins-1 (66-85%), human aquaporin-2 (70%), and human aquaporin-4 (65%), whereas it is less regular in the rest of AQ(G)Ps, namely: aquaporins from plants (39-58%), bacteria (30-64%), and aquaglyceroporins (41-61%, Table S3). Occasionally, the loss of regularity in the pore come together with the loss of the conical shape in one of the two halves, leading to a funnel-shaped pore. This clearly occurs with the two plant AQPs from the highly conserved subfamily known as PIPs, SoPIP2;1 and AtPIP2;4, as well as the aquaglyceroporin hAQP10 (Table S3 and Fig. S1).

PIP aquaporins have been extensively studied and shown to exhibit well-conserved auto-regulatory molecular-level mechanisms known as 'pore gating' (closure mediated by conformational change of the cytoplasmic loop D, dependent of pH, post-translational modification or calcium-binding) [57], allowing them to adjust membrane water permeation under diverse conditions [45, 58–62]. Indeed, the selected crystal structure of SoPIP2;1 (PDB ID 1Z98 [45]) has been shown to be a closed (pore-gated)

conformation [45], which is also the case of AtPIP2;4 (verified by structure comparative analysis with SoPIP2;1, see Fig. S6). Likewise, a pH-dependent pore gating mechanism has been identified in the human aquaglyceroporin hAQP10 [48], wherein His80 has been suggested to be the key residue (pH-sensor). The crystal structure of hAQP10 here analyzed (PDB ID 6F7H [48]) exhibits the closed (pore-gated) conformation (Fig. S6). Taking all this into account and examining the diameter profiles calculated by PoreWalker [56] for these AQPs, it seems that the apparent pore deformation from a classical hourglass (into a funnel-like shape), as predicted for SoPIP2;1, AtPIP2;4 and hAQP10, is mainly due to the pore closure at the cytosolic interface (Fig. S6). This regulatory mechanism seems to be less conserved in animal orthodox AQPs. Nonetheless, evidence suggesting the presence of other regulatory mechanisms, such as mechanosensitivity [63] and voltage-gating [64–66] have also been described. A recent literature review on the pore gating phenomena in AQPs is available in Ref. [57].

Water-selective AQPs typically exhibit a minimum pore diameter slightly smaller than that of a water molecule (~ 2.8 Å), while AQGs have larger diameters [21] (Table S3). In most AQ(G)Ps, the constriction site (the minimum diameter) of the pore is located at or very close to the SF motif (see Table S3, Fig. 4a and Fig. S1). In contrast, *Anabas testudineus* aquaporin-1 (aAqp1) and *Arabidopsis thaliana* TIP2;1 aquaporin (AtTIP2;1) exhibit the minimum diameter near the NPA motifs. In hAQP10 and AtPIP2;4 the minimum diameter is located near the cytoplasmic border of the pore (Table S3), consistent with the occurrence of a pore closed (pore gating)—as described above (Fig. S6). Among the water-selective AQPs, the aquaporins-0 (bAQP0 and oAQP0) and the human aquaporin-5 (hAQP5) exhibit the smallest diameters, ranging from 1.4 to 1.7 Å. This correlates well, particularly for aquaporins-0, with their p_f values, which are the lowest among all AQ(G)Ps (Table S1). However, as previously reported [67], and as further confirmed here by cross-referencing the data in Table S3 with those in Tables S1 and S2, the minimum pore diameter for the AQ(G)Ps analyzed does not follow the same hierarchical order as the experimental permeation rates. Specifically, the relative

minimum pore diameter order is: oAQP0 < bAQP0 ~ hAQP5 < eAqpZ < kAqp1 ~ aAqpM ~ aAqpZ2 < AtPIP2;4 ≈ SoPIP2;1 ≈ hAQP2 < rAQP4 < bAQP1 < mAqpM ≈ AtTIP2;1 < hAQP4 ≈ aAqp1 < eGlpF < pAqgp < hAQP1 ≈ hAQP7 << OsNIP2;1 << hAQP10 (Table S3). In contrast, the relative p_f order for the AQ(G)Ps that have been experimentally measured (average or individual values, as reported in Table S1 and showed in Fig. 2 of the main text) is: bAQP0 ≈ oAQP0 < mAqpM < eGlpF < bAQP1 < hAQP1 < eAqpZ < hAQP2 < hAQP4 << rAQP4. Likewise, for the AQ(G)Ps with corrected water permeabilities reported (p_f^{corr} , Table S2 and Fig. 2 of the main text) the relative order differs, namely: oAQP0 < sAqp < rAQP8 < hAQP2 < hAQP1 < eAqpZ ≈ rAQP4 < mAQP11 < hAQP4 < bAQP1 < RsAqpZ < eGlpF.

Pore Composition Analysis

Although specificities of the NPA and the SF motifs of AQ(G)Ps have been, in general, described, a comprehensive amino acid composition analysis of the AQ(G)Ps' pore lining at the widest available 3D structural level seems to be missing. Here, using the pore lining amino acid composition provided by PoreWalker [56] (**Supplementary Files**), we extracted the per amino acid and per amino acid type statistics (i.e., non-polar, polar uncharged, polar positively charged, and polar negatively charged residues in the pore lining) across all the AQ(G)Ps studied, and compared them with the amino acidic composition for the whole protein (Table S7 and Fig. S4).

Composition averages per amino acid type for all investigated proteins indicate that the percentages of non-polar (i.e. Gly, Ala, Val, Ile, Leu, Met, Pro, Phe, Trp) and negatively charged (Asp, Glu) amino acids are reduced by 3.4% (p-value=0.0019) and 1.4% (p-value=0.0008), respectively) in the pore lining compared to the whole protein (Fig. S4). Conversely, polar uncharged (Ser, Thr, Cys, Tyr, Asn, Gln) and positively charged (Arg, Lys, His) residues are prevalent by 2.2% (p-value=0.0068) and 2.6% (p-value=0.0003), respectively) in the pore lining. The majority of the AQ(G)Ps here

analyzed follows this general pattern individually (see Table S7). Only hAQP7, one out of the four AQGPs in the group, presents a totally opposed profile, namely higher percentages of non-polar and negatively charged amino acids while lower percentages of polar uncharged and positively charged residues in the pore lining. hAQP10—another AQGP—, and OsNIP2;1—a silicon influx transporter in the *Oryza sativa japonica* plant—, do not either fully meet the general composition picture presented by the rest of AQ(G)Ps.

Focusing solely on the pore lining residues, orthodox AQPs from the animal kingdom generally exhibit a higher content of polar residues (charged and uncharged, >38-40%, Table S7) compared to AQPs from other kingdoms, and to hAQP7 (34.4%) and hAQP10 (30.3%), the only two mammalian AQGPs in the set. The amino acid contents of these two AQGPs more closely match those of non-animal AQPs (Table S7). The higher total content of polar residues in orthodox AQPs from animals relates to the higher content of polar uncharged residues (23.3-33.3% vs. 17.0-29.2% in the remaining AQ(G)Ps) and positively charged residues (10.0-18.0% vs. 4.8-12.9%). The content of negatively charged residues is similar in both subgroups (2.1-6.7% vs. 2.0-7.5%). All in all, the current composition analysis on the reduced sample of AQ(G)Ps here studied reveals clear differences in amino acid type composition within the pore lining of animal AQPs compared to AQGPs. Such differences are not as evident in the rest of AQPs or AQGPs from the other kingdoms. Additionally, the analysis shows that only the AQGPs (hAQP7, hAQP10, pAqgp and eGlpF) have a pore lining composition where the content of non-polar amino acids is similar to or higher than that in the whole protein (Table S7), which could be related with their different selectivity and permeability (Table S1) compared to orthodox AQPs.

SUPPLEMENTARY TABLES

Table S1. Experimental or computed water permeation rate(s) reported for AQ(G)Ps.

AQ(G)P ^a (PDB ID)	Experimental Osmotic Permeability, p_f ^b ($\times 10^{-14} \text{ cm}^3 \cdot \text{s}^{-1}$)	Reference	Comments ^c	Computed Osmotic Permeability, p_f ^b ($\times 10^{-14} \text{ cm}^3 \cdot \text{s}^{-1}$)	Reference	Comments ^c
	<0.4	[68]	PSA: proteoliposomes prepared by reverse-phase evaporation, by adding phosphatidylcholine (PC, 400 mg), phosphatidylinositol (PI, 40 mg), and cholesterol (240 mg), (moles of PC:PI:cholesterol = 11:1:11); Buffer: EDTA-phosphate (pH 7.4); Yield of bAqp0 in proteoliposomes: 33%; Temperature of measurement (T): not specified (NS).	0.2±0.2	[67]	Measurements from equilibrium MDS of the protein in a lipid bilayer (5 ns x 2 replicas, NPT); Starting structure PDB: 1YMG; FFs: Charmm22+CMAP (protein), Charmm27 (lipids); WM: Tip3p.
bAQP0 (1YMG)	0.028	[69]	OSA: measurements performed in <i>Xenopus laevis</i> oocytes injected with cRNAs coding for the protein; Buffer: 96 mM NaCl, 2 mM KCl, 1 mM MgCl ₂ , 1.8 mM CaCl ₂ , 5 mM HEPES (pH 7.6); T: NS.			
	0.015	[70]	OSA: measurements performed in <i>Xenopus laevis</i> oocytes injected with cRNAs coding for the protein; Buffer: 96 mM NaCl, 2 mM KCl, 1.8 mM CaCl ₂ , 1 mM MgCl ₂ and 5 mM HEPES (pH 7.4) plus supplements (2.5 mM sodium pyruvate, 10 µg/ml aminobenzylpenicillin, 10 µg/ml streptomycin); T: 10°C.			
Ave±SEM[†]: <0.15±0.13						
oAQP0 (2B6O)	0.2±0.05	[71]	PSA: proteoliposomes reconstituted by dialysis by mixing purified oAqp1 (0.5 mg/mL) with the lipids PC, PS (phosphoserine) with cholesterol (1:4:5)	0.2±0.2	[71]	Measurements from equilibrium MDS of the protein in a POPC lipid bilayer (500 ns, NPT, 305 K, 1 atm); Starting structure PDB: 2B6O; FFs: Charmm36 (protein &

			solubilized in OG at a lipid-protein ratio of 2 mg/mg; Buffer: 20 mM HEPES, 100 mM NaCl (pH 7.5). Measurements performed under a pressure gradient created by osmotic agents; T: 15°C.			lipids); WM: --; 150 mM NaCl; Essential-dynamics (ED) simulations were also carried out to restrain the protein in the open and closed states.
rAQP0 (no PDB structure)	0.3±0.1	[72]	OSA: measurements performed in <i>Xenopus laevis</i> oocytes injected with cRNAs coding for the protein; Buffer: Barth's solution (pH 7.4); T: 10°C.			
bAQP1 (1J4N)	2.3	[73]	PSA: proteoliposomes prepared by reverse-phase evaporation mixing purified bAqp1 and the lipids PC, PI with cholesterol (11:1:11); Buffer: 1 mM EDTA, 100 mM Na-phosphate (pH 7.4) and 200 mM octyl glucoside (OG). Measurements performed under osmotic gradient created by different solute concentrations of the Buffer (from 10 to 60-100 mM Na-phosphate); T: NS.	10.1±4.0	[67]	Same MDS setup as for bAQP0; Starting structure PDB: 1J4N.
				7.1±0.9	[74]	MDS of the protein in a lipid bilayer (5 ns x 4 replicas, NVT, 310 K); A water pressure gradient is settled by applying a constant force on all water molecules in the main direction of the channel; Starting structure PDB: 1J4N; FFs: Charmm22+CMAP (protein), Charmm27 (lipids); WM: Tip3p.
Ave±SEM: 8.8±1.7						
hAQP1 (7UZE)	6.0±1.0	[68]	Same as for bAQP0. Yield of bAQP0 in proteoliposomes: 50%.	7.5±0.5	[25]	Measurements from equilibrium MDS of the protein in a lipid bilayer (10 ns, 2fs time-step, NPT, 300 K); Starting structure PDB: 1H6I; FFs: Gromos (protein & lipids).
	1.2	[69]	Same as for bAQP0.			
	1.4	[70]	Same as for bAQP0.			
	3.4	[73]	Same as for bAQP1.			

	6.8	[75]	PSA: measurements performed under osmotic gradient produced by manitol solutions; Buffer: Tris/HCl (pH 7.4); T: 10°C.		
	11.7±1.8	[76]	PSA: measurements performed under osmotic gradient with sucrose solutions on proteoliposomes prepared by mixing purified hAqp1, <i>E. coli</i> phospholipid, OG, and Tris-HCl; Buffer: MOPS (pH 7.5); Yield of hAQP1 in proteoliposomes: 50%; T: NS.		
	5.43	[77]	Same as done by Zeidel, et al. [76]		
	4.6	[78]	Same as done by Zeidel, et al.[76], except that the concentration of hAQP1 in the proteoliposomes was varied in a range of values to determine the unit water conductance more precisely.		
Ave±SEM: 5.1±1.2					
rAQP1 (no PDB structure)	6.0	[72]	Same as for rAQP0.		
rabAQP1 (no PDB structure)	2.6	[73]	Same as for bAQP1.		
pAQP1 (no PDB structure)	1.9	[73]	Same as for bAQP1.		
oAQP1 (no PDB structure)	2.0	[73]	Same as for bAQP1.		
hAQP2 (4NEF)	9.3±0.3	[79]	PSA: measurements performed under osmotic gradient with sucrose solutions on proteoliposomes prepared by mixing	5.3±2.2	[80] MDS of the protein in a lipid bilayer (20 ns x 1 replica, NVT, 310 K); Starting structure PDB: 4NEF; FFs:

			purified hAQP2 and E. coli lipids; Buffer: 20 mM Tris-HCl, 50 mM NaCl (pH 7.2); T: NS.			Charmm22+CMAP (protein), Charmm27 (lipids); WM: Tip3p.
rAQP2 (no PDB structure)	3.3±0.2	[72]	Same as for rAQP0.			
hAQP4 (3GD8)	11.0±1.0	[81]	PSA: measurements performed under osmotic gradient with sucrose solutions on proteoliposomes prepared by mixing purified hAQP4 and a mixture of POPC, POPG and cholesterol (2:1:2); Buffer: 20 mM HEPES, 200 mM NaCl (pH 8.0); T: 4°C.	1.3±0.3 to 9.5±2.1	[82]	Same approach followed by Hashido et al. [67] (200 ns x 1 replica, NPT, 310 K); Starting structure PDB: 3GD8.
				2.9±0.5	[64]	Equilibrium MDS of the protein in a lipid bilayer (100 ns x 1 replica, NPT, 298 K); Starting structure PDB: 3GD8; FFs: Charmm22+CMAP (protein), Charmm27 (lipids); WM: Tip3p.
Ave±SEM: 4.2±1.3						
rAQP4 (2D57)	24.0±0.6	[72]	Same as for rAQP0.	7.4±2.6	[83]	Same MD setup as for bAQP0 by Hashido et al[67]; Starting structure PDB: 2D57; Introduction of a p_r -matrix method for analysis, where p_r is decomposed into contributions from each channel local region.
				9.0 to 35.0	[84]	PSA: measurements performed under osmotic gradient with sucrose solutions on proteoliposomes prepared by mixing purified rAQP4, octyl glucoside and four different mixtures of two phospholipids: 1) dierucoylphosphatidylcholine & dielaidoylphosphatidylglycerol, 2) dieicosenoylphosphatidylcholine & dielaidoylphosphatidylglycerol, 3) palmitoylloeylphosphatidylcholine & dielaidoylphosphatidylglycerol,

			4) ditridecanoylphosphatidylcholine & dimyristoylphosphatidylglycerol; Buffer: 25 mM HEPES, 50 mM NaCl, pH 7.4; T: 20°C.			extracellular side); Starting structure PDB: 2D57; FFs: Charmm36 (protein & lipids); WM: modified Tip3p; 200 mM NaCl.
Ave±SEM: 23.0±1.0				Ave±SEM: 21.8±7.6		
hAQP5 (3D9S)				5.1	[85]	Same approach followed by Hashido et al. [67] (500 ns x 1 replica, NPT, 300 K); Starting structure PDB: 3D9S.
rAQP5 (no PDB structure)	5.0±0.4	[72]	Same as for rAQP0.			
hAQP7 (6QZI)				4.8±0.2	[36]	MDS of the protein in a lipid bilayer (500-1000 ns x 5 replicas, NPT, 300 K); Starting structure PDB: 6QZI; FF: Charmm36m for protein and lipids; WM: Tip3p.
mAqpM (2F2B)	0.6	[86]	PSA: measurements performed under osmotic gradient with sucrose solutions on proteoliposomes prepared by mixing purified mAqpM, octyl glucoside and <i>E. coli</i> phospholipids; Buffer: MOPS (pH 7.5); T: 4°C.	6.4±1.4	[40]	MDS of the protein in a lipid bilayer (20ns x 1 replica, NPT, 300 K); Starting structure PDB: 6QZI; FF: Charmm36m for protein and lipids; WM: Tip3p.
	0.7	[16]	PSA: measurements performed by setting an osmotic gradient with sucrose solutions on proteoliposomes; Buffer: 1.2% octyl glucoside, 50 mM HEPES, 100mM NaCl (pH 7.4); T: 12°C.			
Ave±SEM: 0.7±0.1						
eAqpZ (1RC2)	>=10.0	[87]	PSA: measurements performed under osmotic gradient with sucrose solutions on proteoliposomes prepared by mixing purified AqpZ, octyl glucoside and lipids; Buffer: MOPS (pH 7.5); T: NS.	3.2±0.7 to 4.4±0.7	[88]	MDS of the protein in several lipid bilayer compositions (18.5-26.5ns x 1 replica, NPT, 310 K); Starting structure PDB: 1RC2; FFs: Charmm22+CMAP (protein), Charmm27 (lipids); WM: Tip3p.

	2.0	[89]	PMA: measurements performed after forming planar lipid bilayers from unilamellar vesicles (proteoliposomes) containing purified AqpZ. Transmembrane water flux measured from solute concentration changes in the immediate membrane vicinity; 50 mM MOPS, 100 mM NaCl, 0.3, μ M CaCl ₂ (pH 7.5); T: NS.	15.9 \pm 5.1	[67]	Same as for bAQP0; Starting structure PDB: 1RC2.
	Ave\pmSEM: >6.0\pm4.0			Ave\pmSEM: 8.2\pm3.9		
	2.0	[90]	PSA: measurements performed under osmotic gradient with sucrose solutions on proteoliposomes prepared by mixing purified GlpF, octyl glucoside and lipids; Buffer: MOPS (pH 7.5); T: NS.	14.0 \pm 0.4	[91]	MDS of the protein in a lipid bilayer (4 replicas, 5ns total, NPT, 310 K); Pressure gradient settled by applying a constant force on all water molecules in the main direction of the channel; Starting structure PDB: 1FX8; FFs: Charmm22+CMAP (protein), Charmm27 (lipids); WM: Tip3p.
eGlpF (1FX8)	0.7	[92]	Same as for AqpZ by Pohl et al. [89]	16.0 \pm 3.0	[67]	Same as for bAQP0; Starting structure PDB: 1LDI.
				8.6 \pm 1.1 to 13.1 \pm 3.4	[88]	MDS of the protein in several lipid bilayer compositions (20-26ns x 1 replica, NPT, 310 K); Starting structure PDB: 1FX8; FFs: Charmm22+CMAP (protein), Charmm27 (lipids); WM: Tip3p.
	Ave\pmSEM: 1.4\pm0.7			Ave\pmSEM: 13.6\pm1.5		

^a Experimental or computed water permeation rate(s) reported for the AQ(G)Ps listed in Table 1 of the main text, as well as for some AQPs without available 3D structure: rAQPx (rat aquaporins), rabAQP1 (rabbit aquaporin-1), pAQP1 (pig aquaporin-1) and oAQP1 (sheep aquaporin-1). ^b Experimental and computed (via MDS) permeabilities reported here refer to per-unit (pore channel) permeability. ^c Abbreviations: SEM, standard error of the mean; OSA, oocytes swelling assay; PSA, proteoliposome swelling assay; PMA, planar membrane assay; T, temperature of measurement; NS, not specified; MDS, molecular dynamics simulations; FF, force field; WM, water model; NPT, isothermal–isobaric ensemble; NVT, canonical ensemble.

Table S2. Corrected single-channel water permeation rates for AQ(G)Ps.^a

AQ(G)P (PDB ID)	Temperature ^b (°C)	Individual corrected single channel permeation rate ^c , p_f^{corr} ($\times 10^{-14}$ cm ³ ·s ⁻¹)	Average of p_f^{corr} ($\times 10^{-14}$ cm ³ ·s ⁻¹)
bAQP1 (1J4N)	5	32 ^d	--
eGlpF (1FX8)	5	110 ^d	--
eAqpZ (1RC2)	4	18	7.33 ^d
	5.5	5.86	
	6 to 8	4.20	
	5	1.24	
hAQP1 (7UZE)	10	6	4.6 ^d
	10	3.2	
	10	2.4	
hAQP2 (4NEF)	RT	3.27 ^d	--
hAQP4 (3GD8)	4	11 ^d	--
rAQP4 (2D57)	10	7.36 ^d	--
oAQP0 (2B6O)	15	0.0874 ^d	--
rAQP8	RT	7.64 ^d	--
mAQP11	NS	1.2 ^d	--
RsAqpZ	NS	44.4	44.7 ^d
	NS	45.0	
sAqp	20	0.32	0.35 ^d
	20	0.38	

^a Corrected single-channel water permeation rates derived from experimental measurements at low-temperature ($\leq 15^\circ\text{C}$, T in the second column), as reported by Wachlmayr *et al.* [93]. PDB entries (in parentheses) are provided for the eight AQ(G)Ps with experimentally resolved 3D structures, which were used as the QSAR training set. The remaining four AQ(G)Ps without resolved structures (no PDB entry): rAQP8 (rat aquaporin-8), mAQP11 (mouse aquaporin-11), RsAqpZ (*Rhodobacter sphaeroides*), sAqp (Soybean Aqp) served as an external test set for validation of Model 2.3b (see Table S6). ^b Temperature at which the water permeation rate was measured in the original functional assays, as reported in Table S1 of Wachlmayr *et al.* [93]. RT stands for room temperature, and NS stands for not specified. ^c Individual corrected water permeation corresponding to the reported measurement temperatures given in the second column. ^d Values used across the QSAR modeling (training or validation) described in the main text.

Table S3. Pore characteristics and additional data extracted from PoreWalker output.

AQ(G)P ^a (PDB ID)	Min pore diameter ^b (Å)	Pore regularity ^c (%)	z-coord at min pore diameter ^d	Residues at min pore diameter ^e	Min pore diameter at SF ^f (Å)	z-coord at SF ^g	Min pore diameter at NPA ^h (Å)	z-coord at NPA ⁱ
bAQP0 (1YMG)	1: 1.7	80.5	1: -13.76	1: I13, G60, I62, S63, G64, F75, F146, Y149, L157	1.7	F48: 3.46 H172: 6.11 A181: 6.62	2.7	N68: -4.62 P69: -4.53 A70: -4.63
	2: 1.7		2: 4.24	2: V24, F48*, H172*, G182, R187*, A190, Y204		R187: 2.46	2.5	N184: 0.00 P185: -0.64 A186: -
oAQP0 (2B6O)	1.4	75.0	3.22	V24, G27, F48*, E134, G182, M183, R187*, Y204	1.4	F48: 3.23 H172: 5.64 A181: 6.48	3.1	N68: -4.71 P69: - A70: -
						R187: 2.54	3.6	N184: 0.00 P185: - A186: -
bAQP1 (1J4N)	2.5	69.0	2.13	I25, I27, F58*, G59, A107, G181, I193, R197*	2.5	F58: 3.26 H182: 5.75 C191: 6.72	3.7	N78: -4.36 P79: - A80: -4.05
						R197: 2.36	2.9	N194: 0.00 P195: - A196: -
hAQP1 (7UZE)	3.2	67.6	-12.44	G68, G72, L83, L154, T156, A168, V224, Y227	3.9	F56: 3.24 H180: 4.99 C189: 6.16	3.8	N76: -4.78 P77: - A78: -4.66
						R195: 2.55	3.9	N192: 0.00 P193: - A194: -

aAQP1 (7W7S)	2.7	85.0	0.15	F23, A53, S99, V168, C169, L170, G171, I183, N184**, P185**	3.9	F50: 2.86 H172: 5.12 C181: - R187: 2.28	3.5 2.7	N70: -4.58 P71: - A72: -3.86 N184: 0.00 P185: 0.07 A186: -
kAqp1 (3ZOJ)	1: 1.9 2: 2.1	66.0	1: -17.25 2: 3.75	Y27, P29, Y31, A124, I125, R129, V191, E192, Q261 L59, A62, F92*, H212*, I214, G222, R227*	2.1	F92: 3.74 H212: 5.45 A221: 6.62 R227: 2.93	3.7 2.7	N112: -4.40 P113: - A114: - N224: 0.00 P225: - A226: -
hAQP2 (4NEF)	2.2	70.3	5.95	G27, A45, A47, A101, C181*, S188	2.2	F48: 3.72 H172: - C181: 6.76 R187: 2.63	4.3 3.0	N68: -4.60 P69: - A70: - N184: 0.00 P185: - A186: -
hAQP4 (3GD8)	2.7	64.9	3.69	V49, S52, F77*, G129, S211, R216*	2.7	F77: 4.03 H201: - A210: 6.57 R216: 2.47	3.5 5.2	N97: -4.60 P98: - A99: - N213: 0.00 P214: - A215: -
rAQP4 (2D57)	2.3	57.9	4.83	V49, S52, F77*, G200, H201*, S211	2.3	F77: 4.22 H201: 6.61 A210: 6.97 R216: 2.72	5.0 3.8	N97: -4.54 P98: - A99: - N213: 0.00 P214: - A215: -1.48

hAQP5 (3D9S)	1.7	33.3	4.55	V25, F27, A48, F49*, H173*, S183, R188*	1.7	F49: 3.76 H173: 5.56 C182: 6.60 R188: 2.94	5.0 3.8	N69: -4.47 P70: - A71: - N185: 0.00 P186: - A187: -0.91
hAQP7 (6QZI)	3.2	41.0	3.46	M48, F74*, V211, Y223*, A224, R229*, D330	3.2	F74: 3.97 G214: - Y223: 4.88 R229: 2.61	4.8 5.6	N94: -4.35 A95: - A96: - N226: 0.00 P227: - S228: -
hAQP10 (6F7H)	1: 1.9 2: 4.6	51.2	1: -14.15 ^Δ 2: 3.85	1: Q23, N75, G78, M89, L95, A176, I177, L178, G184, V185, P186, G188, Y260 2: M35, L37, T38, G62*, S63, A65, A111, A114, G202*, I211*, P212, R217*, D218	4.6	G62: 4.88 G202: 5.46 I211: 4.54 R217: 2.63	4.9 4.8	N82: -4.44 P83: - A84: - N214: 0.00 P215: - A216: -
SoPIP2;1 (1Z98)	2.2	39.5	4.41	L52, I54, T55, F81*, G133, H210*, T219*, G220, R225, G228	2.2	F81: 4.27 H210: 5.57 T219: 5.79 R225: 2.78	3.6 2.6	N101: -4.31 P102: - A103: - N222: 0.00 P223: - A224: -
mAqpM (2F2B)	2.6	39.5	1.28	L18, F62*, A65, A111, V183, I186, L198, N199**, R202*	2.6	F62: 2.97 I187: 5.38 S196: 5.95 R202: 2.43	4.8 3.5	N82: -4.52 P83: -4.16 A84: - N199: 0.00 P200: - A201: -

aAqpM (3NE2)	2.0	64.3	1.02	F63*, A66, L199, N200**, R203*, P229	2.0	F63: 2.16 I188: 4.63 S197: 5.57 R203: 2.33	4.5 3.4	N83: -4.53 P84: -3.99 A85: - N200: 0.00 P201: - A202: -
OsNIP2;1 (7CJS)	4.0	40.5	2.86	V62, T65, I86, G88*, C204, T216, S217, R222*	4.0	G88: 2.79 S207: 5.49 G216: 6.42 R222: 2.09	4.6 5.2	N108: -4.50 P109: - A110: - N219: 0.00 P220: - A221: -
AtTIP2;1 (5I32)	2.6	56.4	-4.58	A70, V82, N83**, A85**, Q108, L153, I180	3.6	H63: 4.20 I185: 6.47 G194: 6.41 R200: 2.59	2.6 3.9	N83: -4.46 P84: - A85: -4.29 N197: 0.00 P198: - A199: -
AtPIP2;4 (6QIM)	1: 2.1 2: 3.1	57.5	1: -16.06 ^Δ 2: 1.94	1: L114, F115, A117, V120, R124, F186, T189, V202 2: F51, G88, M90, A136, V215, I227, N228, R231*,	3.4	F87: 4.07 H216: 5.24 T225: 5.91 R231: 3.45	3.6 4.1	N107: -4.69 P108: - A109: -4.82 N228: 0.00 P229: -0.85 A230: -0.76
eAqpZ (1RC2)	1.8	30.0	3.25	V16, G19, F43*, H174*, S184, R189*, S190	2.0	F43: 3.02 H174: 4.93 T183: 6.05 R189: 2.59	3.6 3.5	N63: -4.58 P64: - A65: - N186: 0.00 P187: - A188: -

aAqpZ2 (3LLQ)	2.0	39.0	4.58	A40, F43*, I135, E136, H172*, T181*, S182, S188	2.0	F43: 3.25 H172: 5.55 T181: 6.32 R187: 2.45	5.1 3.0	N63: -4.39 P64: -4.42 A65: - N184: 0.00 P185: - A186: -
pAqgp (3C02)	3.1	61.0	4.55	M24, L48, W50*, L178, F190*, A191, D197, P223	3.1	W50: 5.08 G181: - F190: 5.45 R196: 2.28	4.9 4.0	N70: -4.34 L71: - A72: - N193: 0.00 P194: - S195: -
eGlpF (1FX8)	3.0	48.6	3.59	S45, W48*, A97, F200*, A201, R206*, P236	3.0	W48: 4.37 G191: - F200: 4.13 R206: 2.78	4.9 6.1	N68: -4.26 P69: - A70: - N203: 0.00 P204: - A205: -

^a Aquaporin full names and their source organisms are given in Table 1 of the main text. ^b Minimum pore diameter calculated by the PoreWalker [56] along the z-coordinates (z-axis) of the AQ(G)Ps' pore. The z-axis refers to that perpendicular to the xy cellular membrane plane, i.e. the main/longest pore axis. In cases where a minimum pore diameter appears near the terminal ends of the pore (see diameter profiles in Fig. S1 and Fig. 4a of the main text), a second minimum closer to the central part is also reported. ^c Measure of regularity of the pore as issued by PoreWalker. The value refers to the percentage of pore centers (at 1 Å step) that could be fitted to a line. ^d z-coordinates where the pore exhibits the minimum diameter(s). Values extracted from the diameter plots included in Fig. S1 and Fig.4a (left top panels), which were obtained at 3 Å step by PoreWalker. The z-coordinate associated to each amino acid is that of their beta carbon (βC). The z-coordinates along the whole z-axis were shifted to place the beta carbon (βC) of the asparagine (N) in the second NPA motif in the center of the z-coordinate system (z=0), for all the AQPs analyzed (check it out in the last column, in bold). This way the z-coordinates are aligned according to the equivalent residues in the AQPs (as if they were aligned structurally). With a delta (Δ) symbol appear those z-coordinates of minima located near the cytosolic or the extracellular interfaces of the pore. ^e Residues located within a z-coordinate range of ±2 Å of the pore minimum. With an asterisk (*) those amino acids forming the SF motifs. ^f Minimum pore diameter in the z-coordinates range encompassing the four residues forming the selectivity filter (SF). ^g z-coordinates of the amino acids (βC) forming the SF motif. ^h Minimum pore

diameter found within the z-coordinates range of the six residues forming the two NPA motifs. ⁱ z-coordinates of the amino acids (β C) forming the NPA motifs. In bold the asparagine in the second NPA motif that constitute the reference ($z=0$) coordinate. **Note:** All the information used to extract the data showed in this table is contained in the PoreWalker output files, provided as **Supplementary Files**. Pore diameter profiles and additional information on the pore shape are given more visually in Fig. S1 and Fig. 4a of the main text.

Table S4. Sequences of the NPA and the selectivity filter (SF) motifs of selected AQ(G)Ps. The symbols highlight the difference or identity across the sequences of the NPA and the SF motifs.

AQ(G)P ^a	PDB ID	Sequences of the NPA motifs ^b				Sequence of the SF motif ^c				
bAQP0	1YMG	NPA 68-70	&	NPA 184-186	⊖	Phe48	His172	Arg187	Ala181	△
oAQP0	2B6O	NPA 68-70	&	NPA 184-186	⊖	Phe48	His172	Arg187	Ala181	△
bAQP1	1J4N	NPA 78-80	&	NPA 194-196	⊖	Phe58	His182	Arg197	Cys191	⊖
hAQP1	7UZE	NPA 76-78	&	NPA 192-194	⊖	Phe56	His180	Arg195	Cys189	⊖
aAQP1	7W7S	NPA 70-72	&	NPA 184-186	⊖	Phe50	His172	Arg187	Cys181	⊖
kAqp1	3ZOJ	NPA 112-114	&	NPA 224-226	⊖	Phe92	His212	Arg227	Ala221	△
hAQP2	4NEF	NPA 68-70	&	NPA 184-186	⊖	Phe48	His172	Arg187	Cys181	⊖
hAQP4	3GD8	NPA 97-99	&	NPA 213-215	⊖	Phe77	His201	Arg216	Ala210	△
rAQP4	2D57	NPA 97-99	&	NPA 213-215	⊖	Phe77	His201	Arg216	Ala210	△
hAQP5	3D9S	NPA 69-71	&	NPA 185-187	⊖	Phe49	His173	Arg188	Cys182	⊖
hAQP7	6QZI	NAA 94-96	&	NPS 226-228	⊖	Phe74	Gly214	Arg229	Tyr223	⊖
hAQP10	6F7H	NPA 82-84	&	NPA 214-216	⊖	Gly62	Gly202	Arg217	Ile211	⊖
SoPIP2;1	1Z98	NPA 101-103	&	NPA 222-224	⊖	Phe81	His210	Arg225	Thr219	⊖
mAqpM	2F2B	NPA 82-84	&	NPA 199-201	⊖	Phe62	Ile187	Arg202	Ser196	⊗
aAqpM	3NE2	NPA 83-85	&	NPA 200-202	⊖	Phe63	Ile188	Arg203	Ser197	⊗

OsNIP2;1	7CJS	NPA 108-110	&	NPA 219-221	⊖	Gly88	Ser207	Arg222	Gly216	⊕
AtTIP2;1	5I32	NPA 83-85	&	NPA 197-199	⊖	His63	Ile185	Arg200	Gly194	⊗
AtPIP2;4	6QIM	NPA 107-109	&	NPA 228-230	⊖	Phe87	His216	Arg231	Thr225	□
eAqpZ	1RC2	NPA 63-65	&	NPA 186-188	⊖	Phe43	His174	Arg189	Thr183	□
aAqpZ2	3LLQ	NPA 63-65	&	NPA 184-186	⊖	Phe43	His172	Arg187	Thr181	□
pAqgp	3C02	NLA 70-72	&	NPS 193-195	△	Trp50	Gly181	Arg196	Phe190	⊞
eGlpF	1FX8	NPA 68-70	&	NPA 203-205	⊖	Trp48	Gly191	Arg206	Phe200	⊞

^a Full names and AQ(G)Ps' source organisms are given in Table 1 of the main text. ^b Information retrieved from the UniProtKB database [94]. ^c Information retrieved in some cases from the reviewed literature and in the others from structural alignment.

Table S5. Resolution, experimental conditions and other relevant information on crystallization of AQ(G)Ps in the modeled datasets.^a

^a The table is provided as an Excel **Supplementary File**. Data reported in this table has been retrieved from the Protein Data Bank [95] website ('Experiment' tab in each PDB entry).

Table S6. Computed values of the PDs retained in Model 3.2b, along with predicted p_f^{corr} values and residuals for the four AQPs used for external validation.

		rAQP8	mAQP11	RsAqpZ	sAqp
PDs retained in Model 2.3b	<i>Regularity</i> ^a	7.317	7.838	5.385	6.578
	N_H ^a	10	9	9	11
	<i>Sites</i> ^{+a}	1	14	6	7
Values used for validation of Model 2.3b	Predicted p_f^{corr} ^b	2.05	14.98	35.93	2.28
	(Pred. $\ln p_f^{corr}$)	(0.72)	(2.71)	(3.58)	(0.83)
	Observed p_f^{corr} ^b	1.2	7.64	44.7	0.35
	(Obs. $\ln p_f^{corr}$)	(0.18)	(2.03)	(3.80)	(-1.05)
	Pred. – Obs. non-log ^b	0.85	7.34	8.77	1.93

^a PD values were computed for the external AQ(G)Ps using the same procedures and tools described in the Materials and Methods for the training set, and were standardized using the training-set mean and standard deviation. ^b Values reported in the original scale of permeation rates ($\times 10^{-14} \text{ cm}^3 \cdot \text{s}^{-1}$).

Table S7. Composition (in %) per amino acid (AA) and per amino acid type for the AQ(G)Ps' pore lining compared to whole protein.

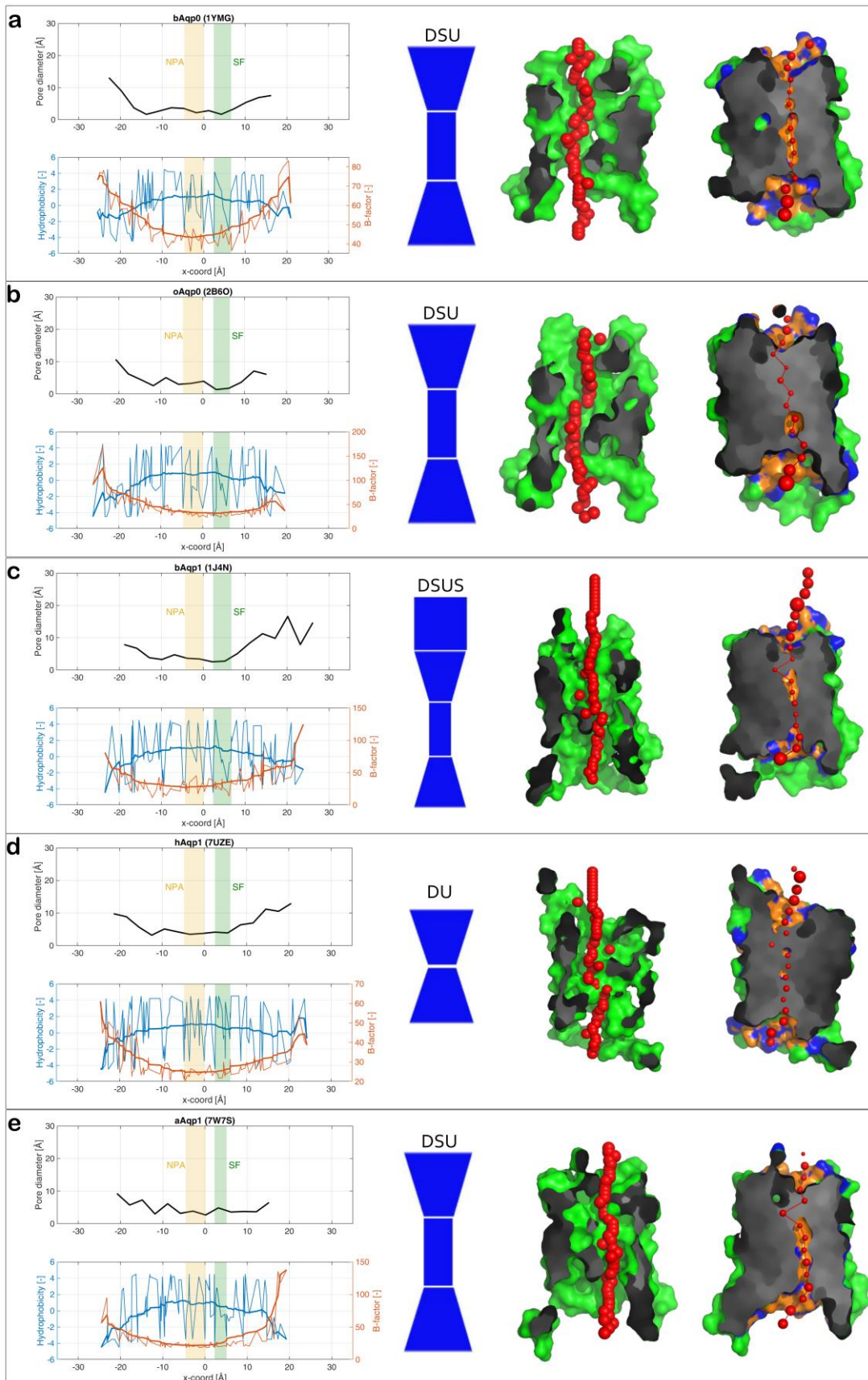
AQ(G)P ^a (PDB ID)	Composition on... ^b	Non-polar AAs										Polar AAs w/o charges						Polar AAs with (-) charges			Polar AAs with (+) charge				
		Gly	Ala	Val	Ile	Leu	Met	Pro	Phe	Trp	Total	Ser	Thr	Cys	Tyr	Asn	Gln	Total	Asp	Glu	Total	Arg	Lys	His	Total
bAQP0 (1YMG)	Whole protein	9.9	12.2	9.5	3.4	14.4	1.9	4.9	6.8	1.9	65.0	7.2	4.9	1.1	3.0	3.0	3.0	22.4	0.8	3.4	4.2	4.9	1.1	2.3	8.4
	Pore lining	11.1	11.1	8.9	4.4	12.2	3.3	3.3	5.6	1.1	61.1	7.8	4.4	0.0	4.4	5.6	1.1	23.3	1.1	2.2	3.3	4.4	2.2	5.6	12.2
oAQP0 (2B6O)	Whole protein	9.9	12.2	9.9	3.4	14.4	1.5	4.9	7.2	1.9	65.4	6.5	5.7	0.8	3.0	3.0	3.0	22.1	0.8	3.4	4.2	4.9	1.1	2.3	8.4
	Pore lining	8.8	9.9	9.9	3.3	12.1	3.3	3.3	5.5	0.0	56.0	5.5	4.4	1.1	5.5	6.6	3.3	26.4	0.0	2.2	2.2	9.9	0.0	5.5	15.4
bAQP1 (1J4N)	Whole protein	9.6	10.3	7.7	9.6	12.2	1.5	3.3	4.8	1.5	60.5	8.9	4.8	1.5	1.8	3.3	3.3	23.6	4.8	2.2	7.0	3.7	3.0	2.2	8.9
	Pore lining	13.3	10.0	7.8	10.0	11.1	1.1	3.3	4.4	0.0	61.1	5.6	5.6	2.2	1.1	6.7	5.6	26.7	2.2	0.0	2.2	5.6	0.0	4.4	10.0
hAQP1 (7UZE)	Whole protein	10.0	10.4	8.2	8.6	12.3	1.1	2.6	4.8	1.5	59.5	8.6	5.6	1.5	1.9	4.1	3.0	24.5	4.8	2.2	7.1	4.1	3.0	1.9	8.9
	Pore lining	12.4	9.0	7.9	6.7	10.1	0.0	1.1	4.5	0.0	51.7	5.6	6.7	2.2	2.2	4.5	4.5	25.8	3.4	1.1	4.5	11.2	3.4	3.4	18.0
aAQP1 (7W7S)	Whole protein	10.3	11.1	9.2	5.7	12.3	2.7	4.2	4.2	1.1	60.9	7.3	5.4	1.9	2.3	5.7	2.3	24.9	3.4	2.7	6.1	2.7	3.8	1.5	8.0
	Pore lining	8.6	9.7	7.5	7.5	9.7	2.2	3.2	4.3	0.0	52.7	11.8	3.2	3.2	2.2	8.6	4.3	33.3	1.1	2.2	3.2	3.2	4.3	3.2	10.8
kAqp1 (3ZOJ)	Whole protein	10.4	15.8	5.0	7.9	8.2	3.2	6.1	7.2	2.9	66.7	4.7	5.0	0.7	3.6	4.3	3.2	21.5	2.5	2.9	5.4	3.6	1.4	1.4	6.5
	Pore lining	12.9	17.2	6.5	6.5	8.6	0.0	3.2	6.5	3.2	64.5	2.2	5.4	1.1	4.3	7.5	4.3	24.7	1.1	3.2	4.3	3.2	2.2	1.1	6.5
hAQP2 (4NEF)	Whole protein	8.9	12.9	8.9	4.4	14.8	1.1	5.2	5.2	1.8	63.1	7.0	5.2	1.5	1.5	2.6	3.0	20.7	2.6	4.4	7.0	4.8	1.5	3.0	9.2
	Pore lining	9.1	14.1	8.1	7.1	7.1	1.0	3.0	6.1	1.0	56.6	9.1	4.0	3.0	1.0	5.1	2.0	24.2	3.0	3.0	6.1	6.1	2.0	5.1	13.1

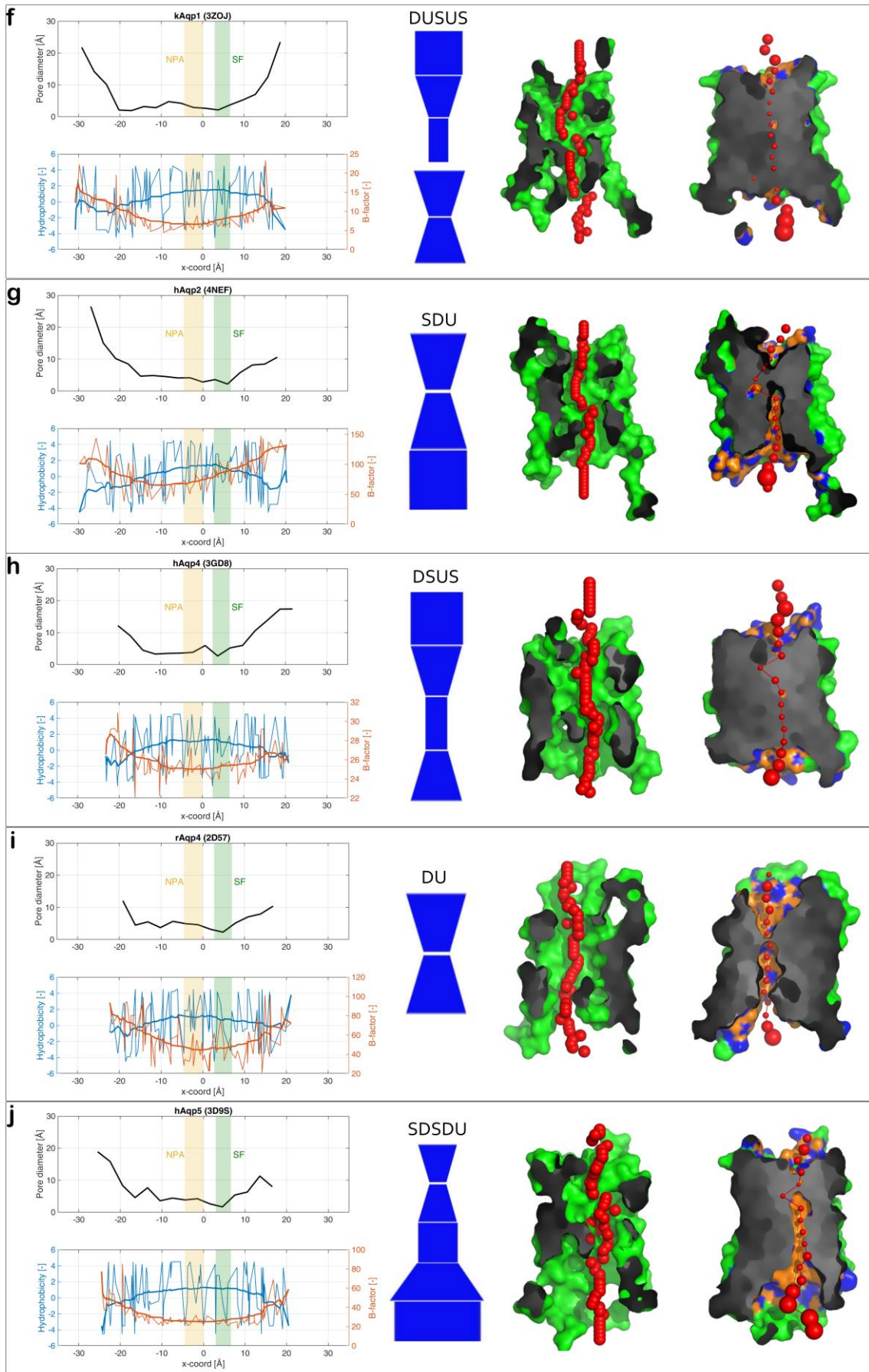
hAQP4 (3GD8)	Whole protein	10.5	8.7	10.2	8.0	8.0	3.1	3.7	5.3	2.2	59.8	6.5	5.9	2.5	2.2	2.8	2.5	22.3	3.4	4.3	7.7	3.4	4.6	2.2	10.2
	Pore lining	11.4	6.8	11.4	10.2	3.4	8.0	3.4	4.5	0.0	59.1	9.1	5.7	2.3	1.1	6.8	2.3	27.3	2.3	1.1	3.4	2.3	4.5	3.4	10.2
rAQP4 (2D57)	Whole protein	10.5	9.3	10.5	8.0	8.0	2.8	3.7	4.6	2.2	59.8	7.7	5.6	2.5	2.2	2.8	2.2	22.9	3.4	4.3	7.7	3.1	4.3	2.2	9.6
	Pore lining	12.2	6.7	11.1	10.0	3.3	6.7	0.0	5.6	1.1	56.7	12.2	5.6	2.2	1.1	4.4	1.1	26.7	3.3	3.3	6.7	2.2	3.3	4.4	10.0
hAQP5 (3D9S)	Whole protein	8.7	12.8	8.3	6.4	13.6	1.9	4.9	6.4	1.5	64.5	6.4	5.7	1.1	2.3	4.2	3.0	22.6	1.1	4.2	5.3	3.8	2.6	1.1	7.5
	Pore lining	8.5	9.6	6.4	10.6	9.6	1.1	4.3	8.5	0.0	58.5	7.4	5.3	2.1	3.2	7.4	3.2	28.7	1.1	1.1	2.1	6.4	2.1	2.1	10.6
hAQP7 (6QZI)	Whole protein	10.2	8.5	9.4	6.1	10.2	4.4	6.1	5.6	2.3	62.9	7.0	5.6	0.6	3.2	3.5	2.3	22.2	1.5	3.8	5.3	3.8	2.6	3.2	9.6
	Pore lining	9.7	8.6	12.9	8.6	7.5	5.4	5.4	6.5	1.1	65.6	4.3	5.4	1.1	5.4	4.3	1.1	21.5	2.2	3.2	5.4	4.3	1.1	2.2	7.5
hAQP10 (6F7H)	Whole protein	10.6	12.0	9.3	4.0	14.6	3.0	6.3	4.0	1.7	65.4	4.7	6.0	1.7	3.0	3.7	3.7	22.6	1.7	3.7	5.3	2.7	2.0	2.0	6.6
	Pore lining	11.1	13.1	11.1	7.1	11.1	4.0	7.1	4.0	1.0	69.7	4.0	5.1	1.0	4.0	3.0	3.0	20.2	2.0	3.0	5.1	3.0	0.0	2.0	5.1
SoPIP2;1 (1Z98)	Whole protein	10.7	13.5	9.3	7.5	8.5	1.8	5.0	7.1	2.1	65.5	5.3	5.0	1.4	3.2	3.2	2.1	20.3	2.5	2.5	5.0	2.8	3.9	2.5	9.3
	Pore lining	12.0	11.0	10.0	11.0	6.0	0.0	4.0	8.0	0.0	62.0	5.0	7.0	1.0	4.0	5.0	2.0	24.0	1.0	1.0	2.0	4.0	3.0	5.0	12.0
mAqpM (2F2B)	Whole protein	14.6	12.6	6.5	12.2	9.8	2.4	4.9	6.5	1.6	71.1	5.3	6.5	1.2	3.7	3.7	1.6	22.0	1.2	2.0	3.3	1.6	1.6	0.4	3.7
	Pore lining	16.2	12.1	6.1	15.2	8.1	2.0	4.0	3.0	1.0	67.7	4.0	9.1	1.0	3.0	3.0	1.0	21.2	2.0	2.0	4.0	3.0	3.0	1.0	7.1
aAqpM (3NE2)	Whole protein	15.0	14.6	7.7	11.0	10.2	2.8	5.7	6.1	1.6	74.8	2.8	6.1	0.4	3.3	3.3	1.2	17.1	1.6	2.4	4.1	2.4	1.2	0.4	4.1
	Pore lining	13.3	13.3	7.6	13.3	8.6	2.9	7.6	3.8	1.0	71.4	2.9	8.6	0.0	1.9	4.8	1.0	19.0	1.9	2.9	4.8	3.8	0.0	1.0	4.8
OsNIP2;1 (7CJS)	Whole protein	8.4	10.7	9.7	6.7	7.4	3.7	4.4	6.0	1.7	58.7	8.7	7.4	1.0	2.3	3.7	3.0	26.2	3.4	3.0	6.4	3.4	2.7	2.7	8.7

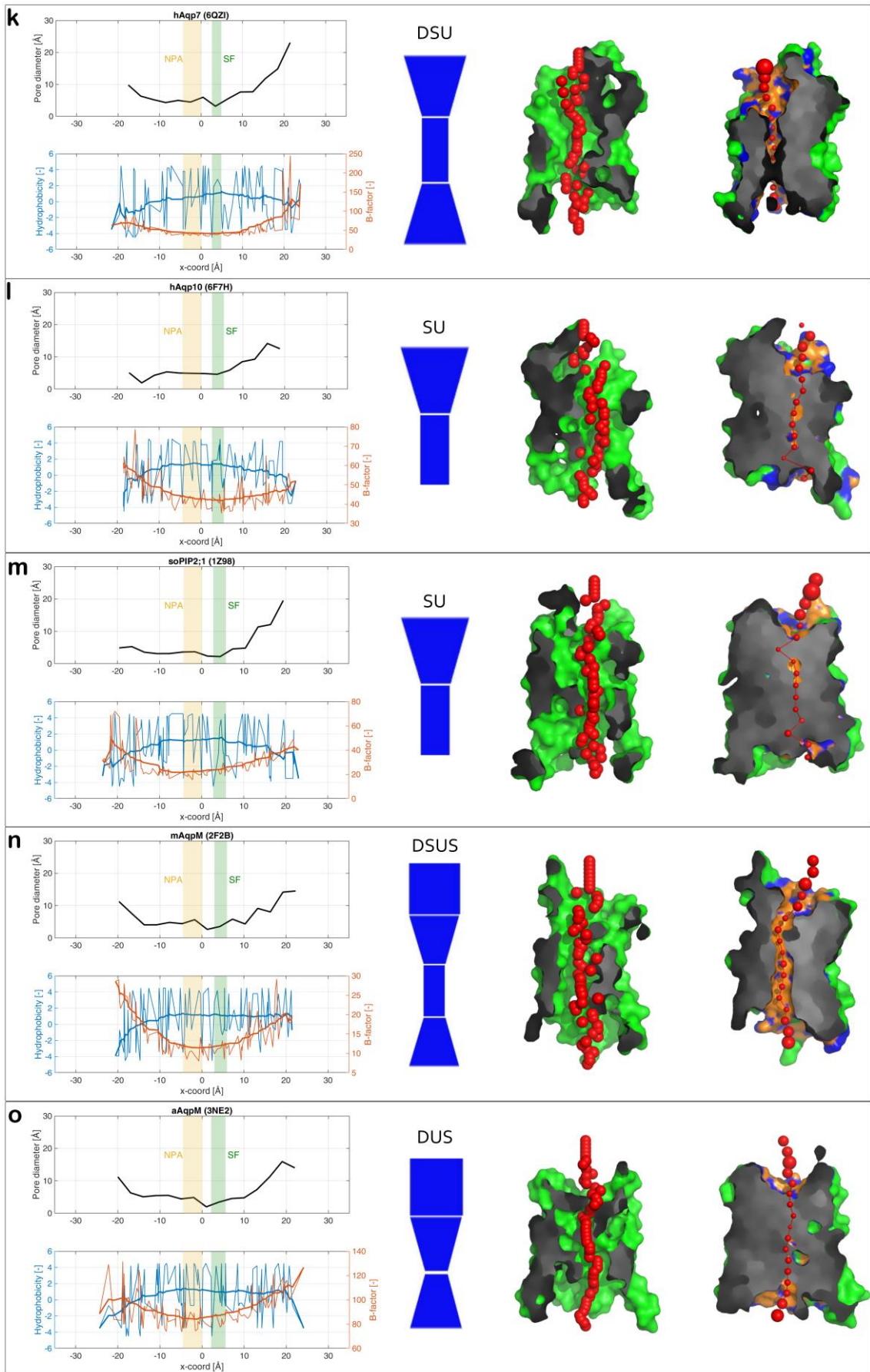
	Pore lining	15.7	14.3	11.4	5.7	4.3	7.1	2.9	2.9	0.0	64.3	5.7	8.6	1.4	1.4	2.9	2.9	22.9	2.9	1.4	4.3	4.3	0.0	4.3	8.6
AtTIP2;1 (5I32)	Whole protein	14.4	16.4	10.0	7.2	10.0	1.6	4.0	6.8	1.2	71.6	7.6	5.2	0.8	3.2	2.0	0.8	19.6	2.8	1.6	4.4	0.8	1.6	2.0	4.4
	Pore lining	8.3	16.7	9.7	6.9	8.3	2.8	4.2	1.4	0.0	58.3	11.1	8.3	0.0	4.2	4.2	1.4	29.2	2.8	1.4	4.2	2.8	1.4	4.2	8.3
AtPIP2;4 (6QIM)	Whole protein	11.7	13.7	8.6	7.2	7.6	1.7	5.2	7.2	1.7	64.6	4.5	5.2	1.7	4.5	2.7	1.7	20.3	4.1	2.4	6.5	3.8	3.4	1.4	8.6
	Pore lining	10.5	11.6	11.6	9.5	7.4	1.1	5.3	5.3	0.0	62.1	2.1	8.4	2.1	4.2	5.3	3.2	25.3	2.1	1.1	3.2	4.2	3.2	2.1	9.5
eAqpZ (1RC2)	Whole protein	15.2	14.7	9.5	7.4	11.3	1.3	3.9	7.8	2.2	73.2	5.2	4.8	0.9	2.2	1.7	1.3	16.0	1.3	3.0	4.3	2.2	2.2	2.2	6.5
	Pore lining	14.1	10.9	8.7	5.4	7.6	1.1	4.3	12.0	2.2	66.3	7.6	3.3	1.1	1.1	4.3	0.0	17.4	1.1	3.3	4.3	2.2	4.3	5.4	12.0
aAqpZ2 (3LLQ)	Whole protein	15.4	15.4	9.2	7.9	11.8	0.9	4.4	7.5	2.2	74.6	5.7	5.3	0.4	2.2	1.8	1.8	17.1	0.9	2.2	3.1	1.8	1.8	1.8	5.3
	Pore lining	13.6	12.5	10.2	8.0	8.0	0.0	3.4	11.4	1.1	68.2	4.5	4.5	1.1	1.1	4.5	1.1	17.0	1.1	2.3	3.4	3.4	3.4	4.5	11.4
pAqgp (3C02)	Whole protein	10.5	5.4	8.5	7.4	14.0	1.2	2.7	9.7	1.6	60.9	7.4	5.0	2.3	3.5	4.7	1.2	24.0	3.9	2.7	6.6	1.6	5.0	1.9	8.5
	Pore lining	8.6	7.5	8.6	8.6	12.9	1.1	3.2	5.4	3.2	59.1	6.5	5.4	1.1	2.2	4.3	1.1	20.4	4.3	3.2	7.5	3.2	6.5	3.2	12.9
eGlpF (1FX8)	Whole protein	11.4	12.1	9.3	7.5	10.7	2.1	5.3	7.5	1.8	67.6	4.3	5.3	2.1	2.5	2.5	2.5	19.2	2.8	3.2	6.0	2.5	2.8	1.8	7.1
	Pore lining	13.1	11.1	7.1	9.1	10.1	2.0	6.1	7.1	2.0	67.7	2.0	6.1	2.0	3.0	3.0	2.0	18.2	5.1	0.0	5.1	5.1	2.0	2.0	9.1
ALL PROTEINS	Whole protein	11.2	12.1	8.8	7.2	11.0	2.2	4.6	6.3	1.8	65.3±1.1	6.3	5.5	1.4	2.8	3.3	2.4	21.6±0.6	2.6	3.0	5.6±0.3	3.1	2.6	1.9	7.6±0.4
	Pore lining	11.6	11.2	9.1	8.4	8.5	2.6	3.9	5.8	0.9	61.8±1.2	6.2	5.9	1.5	2.8	5.1	2.3	23.8±0.9	2.1	2.0	4.2±0.3	4.5	2.4	3.4	10.2±0.7

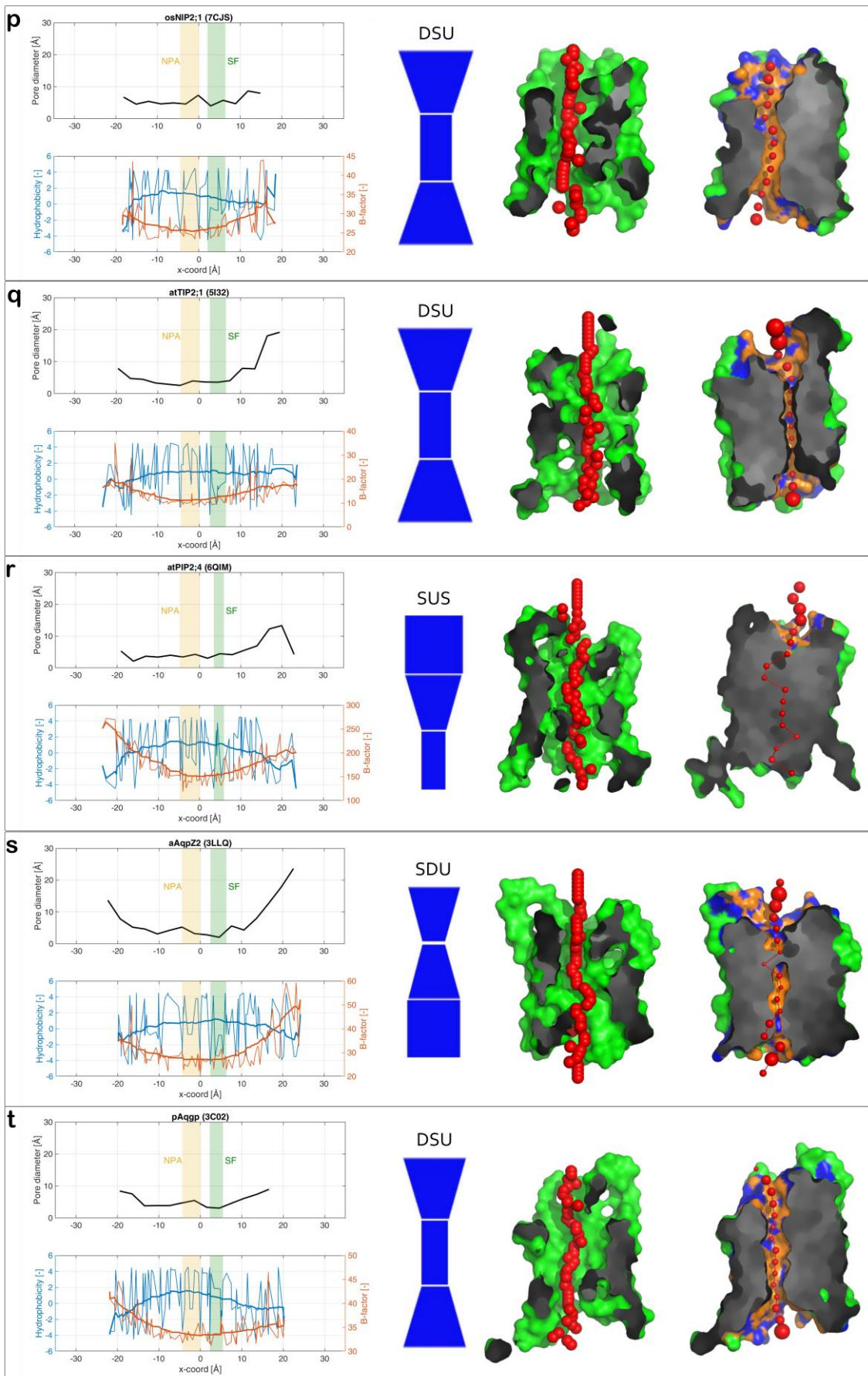
^a Aquaporins full names and their source organisms are given in Table 1 of the main manuscript. ^b Statistics for the whole protein composition obtained from the canonical aquaporin sequences retrieved from UniProtKB database [94], and statistics for the pore lining composition calculated based on the information given by PoreWalker [56]. FASTA files with the protein sequence from UniProtKB are provided as **Supplementary Files** along with all the output files issued by PoreWalker including the pore-lining amino acidic composition.

SUPPLEMENTARY FIGURES









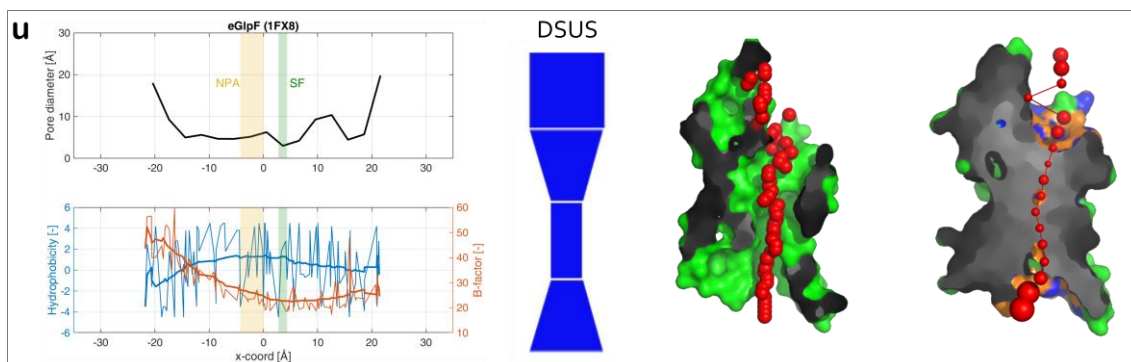


Figure S1. Pore properties profiles and geometrical shape for all the AQ(G)Ps listed in Table 1 of the main text, except for *E. coli* AqpZ included in the main article. Left top panels: diameter profile along the pore principal axis (z-coordinate) at 3Å step as calculated by the PoreWalker tool [56]. Left bottom panels: per-residue hydrophobicity index (blue) and B-factor (orange) of amino acids in the pore lining along the pore z-coordinate, as calculated by the Discovery Studio (BIOVIA, Dassault Systèmes) [96] and as obtained from the crystal PDB files, respectively. The thicker lines are smoothed curves (noise removed). Vertical bands depicted show the z-coordinates ranges where the NPA (orange) and SF (green) motifs are located. The blue funnel-like form at the center is a 2D projection of the predicted pore shape as calculated by variations of diameter values along the pore: the bottom of the pore axis (i.e., the lowest z-coordinate) correspond to the bottom of the stack. In the letter code on the top of the form, 'D' indicates a conical frustum generated by decreasing pore diameter values, i.e. the diameter of the lower base of the frustum is bigger than the diameter of its upper circle, 'U' indicates the opposite conical frustum, i.e., lower base diameter smaller than upper base diameter, and 'S' indicates a cylinder (the code ordering from bottom to top). The two longitudinal cross-sectional images are selected cuts along the pore's z-coordinate issued by PoreWalker, where the pore regularity is shown in the first cross-sectional image through red spheres located at the centre of the pore every 1Å step, whereas the pore dimension is represented in the second cross-sectional image by red spheres—at the center of the pore at 3Å step—, whose sizes are proportional to the pore diameter calculated at that point. In the latter, orange and blue areas show pore-lining atoms and corresponding residues, respectively. (a) bAQP0 (PDB ID 1YMG); (b) oAQP0 (PDB ID 2B6O); (c) bAQP1 (PDB ID 14JN); (d) hAQP1 (PDB ID 7UZE); (e) aAqp1 (PDB ID 7W7S); (f) kAqp1 (PDB ID 3ZOJ); (g) hAQP2 (PDB ID 4NEF); (h) hAQP4 (PDB ID 3GD8); (i) rAQP4 (PDB ID 2D57); (j) hAQP5 (PDB ID 3D9S); (k) hAQP7 (PDB ID 6QZI); (l) hAQP10 (PDB ID 6F7H); (m) SoPIP2;1 (PDB ID 1Z98); (n) mAqpM (PDB ID 2F2B); (o) aAqpM (PDB ID 3NE2); (p) OsNIP2;1 (PDB ID 7CJS); (q) AtTIP2;1 (PDB ID 5I32); (r) AtPIP2;4 (PDB ID 6QIM); (s) aAqpZ2 (PDB ID 3LLQ); (t) pAqgp (PDB ID 3C02); (u) eGlpF (PDB ID 1FX8). **Notes:** Aquaporin full names and their source organisms are given in Table 1 of the main text. Amino acids in the pore lining are reported in the PoreWalker's output files (**Supplementary Files**). The z-coordinates in the panels at the left (diameter, hydrophobicity index and B-factors profiles) were shifted from the original ones issued by PoreWalker, to place the beta carbon (β C) of the asparagine (N) in the second NPA motif at the center of the z-coordinate system ($z=0$). This ensures that all the AQ(G)Ps are aligned to have the same reference z-coordinate.

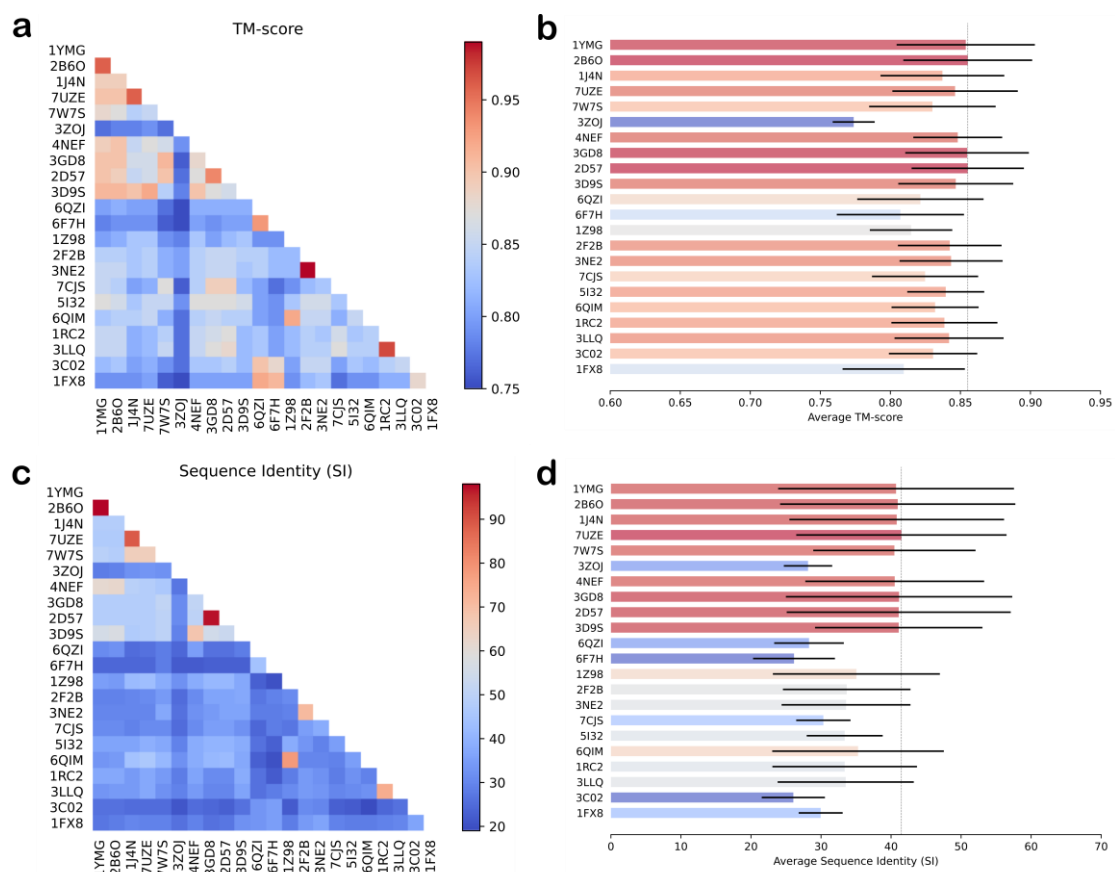


Figure S2. Structural and sequence comparisons of AQ(G)Ps. (a) TM-score-based pairwise map. (b) Per structure averaged TM-score against all other structures (bars). (c) Sequence identity (SI) pairwise map. (d) Per structure averaged SI against all other structures (bars). A min-max normalization is adopted for the bars coloring. The black lines at the right-hand side of the bars represent the standard deviations, whereas the dashed vertical lines indicate the maximum averages among all the structures. The initial chain of the tetrameric AQ(G)Ps' PDB structures was taken for the calculations. The corresponding AQ(G)Ps of the compared structures (PDBs) are given in Table 1 of the main text.

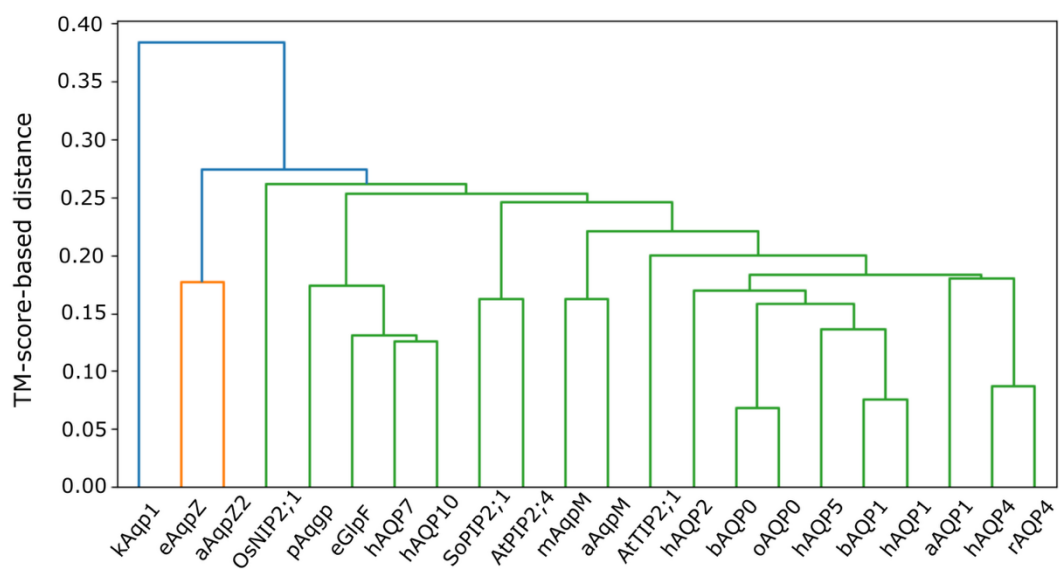


Figure S3. Hierarchical clustering based on the pairwise TM-score of AQ(G)Ps. The PDB IDs of the structures used are those reported in Table 1 of the main text. The single linkage method from the Python SciPy library (v.1.11.4) [97] was used for the clustering.

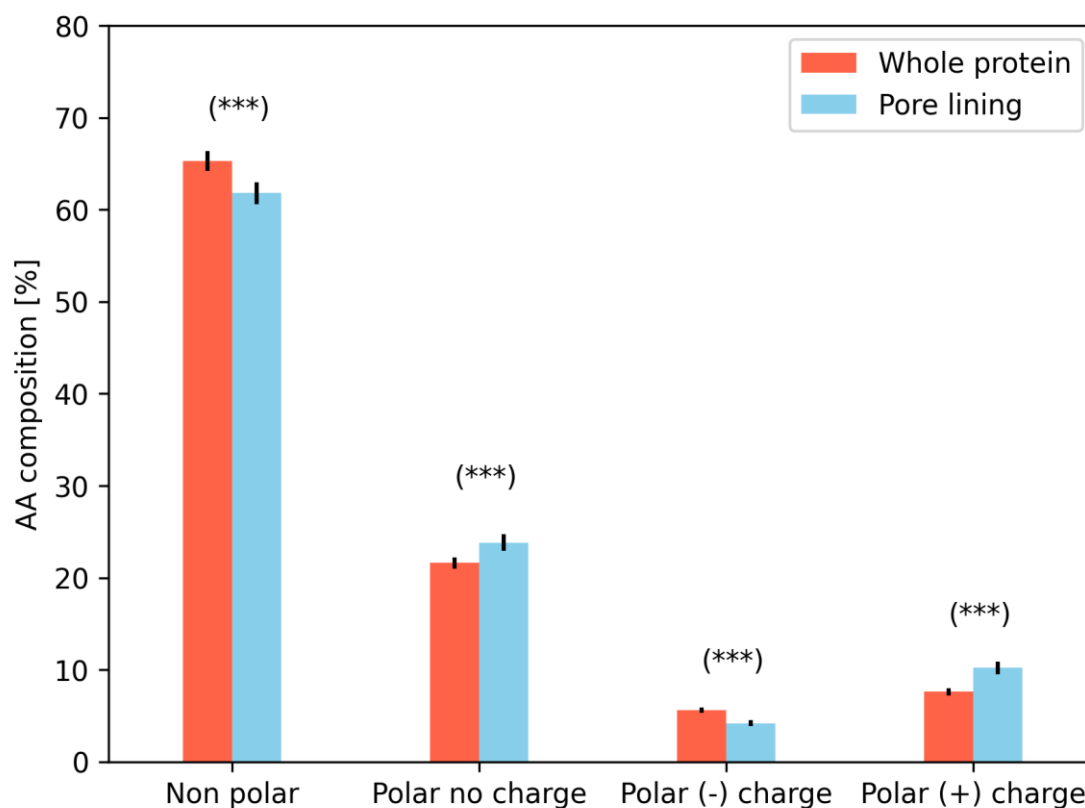


Figure S4. Comparative depiction of the per-amino-acid type composition (in %) both in the whole protein and the pore lining across the AQ(G)Ps investigated. The statistical significance (p -value < 0.01) of a t-test for mean differences is shown on each pair of compared bars. Data on the whole protein composition were obtained from the canonical aquaporin sequences retrieved from UniProt database [98]. Statistics on the pore lining composition were calculated based on the information given by PoreWalker [56]. FASTA files with the protein sequences used are provided as **Supplementary Files** along with the PoreWalker output files, which contain the pore shape, size and residue-level lining composition.

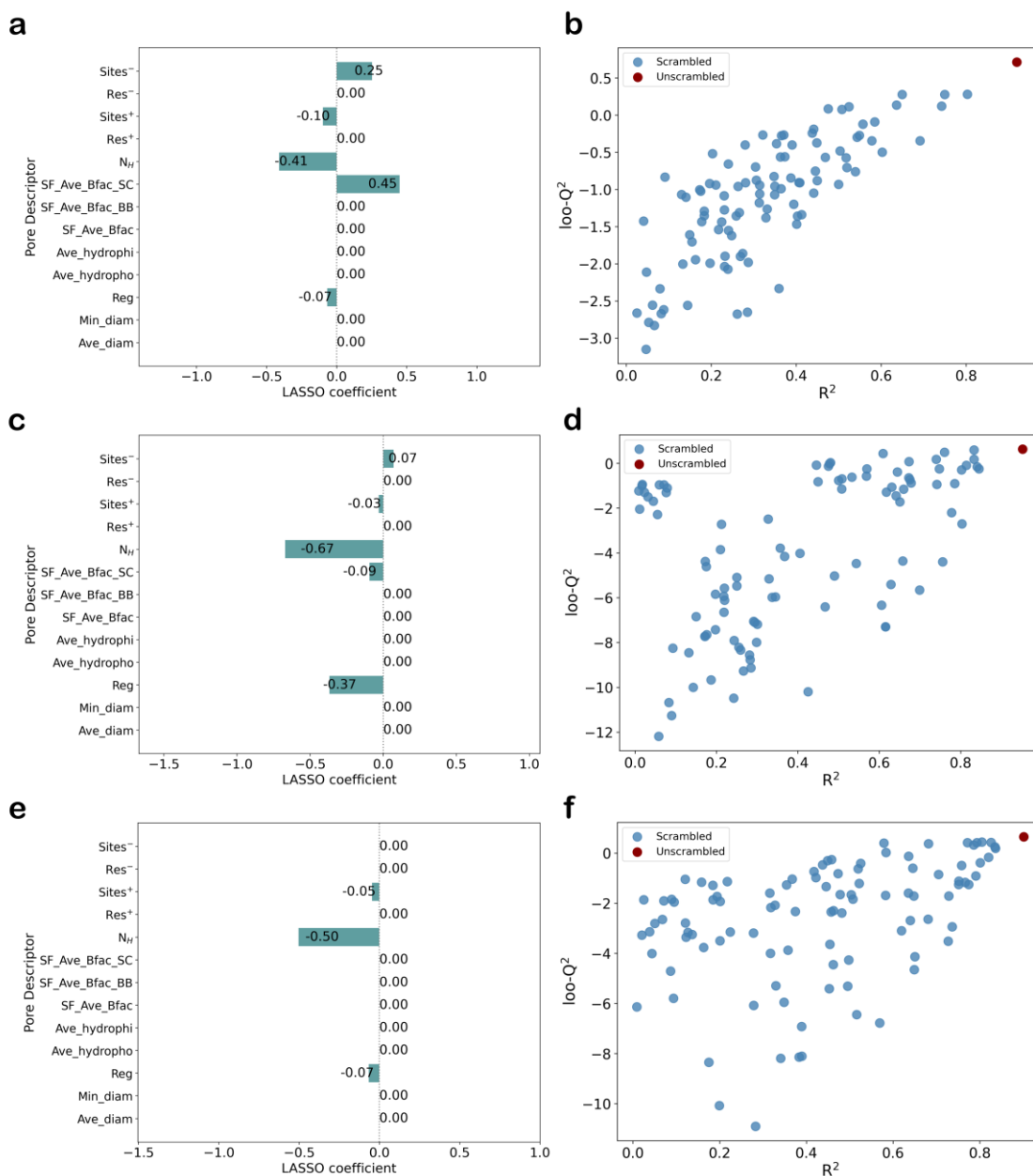


Figure S5. Final LASSO coefficients and y-scramblings analyses for the best-performing QSAR models. Panels a, c and e show bar plots of the final LASSO coefficients for models 1.3, 2.3a and 2.3b (see Table 3 of the main text), respectively, after applying the feature selection procedure. Coefficients were estimated using $\alpha = 0.1, 0.5,$ and 1.0 for models 1.3, 2.3a, and 2.3b, respectively, with 1,000,000 iterations in all cases. Panels b, d and f present the corresponding y-scrambling plots, showing leave-one-out predictive performance ($loo-Q^2$) as a function of the coefficient of determination (R^2) for 100 scrambled models (blue dots) compared with the original (unscrambled) model (red dot).

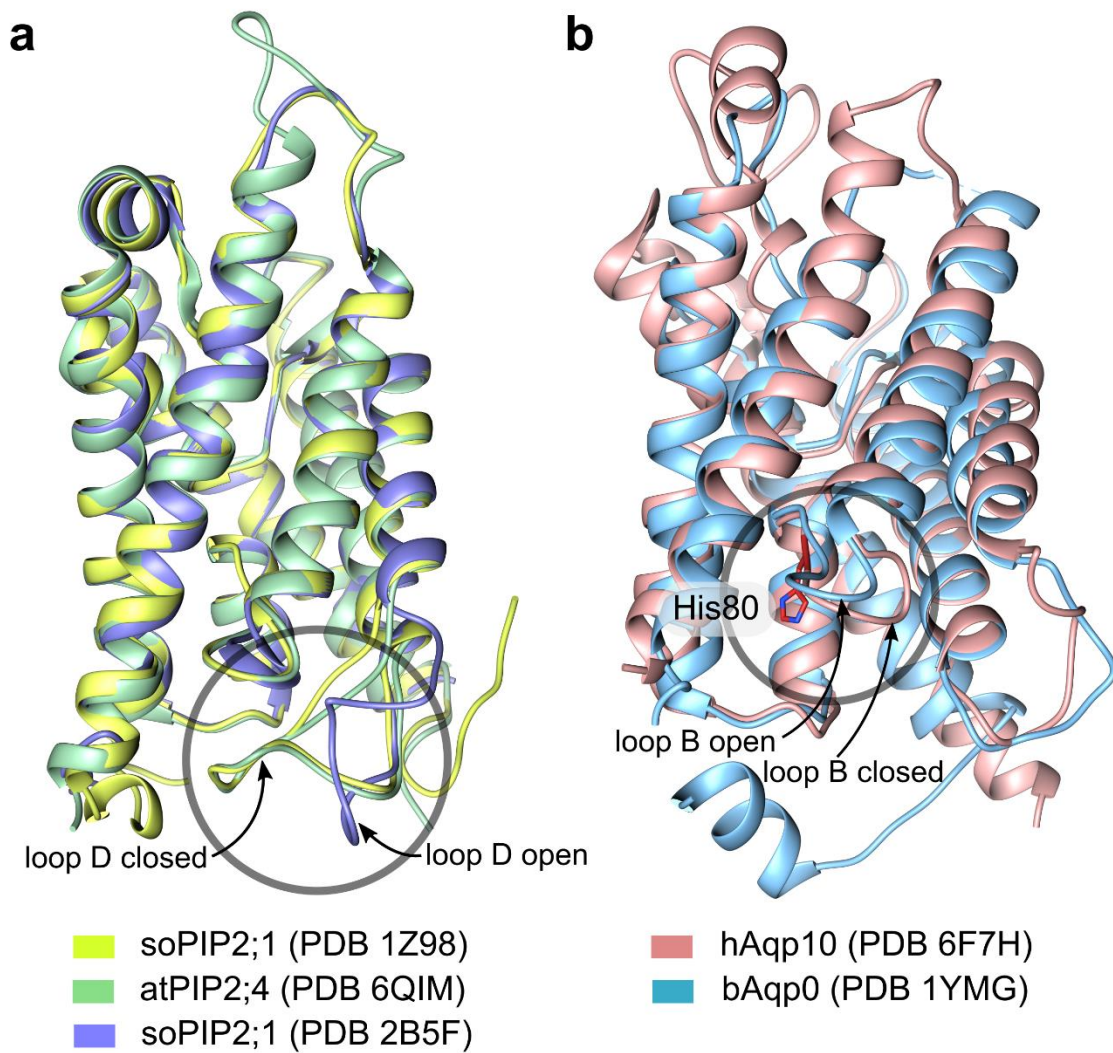


Figure S6. Structure comparison of AQPs on pore gating molecular events. (a) Overlapping of *Spinacia oleracea* PIP2;1, in its closed (PDB ID 1Z98 [45]) and open conformations (PDB ID 2B5F [45]), with the closed conformation of *Arabidopsis thaliana* PIP2;4 (PDB ID 6QIM [47]) aquaporin. Highlighted (circled region) are the main conformational differences in the cytoplasmic loop D that describe the ‘pore-gating’ event. (b) Overlapping hAQP10 (PDB ID 6F7H [48]) with bAQP0 (PDB ID 1YMG [34]) to highlight (circled region) the gated (closed) conformation of loop B in the former. His80, described as the key residue for the pH-dependent loop-B conformational change (pH-sensor [48]), is depicted (sticks).

SUPPLEMENTARY REFERENCES

1. O'Brien RM (2007) A Caution Regarding Rules of Thumb for Variance Inflation Factors. *Qual Quant* 41:673–690. <https://doi.org/10.1007/s11135-006-9018-6>
2. (1980) Detecting and Assessing Collinearity. In: *Regression Diagnostics*. John Wiley & Sons, Ltd, pp 85–191
3. Tibshirani R (1996) Regression Shrinkage and Selection Via the Lasso. *Journal of the Royal Statistical Society: Series B (Methodological)* 58:267–288. <https://doi.org/10.1111/j.2517-6161.1996.tb02080.x>
4. Gonen T, Walz T (2006) The structure of aquaporins. *Quarterly Reviews of Biophysics* 39:361–396. <https://doi.org/10.1017/S0033583506004458>
5. Xiong M, Li C, Wang W, Yang B (2023) Protein Structure and Modification of Aquaporins. In: Yang B (ed) *Aquaporins*. Springer Nature, Singapore, pp 15–38
6. Dingwell DA, Brown LS, Ladizhansky V (2019) Structure of the Functionally Important Extracellular Loop C of Human Aquaporin 1 Obtained by Solid-State NMR under Nearly Physiological Conditions. *The journal of physical chemistry B* 123:7700–7710. <https://doi.org/10.1021/acs.jpcc.9b06430>
7. Tajkhorshid E, Nollert P, Jensen MØ, et al (2002) Control of the selectivity of the aquaporin water channel family by global orientational tuning. *Science (New York, NY)* 296:525–530. <https://doi.org/10.1126/science.1067778>
8. Fasano M, Morciano M, Bergamasco L, et al (2021) Deep-sea reverse osmosis desalination for energy efficient low salinity enhanced oil recovery. *Applied Energy* 304:117661. <https://doi.org/10.1016/j.apenergy.2021.117661>
9. Fu D, Lisbon A, Miercke LJ, et al (2000) Structure of a glycerol-conducting channel and the basis for its selectivity. *Science* 290:481–486. <https://doi.org/10.1126/science.290.5491.481>
10. Sachdeva R, Priyadarshini P, Gupta S (2023) Aquaporins Display a Diversity in their Substrates. *The Journal of Membrane Biology* 256:1–23. <https://doi.org/10.1007/s00232-022-00257-7>
11. Groot BL de, Engel A, Grubmüller H (2001) A refined structure of human aquaporin-1. *FEBS letters* 504:206–211. [https://doi.org/10.1016/S0014-5793\(01\)02743-0](https://doi.org/10.1016/S0014-5793(01)02743-0)
12. Sui H, Han BG, Lee JK, et al (2001) Structural basis of water-specific transport through the AQP1 water channel. *Nature* 41:872–878. <https://doi.org/10.1038/414872a>
13. Savage DF, Egea PF, Robles-Colmenares Y, et al (2003) Architecture and selectivity in aquaporins: 2.5 Å X-ray structure of aquaporin Z. *PLoS biology* 1:E72. <https://doi.org/10.1371/journal.pbio.0000072>
14. Jiang J, Daniels BV, Fu D (2006) Crystal structure of AqpZ tetramer reveals two distinct Arg-189 conformations associated with water permeation through the narrowest constriction

- of the water-conducting channel. *The Journal of biological chemistry* 281:454–460. <https://doi.org/10.1074/jbc.M508926200>
15. Palanivelu DV, Kozono DE, Engel A, et al (2006) Co-axial association of recombinant eye lens aquaporin-0 observed in loosely packed 3D crystals. *Journal of molecular biology* 355:605–611. <https://doi.org/10.1016/j.jmb.2005.10.032>
 16. Lee JK, Kozono D, Remis J, et al (2005) Structural basis for conductance by the archaeal aquaporin AqpM at 1.68 Å. *Proceedings of the National Academy of Sciences* 102:18932–18937. <https://doi.org/10.1073/pnas.0509469102>
 17. Savage DF, Stroud RM (2007) Structural basis of aquaporin inhibition by mercury. *Journal of molecular biology* 368:607–617. <https://doi.org/10.1016/j.jmb.2007.02.070>
 18. Tani K, Hiroaki TMY, Kamegawa A, et al (2009) Mechanism of aquaporin-4's fast and highly selective water conduction and proton exclusion. *Journal of molecular biology* 389:694–706. <https://doi.org/10.1016/j.jmb.2009.04.049>
 19. Horsefield R, Nordén K, Fellert M, et al (2008) High-resolution x-ray structure of human aquaporin 5. *Proceedings of the National Academy of Sciences of the United States of America* 105:13327–13332. <https://doi.org/10.1073/pnas.0801466105>
 20. Ho JD, Yeh R, Sandstrom A, et al (2009) Crystal structure of human aquaporin 4 at 1.8 Å and its mechanism of conductance. *Proceedings of the National Academy of Sciences of the United States of America* 106:7437–7442. <https://doi.org/10.1073/pnas.0902725106>
 21. Savage DF, O'Connell 3rd JD, Miercke LJ, et al (2010) Structural context shapes the aquaporin selectivity filter. *Proceedings of the National Academy of Sciences of the United States of America* 107:17164–17169. <https://doi.org/10.1073/pnas.1009864107>
 22. Carrillo DR, Ying LTY, Darwis D, et al (2014) Crystallization and preliminary crystallographic analysis of human aquaporin 1 at a resolution of 3.28 Å. *Acta crystallographica Section F, Structural biology communications* 70:1657–1663. <https://doi.org/10.1107/S2053230X14024558>
 23. Frick A, Eriksson UK, Mattia F de, et al (2014) X-ray structure of human aquaporin 2 and its implications for nephrogenic diabetes insipidus and trafficking. *Proceedings of the National Academy of Sciences of the United States of America* 111:6305–6310. <https://doi.org/10.1073/pnas.1321406111>
 24. Lieske J, Cerv M, Kreida S, et al (2019) On-chip crystallization for serial crystallography experiments and on-chip ligand-binding studies. *IUCrJ* 6:714–728. <https://doi.org/10.1107/S2052252519007395>
 25. Groot BL de, Grubmüller H (2005) The dynamics and energetics of water permeation and proton exclusion in aquaporins. *Current opinion in structural biology* 15:176–183. <https://doi.org/10.1016/j.sbi.2005.02.003>
 26. Murata K, Mitsuoka K, Hirai T, et al (2000) Structural determinants of water permeation through aquaporin-1. *Nature* 407:599–605. <https://doi.org/10.1038/35036519>

27. King L, Kozono D, Agre P (2004) From structure to disease: the evolving tale of aquaporin biology. *Nature Reviews Molecular Cell Biology* 5:687–698. <https://doi.org/10.1038/nrm1469>
28. Cui Y, Bastien DA (2011) Water transport in human aquaporin-4: molecular dynamics (MD) simulations. *Biochemical and biophysical research communications* 412:654–659. <https://doi.org/10.1016/j.bbrc.2011.08.019>
29. Ilan B, Tajkhorshid E, Schulten K, Voth GA (2004) The mechanism of proton exclusion in aquaporin channels. *Proteins* 55:223–228. <https://doi.org/10.1002/prot.20038>
30. De Groot BL, Frigato T, Helms V, Grubmüller H (2003) The Mechanism of Proton Exclusion in the Aquaporin-1 Water Channel. *Journal of Molecular Biology* 333:279–293. <https://doi.org/10.1016/j.jmb.2003.08.003>
31. Jensen MØ, Tajkhorshid E, Schulten K (2003) Electrostatic Tuning of Permeation and Selectivity in Aquaporin Water Channels. *Biophysical Journal* 85:2884–2899. [https://doi.org/10.1016/S0006-3495\(03\)74711-0](https://doi.org/10.1016/S0006-3495(03)74711-0)
32. Burykin A, Warshel A (2003) What Really Prevents Proton Transport through Aquaporin? Charge Self-Energy versus Proton Wire Proposals. *Biophysical Journal* 85:3696–3706. [https://doi.org/10.1016/S0006-3495\(03\)74786-9](https://doi.org/10.1016/S0006-3495(03)74786-9)
33. Kosinska Eriksson U, Fischer G, Friemann R, et al (2013) Subangstrom resolution X-ray structure details aquaporin-water interactions. *Science* 340:1346–1349. <https://doi.org/10.1126/science.1234306>
34. Harries WE, Akhavan D, Miercke LJ, et al (2004) The channel architecture of aquaporin 0 at a 2.2-Å resolution. *Proceedings of the National Academy of Sciences of the United States of America* 101:14045–14050. <https://doi.org/10.1073/pnas.0405274101>
35. Gonen T, Cheng Y, Sliz P, et al (2005) Lipid-protein interactions in double-layered two-dimensional AQP0 crystals. *Nature* 438:633–638. <https://doi.org/10.1038/nature04321>
36. de Mare SW, Venskutonytė R, Eltschkner S, et al (2020) Structural basis for glycerol efflux and selectivity of human aquaporin 7. *Structure* 28:215–222. <https://doi.org/10.1016/j.str.2019.11.011>
37. Newby ZE, O’Connell Iii J, Robles-Colmenares Y, et al (2008) Crystal structure of the aquaglyceroporin PfAQP from the malarial parasite *Plasmodium falciparum*. *Nature structural & molecular biology* 15:619–625. <https://doi.org/10.1038/nsmb.1431>
38. Ren G, Reddy VS, Cheng A, et al (2001) Visualization of a water-selective pore by electron crystallography in vitreous ice. *Proceedings of the National Academy of Sciences of the United States of America* 98:1398–1403. <https://doi.org/10.1073/pnas.98.4.1398>
39. Verkman AS (2013) Aquaporins. *Current Biology* 23:R52–R55. <https://doi.org/10.1016/j.cub.2012.11.025>

40. Araya-Secchi R, Garate JA, Holmes DS, Perez-Acle T (2011) Molecular dynamics study of the archaeal aquaporin AqpM. *BMC Genomics* 12 Suppl 4:S8. <https://doi.org/10.1186/1471-2164-12-S4-S8>
41. Krenc D, Song J, Almasalmeh A, et al (2014) The arginine-facing amino acid residue of the rat aquaporin 1 constriction determines solute selectivity according to its size and lipophilicity. *Molecular Membrane Biology* 31:228–238. <https://doi.org/10.3109/09687688.2014.960493>
42. Gonen T, Sliz P, Kistler J, et al (2004) Aquaporin-0 membrane junctions reveal the structure of a closed water pore. *Nature* 429:193–197. <https://doi.org/10.1038/nature02503>
43. Reichow SL, Clemens DM, Freites JA, et al (2013) Allosteric mechanism of water-channel gating by Ca²⁺-calmodulin. *Nature structural & molecular biology* 20:1085–1092. <https://doi.org/10.1038/nsmb.2630>
44. Hiroaki Y, Tani K, Kamegawa A, et al (2006) Implications of the aquaporin-4 structure on array formation and cell adhesion. *Journal of molecular biology* 355:628–639. <https://doi.org/10.1016/j.jmb.2005.10.081>
45. Törnroth-Horsefield S, Wang Y, Hedfalk K, et al (2006) Structural mechanism of plant aquaporin gating. *Nature* 439:688–694. <https://doi.org/10.1038/nature04316>
46. Liu Q, Hillerich B, Love J, NYCOMPS. RCSB Protein Data Bank, 3LLQ: Aquaporin structure from plant pathogen *Agrobacterium tumefaciens*. <https://www.rcsb.org/structure/3llq>. Accessed 6 Oct 2023
47. Wang H, Schoebel S, Schmitz F, et al (2020) Characterization of aquaporin-driven hydrogen peroxide transport. *Biochimica et biophysica acta Biomembranes* 1862:183065. <https://doi.org/10.1016/j.bbamem.2019.183065>
48. Gotfryd K, Móscica AF, Missel JW, et al (2018) Human adipose glycerol flux is regulated by a pH gate in AQP10. *Nature communications* 9:1–11. <https://doi.org/10.1038/s41467-018-07176-z>
49. Lindahl V, Gourdon P, Andersson M, Hess B (2018) Permeability and ammonia selectivity in aquaporin TIP2;1: linking structure to function. *Sci Rep* 8:2995. <https://doi.org/10.1038/s41598-018-21357-2>
50. Kirscht A, Kaptan SS, Bienert GP, et al (2016) Crystal Structure of an Ammonia-Permeable Aquaporin. *PLoS biology* 14:e1002411. <https://doi.org/10.1371/journal.pbio.1002411>
51. Zhang Y, Skolnick J (2004) Scoring function for automated assessment of protein structure template quality. *Proteins: Structure, Function, and Bioinformatics* 57:702–710. <https://doi.org/10.1002/prot.20264>
52. Xu J, Zhang Y (2010) How significant is a protein structure similarity with TM-score= 0.5? *Bioinformatics* 26:889–895. <https://doi.org/10.1093/bioinformatics/btq066>
53. (2024) RCSB PDB Pairwise Structure Alignment. <https://www.rcsb.org/alignment>. Accessed 26 Apr 2024

54. Li Z, Jaroszewski L, Iyer M, et al (2020) FATCAT 2.0: towards a better understanding of the structural diversity of proteins. *Nucleic acids research* 48:W60–W64. <https://doi.org/10.1093/nar/gkaa443>
55. Ye Y, Godzik A (2003) Flexible structure alignment by chaining aligned fragment pairs allowing twists. *Bioinformatics* 19:ii246–ii255. <https://doi.org/10.1093/bioinformatics/btg1086>
56. Pellegrini-Calace M, Maiwald T, Thornton JM (2009) PoreWalker: A Novel Tool for the Identification and Characterization of Channels in Transmembrane Proteins from Their Three-Dimensional Structure. *PLoS Comput Biol* 5:e1000440. <https://doi.org/10.1371/journal.pcbi.1000440>
57. Ozu M, Alvear-Arias JJ, Fernandez M, et al (2022) Aquaporin Gating: A New Twist to Unravel Permeation through Water Channels. *International Journal of Molecular Sciences* 23:12317. <https://doi.org/10.3390/ijms232012317>
58. Yang B (2023) *Aquaporins, Second Edition*. Springer Nature, Singapore
59. Frick A, Järvå M, Törnroth-Horsefield S (2013) Structural basis for pH gating of plant aquaporins. *FEBS Letters* 587:989–993. <https://doi.org/10.1016/j.febslet.2013.02.038>
60. Tournaire-Roux C, Sutka M, Javot H, et al (2003) Cytosolic pH regulates root water transport during anoxic stress through gating of aquaporins. *Nature* 425:393–397. <https://doi.org/10.1038/nature01853>
61. Yaneff A, Sigaut L, Marquez M, et al (2014) Heteromerization of PIP aquaporins affects their intrinsic permeability. *Proceedings of the National Academy of Sciences* 111:231–236. <https://doi.org/10.1073/pnas.1316537111>
62. Yaneff A, Sigaut L, Gómez N, et al (2016) Loop B serine of a plasma membrane aquaporin type PIP2 but not PIP1 plays a key role in pH sensing. *Biochimica et Biophysica Acta (BBA) - Biomembranes* 1858:2778–2787. <https://doi.org/10.1016/j.bbamem.2016.08.002>
63. Goldman RP, Jozefkowicz C, Canessa Fortuna A, et al (2017) Tonoplast (BvTIP1;2) and plasma membrane (BvPIP2;1) aquaporins show different mechanosensitive properties. *FEBS Letters* 591:1555–1565. <https://doi.org/10.1002/1873-3468.12671>
64. Garate J-A, English NJ, MacElroy JMD (2011) Human aquaporin 4 gating dynamics in dc and ac electric fields: A molecular dynamics study. *The Journal of Chemical Physics* 134:055110. <https://doi.org/10.1063/1.3529428>
65. English NJ, Garate J-A (2016) Near-microsecond human aquaporin 4 gating dynamics in static and alternating external electric fields: Non-equilibrium molecular dynamics. *The Journal of Chemical Physics* 145:085102. <https://doi.org/10.1063/1.4961072>
66. Hub JS, Aponte-Santamaría C, Grubmüller H, De Groot BL (2010) Voltage-Regulated Water Flux through Aquaporin Channels In Silico. *Biophysical Journal* 99:L97–L99. <https://doi.org/10.1016/j.bpj.2010.11.003>

67. Hashido M, Ikeguchi M, Kidera A (2005) Comparative simulations of aquaporin family: AQP1, AQPZ, AQP0 and GlpF. *FEBS letters* 579:5549–5552. <https://doi.org/10.1016/j.febslet.2005.09.018>
68. Van Hoek AN, Wiener M, Bicknese S, et al (1993) Secondary structure analysis of purified functional CHIP28 water channels by CD and FTIR spectroscopy. *Biochemistry* 32:11847–11856. <https://doi.org/10.1021/bi00095a013>
69. Chandy G, Zampighi GA, Kreman M, Hall JE (1997) Comparison of the water transporting properties of MIP and AQP1. *The Journal of membrane biology* 159:29–39. <https://doi.org/10.1007/s002329900266>
70. Zampighi GA, Kreman M, Boorer KJ, et al (1995) A method for determining the unitary functional capacity of cloned channels and transporters expressed in *Xenopus laevis* oocytes. *J Membran Biol* 148:65–78. <https://doi.org/10.1007/BF00234157>
71. Saboe PO, Rapisarda C, Kaptan S, et al (2017) Role of Pore-Lining Residues in Defining the Rate of Water Conduction by Aquaporin-0. *Biophysical Journal* 112:953–965. <https://doi.org/10.1016/j.bpj.2017.01.026>
72. Yang B, Verkman A (1997) Water and glycerol permeabilities of aquaporins 1–5 and MIP determined quantitatively by expression of epitope-tagged constructs in *Xenopus* oocytes. *Journal of Biological Chemistry* 272:16140–16146. <https://doi.org/10.1074/jbc.272.26.16140>
73. Schulte DJ, van Hoek AN (1997) Functional Analysis and Association State of Water Channel (AQP-1) Isoforms Purified from Six Mammals. *Comparative Biochemistry and Physiology Part B: Biochemistry and Molecular Biology* 118:35–43. [https://doi.org/10.1016/S0305-0491\(97\)00015-1](https://doi.org/10.1016/S0305-0491(97)00015-1)
74. Zhu F, Tajkhorshid E, Schulten K (2004) Theory and simulation of water permeation in aquaporin-1. *Biophysical journal* 86:50–57. [https://doi.org/10.1016/S0006-3495\(04\)74082-5](https://doi.org/10.1016/S0006-3495(04)74082-5)
75. Van Hoek A, Verkman A (1992) Functional reconstitution of the isolated erythrocyte water channel CHIP28. *Journal of Biological Chemistry* 267:18267–18269. [https://doi.org/10.1016/S0021-9258\(19\)36953-4](https://doi.org/10.1016/S0021-9258(19)36953-4)
76. Zeidel ML, Ambudkar SV, Smith BL, Agre P (1992) Reconstitution of functional water channels in liposomes containing purified red cell CHIP28 protein. *Biochemistry* 31:7436–7440. <https://doi.org/10.1021/bi00148a002>
77. Walz T, Smith BL, Zeidel ML, et al (1994) Biologically active two-dimensional crystals of aquaporin CHIP. *Journal of Biological Chemistry* 269:1583–1586. [https://doi.org/10.1016/S0021-9258\(17\)42062-X](https://doi.org/10.1016/S0021-9258(17)42062-X)
78. Zeidel ML, Nielsen S, Smith BL, et al (1994) Ultrastructure, pharmacologic inhibition, and transport selectivity of aquaporin CHIP in proteoliposomes. *Biochemistry* 33:1606–1615. <https://doi.org/10.1021/bi00172a042>

79. Wertén PJL, Hasler L, Koenderink JB, et al (2001) Large-scale purification of functional recombinant human aquaporin-2. *FEBS Letters* 504:200–205. [https://doi.org/10.1016/S0014-5793\(01\)02703-X](https://doi.org/10.1016/S0014-5793(01)02703-X)
80. Binesh AR, Kamali R (2015) Molecular dynamics insights into human aquaporin 2 water channel. *Biophysical chemistry* 207:107–113. <https://doi.org/10.1016/j.bpc.2015.10.002>
81. Kitchen P, Salman MM, Halsey AM, et al (2020) Targeting Aquaporin-4 Subcellular Localization to Treat Central Nervous System Edema. *Cell* 181:784-799.e19. <https://doi.org/10.1016/j.cell.2020.03.037>
82. Alberga D, Nicolotti O, Lattanzi G, et al (2014) A new gating site in human aquaporin-4: Insights from molecular dynamics simulations. *Biochimica et Biophysica Acta (BBA)-Biomembranes* 1838:3052–3060. <https://doi.org/10.1016/j.bbamem.2014.08.015>
83. Hashido M, Kidera A, Ikeguchi M (2007) Water transport in aquaporins: osmotic permeability matrix analysis of molecular dynamics simulations. *Biophysical journal* 93:373–385. <https://doi.org/10.1529/biophysj.106.101170>
84. Tong J, Wu Z, Briggs MM, et al (2016) The Water Permeability and Pore Entrance Structure of Aquaporin-4 Depend on Lipid Bilayer Thickness. *Biophysical Journal* 111:90–99. <https://doi.org/10.1016/j.bpj.2016.05.039>
85. Alishahi M, Kamali R (2018) Forced diffusion of water molecules through aquaporin-5 biomembrane; a molecular dynamics study. *Biophysics and physcobiology* 15:255–262. https://doi.org/10.2142/biophysico.15.0_255
86. Kozono D, Ding X, Iwasaki I, et al (2003) Functional Expression and Characterization of an Archaeal Aquaporin. *Journal of Biological Chemistry* 278:10649–10656. <https://doi.org/10.1074/jbc.M212418200>
87. Borgnia MJ, Kozono D, Calamita G, et al (1999) Functional reconstitution and characterization of AqpZ, the E. coli water channel protein. *Journal of molecular biology* 291:1169–1179. <https://doi.org/10.1006/jmbi.1999.3032>
88. Jensen MØ, Mouritsen OG (2006) Single-channel water permeabilities of Escherichia coli aquaporins AqpZ and GlpF. *Biophysical journal* 90:2270–2284. <https://doi.org/10.1529/biophysj.105.073965>
89. Pohl P, Saparov SM, Borgnia MJ, Agre P (2001) Highly selective water channel activity measured by voltage clamp: analysis of planar lipid bilayers reconstituted with purified AqpZ. *Proceedings of the National Academy of Sciences* 98:9624–9629. <https://doi.org/10.1073/pnas.161299398>
90. Borgnia MJ, Agre P (2001) Reconstitution and functional comparison of purified GlpF and AqpZ, the glycerol and water channels from Escherichia coli. *Proceedings of the National Academy of Sciences* 98:2888–2893. <https://doi.org/10.1073/pnas.051628098>

91. Zhu F, Tajkhorshid E, Schulten K (2002) Pressure-induced water transport in membrane channels studied by molecular dynamics. *Biophysical journal* 83:154–160. [https://doi.org/10.1016/S0006-3495\(02\)75157-6](https://doi.org/10.1016/S0006-3495(02)75157-6)
92. Saparov SM, Tsunoda SP, Pohl P (2005) Proton exclusion by an aquaglyceroprotein: a voltage clamp study. *Biology of the Cell* 97:545–550. <https://doi.org/10.1042/BC20040136>
93. Wachlmayr J, Samineni L, Knyazev DG, et al (2023) Biophysical quantification of unitary solute and solvent permeabilities to enable translation to membrane science. *Journal of Membrane Science* 675:121308. <https://doi.org/10.1016/j.memsci.2022.121308>
94. The UniProt Consortium (2023) UniProt: the Universal Protein Knowledgebase in 2023. *Nucleic Acids Research* 51:D523–D531. <https://doi.org/10.1093/nar/gkac1052>
95. Berman HM, Mitsuoka K, Westbrook J, et al (2000) The Protein Data Bank. *Nucleic Acids Research* 28:235–242. <https://doi.org/10.1093/nar/28.1.235>
96. (2022) Discovery Studio, BIOVIA, Dassault Systèmes
97. Virtanen P, Gommers R, Oliphant TE, et al (2020) SciPy 1.0: fundamental algorithms for scientific computing in Python. *Nat Methods* 17:261–272. <https://doi.org/10.1038/s41592-019-0686-2>